PhD Thesis

for the award of the degree of Doctor of Philosophy

"Raman Spectroscopic Probe of Chemical Reactions at the Surfaces of Gold Nanostructures"

Submitted by: Srimanta Pal

Roll No. 166122105

Department of Chemistry

Indian Institute of Technology Guwahati

Guwahati- 781039, Assam, India

May, 2022

TH-2949_166122105

Raman Spectroscopic Probe of Chemical Reactions at the Surfaces of Gold Nanostructures

A thesis submitted by Srimanta Pal

Roll No. 166122105

Supervisor: Prof. Arun Chattopadhyay

Department of Chemistry

Indian Institute of Technology Guwahati

Guwahati, Assam-781039

India

TH-2949_166122105

DECLARATION

I hereby declare that the results and discussions embodied in the thesis titled "***Raman Spectroscopic Probe of Chemical Reactions at the Surfaces of Gold Nanostructures"*** are the outcome of research work carried out by me under the supervision of ***Prof. Arun Chattopadhyay***, **Department of Chemistry**, **Indian Institute of Technology Guwahati**, **Guwahati**, **Assam**, **India** for the award of the degree of Doctor of Philosophy. To the best of my knowledge, the present thesis has not been submitted for any degree, diploma, associateship etc. of any Institute or University elsewhere.

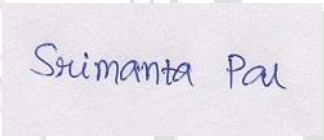

Srimanta Pal
Roll no.: 166122105
Department of Chemistry, IIT Guwahati
Guwahati-781039, Assam, India
Date: 11.05.2022

TH-2949_166122105

भारतीय प्रौद्योगिकी संस्थान गुवाहाटी
INDIAN INSTITUTE OF TECHNOLOGY GUWAHATI

CERTIFICATE

This is to certify that the thesis entitled "**Raman Spectroscopic Probe of Chemical Reactions at the Surfaces of Gold Nanostructures"** being submitted to the Indian Institute of Technology Guwahati by Srimanta Pal (Roll No. 166122105) for the award of the degree of Doctor of Philosophy in Chemistry is a bonafide record of research work carried by him. The data reported and the conclusion drawn herein are the results of the original findings of his work. This work has not been submitted elsewhere for any degree or diploma.

Prof. Arun Chattopadhyay
Department of Chemistry
Indian Institute of Technology Guwahati
Guwahati-781 039, INDIA

Prof. Arun Chattopadhyay
Thesis Supervisor
Department of Chemistry, IIT Guwahati
Guwahati-781039, Assam, India.
Date: 11.05.2022

TH-2949_166122105

ACKNOWLEDGEMENTS

Firstly, an honest thank you to all the people who had encouraged me directly or indirectly at odd and even times during my PhD life. During my MSc, I dreamt of pursuing my doctoral studies at IIT, and now it's time to complete my PhD at IIT Guwahati. I am delighted and thankful to IIT Guwahati for giving me a chance to carry out my doctoral studies in this wonderful green campus.

I would like to express my sincere gratitude and thanks to my supervisor, Prof. Arun Chattopadhyay. His enormous support in carrying out my research work, constructive criticism and positive motivation made my ground as a researcher with optimistic personality. I also thank him for providing me with the freedom to work. It has been my privilege to work with a generous person like him and share knowledge both scientifically and non-scientifically.

Next, I express my sincere thanks to my doctoral committee chairman Prof. Chandan Mukherjee and to the other committee members Dr. Akshai Kumar A. S and Dr. G. P. Partho Sarathi for their timely assessment of my thesis work, valuable suggestions and corrections made for the same.

I acknowledge the Department of Chemistry, Central Instrumental Facility and Centre for Nanotechnology, IIT Guwahati for providing me with the much needed instrumental facilities. I take this opportunity to convey my thanks and gratitude to all the lab members in our research group. My heartfelt and special thanks to Dr. Anushree Dutta for her support at the beginning of my PhD life.

Last but not least, I convey my thanks and gratitude to my parents, sister and close friends for their well wishes, encouragement and support in all my endeavours. Although my parents do not have any formal degrees, my father understood the importance of education and supported me in pursuing higher studies by fighting a lot of obstacles. Because of him, I am going to be the first person to achieve a doctorate in my family history.

It will not be complete without thanking god for giving me all the blessings.

Srimanta

TH-2949_166122105

CONTENTS

TH-2949_166122105

TH-2949_166122105

Raman Spectroscopic Probe of Chemical Reactions at the Surfaces of Gold Nanostructures

THESIS ABSTRACT

A significant numbers of research in nanoscience are focused on the plasmon induced photochemical reactions. In addition to the emphasis on the mechanism, there is a need to improve the kinetic efficiency of such reactions. On the other hand, applications of metal nanostructures are not limited to the plasmon induced reactions only. Although surface enhanced Raman scattering is a popular technique, surface enhanced resonance Raman scattering (SERRS) provides the best opportunity to pursue vibrational probes even at single molecule level, it can be exploited to characterize the bonding, structure and kinetics of formation of various complexes that are not amenable to many other spectroscopic techniques. This leads to the importance of assembly of metal nanostructures and their application potential. The current thesis addresses some of the issues related to the above. **Chapter 1** gives a general overview of the metal nanostructures and their implications in chemical reactions. In **Chapter 2**, end-to-end specific assembled gold nanorods were achieved under centrifugal force, exploiting hydrogen bond formation between 4-aminothiophenol (4-ATP) attached to the longitudinal ends of gold nanorods. The transformation of 4-ATP into dimercaptoazobenzene (DMAB) was carried out at the plasmonic hot-spots of assembled gold nanorods under the excitation of 632.8 nm laser. The degradation of DMAB formed at the hot-spots was also performed using hydrogen peroxide (H_2O_2). Kinetic data based on surface enhanced Raman spectra revealed that the coupling reaction was faster by 1.6 fold at the hot-spots of end-to-end assembled gold nanorod than at the surface of longitudinal end of non-assembled gold nanorods. This study opens a new direction of carrying out plasmon catalyzed photochemical reaction selectively at the hot spot region with enhanced reaction rate.

In **Chapter 3**, surface enhanced Raman scattering (SERS) was used to monitor the effect of metal cations (Mn(II), Co(II), Ni(II), Cu(II) and Zn(II)) on the plasmon catalyzed conversion of 4-ATP into DMAB at the surface of Au nanorods and nanospheres using 632.8 and 532 nm laser excitations, respectively. When the coupling reaction was carried out under appropriate laser irradiation, DMAB production was augmented markedly by a factor of 1.98 - 4.07 on the surface of Au nanoparticle and 3.34 - 5.74 on the surface of Au nanorods (in

TH-2949_166122105

the presence of different metal cations). Moreover, the SERS signal of product was significantly enhanced. Thus, this study shows a new direction of performing plasmon catalyzed reaction with enhanced yield and SERS signal.

In **Chapter 4**, we report the catalytic formation of bridged polynuclear peroxo complex of Co(II) and 2-picolylamine (2-PA) in aqueous alkaline medium on the surface of Au nanoparticles. The reaction followed sigmoidal kinetics both in absence and presence of Au nanoparticles with an order of magnitude higher rate constant for the latter. Importantly, using UV-Vis spectroscopy, mass spectrometry and surface enhanced resonance Raman scattering (SERRS), we conclude the formation of peroxo complex with 2-PA acting as a monodentate ligand. The absorbance of the polynuclear complex at 595 nm and the extinction maximum of (agglomerated) Au nanoparticles at 750 nm provided the right opportunity to pursue SERRS using 632.8 nm laser excitation. Density functional theoretical calculation indicated that the lowering of HOMO-LUMO energy gap of 2-PA bonded to the nanoparticle surface helped catalyze the reaction.

In **Chapter 5**, we report simultaneous quantitative detection of H_2O, D_2O and HOD in the same reaction mixture with the help of bridged polynuclear peroxo complex in absence and presence of Au nanoparticles on the basis of probing the peroxide vibrational mode in resonance Raman and surface enhanced resonance Raman spectrum. We synthesized bridged polynuclear peroxo complex in different solvent mixture of H_2O and D_2O. Due to the formation of different nature of hydrogen bonding between peroxide and solvent molecules (H_2O, D_2O and HOD), vibrational frequency of peroxo bond was significantly affected. Mixtures of different H_2O and D_2O concentrations produced different HOD concentrations and that led to different intensities of peaks positioned at 897, 823 and 867 cm^{-1} indicating H_2O, D_2O and HOD, respectively. The lowest detection limits (LODs) were 0.028 mole fraction of D_2O in H_2O and 0.046 mole faction of H_2O in D_2O. In addition, for the first time the results revealed that the cis-peroxide forms two hydrogen bonds with solvent molecules.

Chapter 6 includes summary and future prospects of the thesis.

TH-2949_166122105

CHAPTER 1

1.1. Introduction

The term "nano" represents something which is very small – one billionth of a meter. Matter having at least one dimension ranging from 1 to 100 nm is generally accepted as nanomaterial. Nanoscience deals with the structures of nanomaterials and the technology that offers potential applications of nanoscience is known as nanotechnology. In the 21st century nanotechnology has gained tremendous interest whereas nanoscience has been of attention since the last century. Since nanomaterials fall in the size range between molecule and its bulk material, special attributes have been observed in terms of chemical, optical, electrical and magnetic properties that are imperative in the fundamental scientific research in chemistry, physics, biology, materials science, computer science as well as chemical catalysis, energy, biomedical and technological applications.

1.2. Metal Nanostructures and their Properties

Due to large surface to volume ratio metal nanostructures have been achieving enormous interest in various applications as compared to their bulk counterparts.[1] Higher percentage of surface atoms leads to higher reactivity of nanomaterials.[2-3] The size and shape dependent properties of nanostructures are extensively used in the field of applications such as biomedical devices, electronics, information storage and energy technologies.[4-9] Modern scientific research on nanomaterials began after the preparation of colloidal Au sol by Michael Faraday.[10] After 1950 Turkevich and Enustun synthesized Au and Ag nanospheres with tunable sizes.[11] Metal nanostructure having size in the range of 2 to 100 nm consists less than 10^6 number of atoms and exhibits a special characteristic property - surface plasmon resonance (SPR). SPR arises due to the collective oscillation of free electrons – known as plasmons – under the irradiation of light when the frequency of plasmons is in resonance condition with the frequency of incident light.[12,13] Presence of SPR condition in

TH-2949_166122105

metal nanostructures reveal unique behavior in terms of optical, chemical, magnetic and electrical properties that are also dependent on their shape, size and composition.

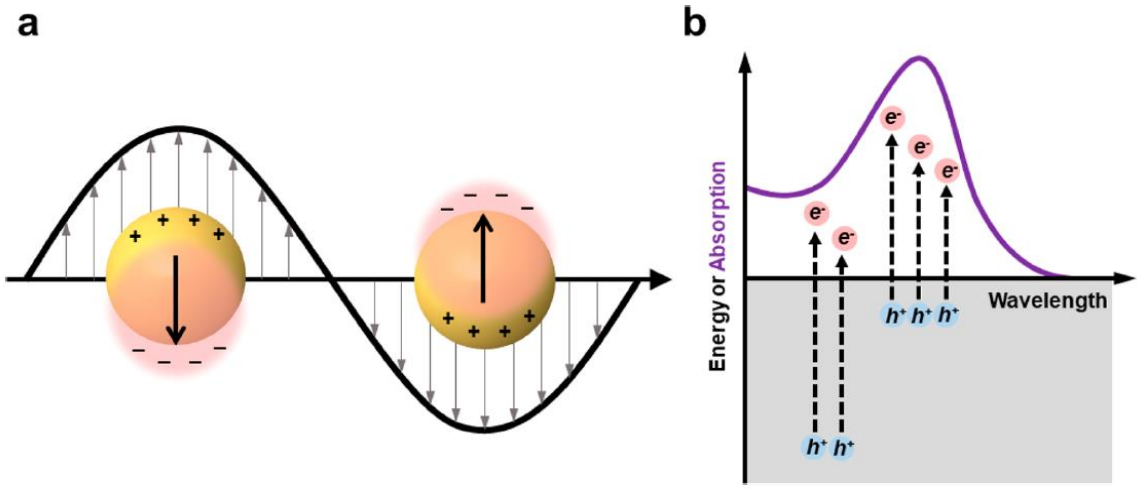

Figure 1.1. (**a**) Coherent oscillation of electron cloud (localized SPR) of nanoparticle in presence of electric field. (**b**) Hot electron (e^-) and hot hole (h^+) generation (due to SPR dephasing) along with the corresponding extinction spectrum of plasmonic material. Adapted with permission from reference 14. Copyright 2018 American Chemical Society.

When surface plasmons are propagating along the surface under resonance condition with the incoming light, it is known as propagating surface plasmon resonance (PSPR). But, when the surface plasmons are confined to a metal nanostructure having size less than or comparable to the incoming light's wavelength, free electrons on the surface display coherent oscillation, which is known as localized surface plasmon resonance (LSPR) under the resonance condition with the incoming light (**Figure 1.1**).[13,14] Among all the transition metals coinage elements, copper, silver, and gold have drawn a significant attention in the field of nanoscience and technology because the SPR of their nanostructures occur in the visible range of the electromagnetic spectrum and exhibit characteristic color.[1,12] The position and wavelength of SPR extinction band of metal nanostructure are influenced by its shape, size, inter-particle interactions, refractive index and dielectric properties of the surrounding medium.[15]

Spherical nanostructures show sharp and single extinction band due to dipole plasmon resonance when the entire surface charge distribution oscillates at the frequency of the incident electric field of light.[13] But when we consider metal nanorods, due to particle

TH-2949_166122105

anisotropy, the dipole plasmon resonance splits between longitudinal (along the length) and transverse (along the width) modes, and thus two extinction bands are observed.[16] Moreover, strong augmentation of electromagnetic field occurs near to the surface and decreases rapidly with the distance from the surface of metal nanostructure.[17] Thus, any molecule attached at the surface of metal nanostructure can show enhanced optical properties such as Raman scattering, fluorescence etc. – which led to the development of the concepts of surface-enhanced fluorescence spectroscopy (SEFS), surface-enhanced Raman scattering (SERS) etc.[18,19] Additionally, metal nanostructures can exhibit redox property.[20] All these special characteristic properties make metal nanostructure a potent candidate in the field of nanoscience and nanotechnology.

When two or more plasmonic metal nanostructures are placed very close to each other, surface plasmons can couple, which generates new SPR.[21] Thus, scientists have been exploring a persistent idea regarding the formation of higher order assembled structure from individual nanostructures.[22-26] Higher dimensional hierarchical structures are gaining interest in the technological field such as in fabrication of super-efficient sensors, photovoltaic and optoelectronic devices.[27-29] At the inter-particle gap of assembled metal nanostructures, strong electric field enhancement occurs due to plasmon coupling. In this inter-particle gap distance- known as hot-spot region – the magnitude of electric field is greater by many orders as compared to the other regions of the surface (**Figure 1.2**).[12,13] Thus, at this region higher sensitivity – e.g., down to a single molecular level - can be achieved in the SERS sepctrum.[22] It is reported that 98% of signal in SERS spectrum originates from 2% of the molecules situated at hot-spot region.[30] **Figure 1.2c** shows the excitation of carriers inside the metal nanostructure and their transfer to the neighboring species. Thus, multi-mers or higher order assemblies of metal nanostructures have gained extensive interest in catalysis, sensing etc.[22]

TH-2949_166122105

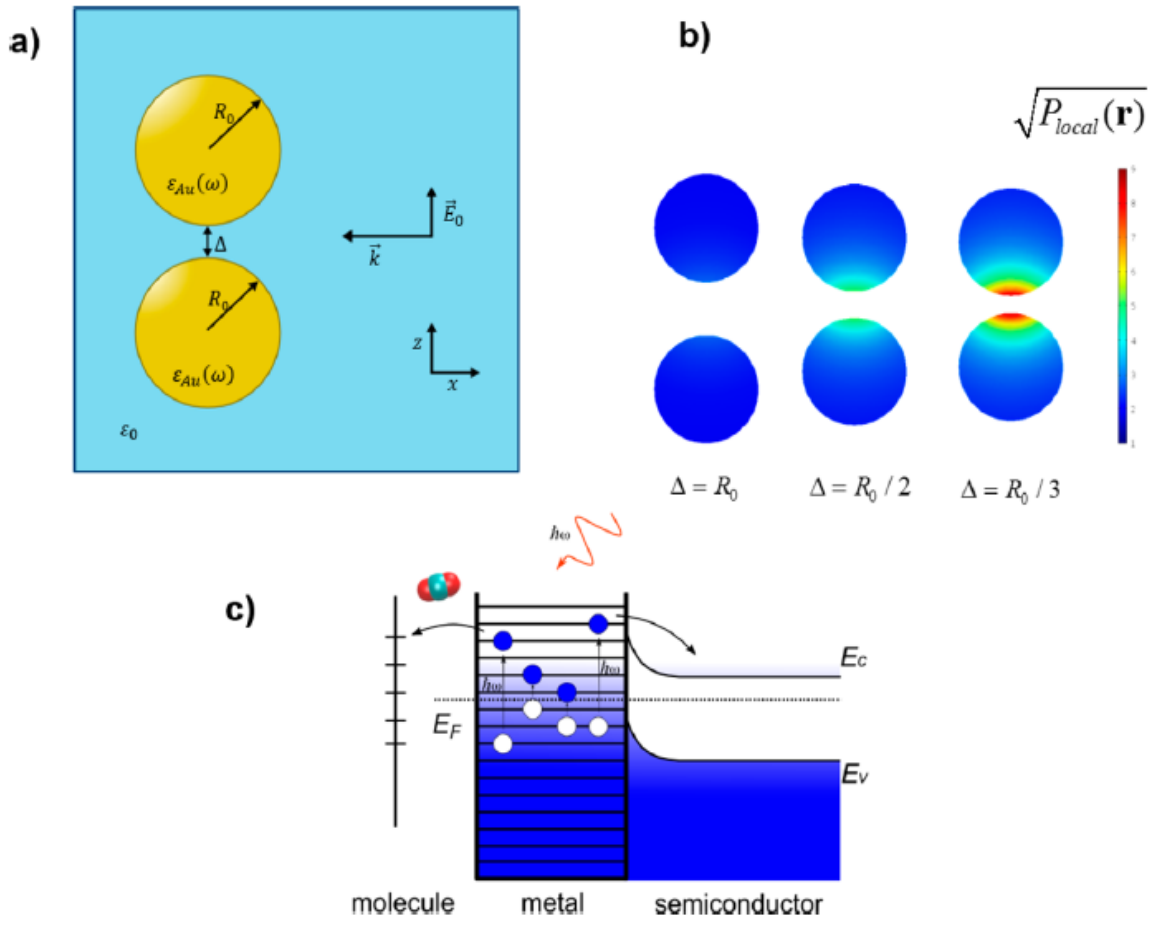

Figure 1.2. (**a**) Geometry and corresponding parameters for dimer of nanospheres. (**b**) Hot-spot intensity (as represented through the square root of local field enhancement at hot-spot region) for different interparticle gap distances. (**c**) Cartoon diagram of energy levels depicting excitation of carriers inside the metal nanostructure and their transfer to the neighboring species. Adapted with permission from reference 132. Copyright 2016 American Chemical Society.

1.3. Gold Nanospheres

Gold nanospheres (Au nanospheres) have been gaining enormous interest in the field of nanoscience and technology because of their tunable optical and electronic properties, resistive nature towards oxidation and the presence of their SPR band in the visible region of electromagnetic spectrum.[31] Au nanosphere colloid was first synthesized by Michael

TH-2949_166122105

Faraday in 1857.[10] In 1908, by solving Maxwell's equation Gustav Mie described the scattering and absorption phenomena of spherical nanoparticles dispersed in a homogeneous solution.[32] However, modern science uses DDA (discrete dipole approximation), FEM (finite element method) and FDTD (finite difference time domain) to calculate plasmonic properties of nanostructures having various geometry.[12,33,34] In 1951, Turkevich synthesized Au nanospheres by reducing chloroauric acid ($HAuCl_4$) using sodium citrate, which is the most popular method till date.[35] The growth of Au nanoparticles with time is shown in **Figure 1.3**.

After that, various synthetic strategies were developed. For example, Brust and Schiffrin used thiol ligands to obtain 1.5-5 nm Au nanospheres where strong thiol-gold interaction was used to stabilize gold nanoparticles**.**[36] Significant literatures are available, which demonstrate that various functional ligands like amines ligands (irrespective of being primary, secondary or quaternary), thiol/thiolated ligands, phosphine, amino acids, carboxylate ligands, hydroquinone, proteins etc. can be used to synthesize Au nanospheres.[37-47] Metal nanospheres generally show optical extinction maximum at the localized surface plasmon resonance frequency that occurs at the visible wavelength in case of noble metal nanospheres. Au nanospheres having size 50 nm show a ruby red color due to absorption of light where the resonance of its SPR band and incident light (of wavelength near 520 nm) can take place.[48]

Therefore, because of the tunable properties including high surface to volume ratio, optoelectronic properties and wide functionalization scopes Au nanospheres offer platforms for catalysis, surface-enhanced spectroscopic studies, sensing studies, drug carrier system, plasmon assisted hot-carrier, detection of biological targets, therapy etc.[49-54]

TH-2949_166122105

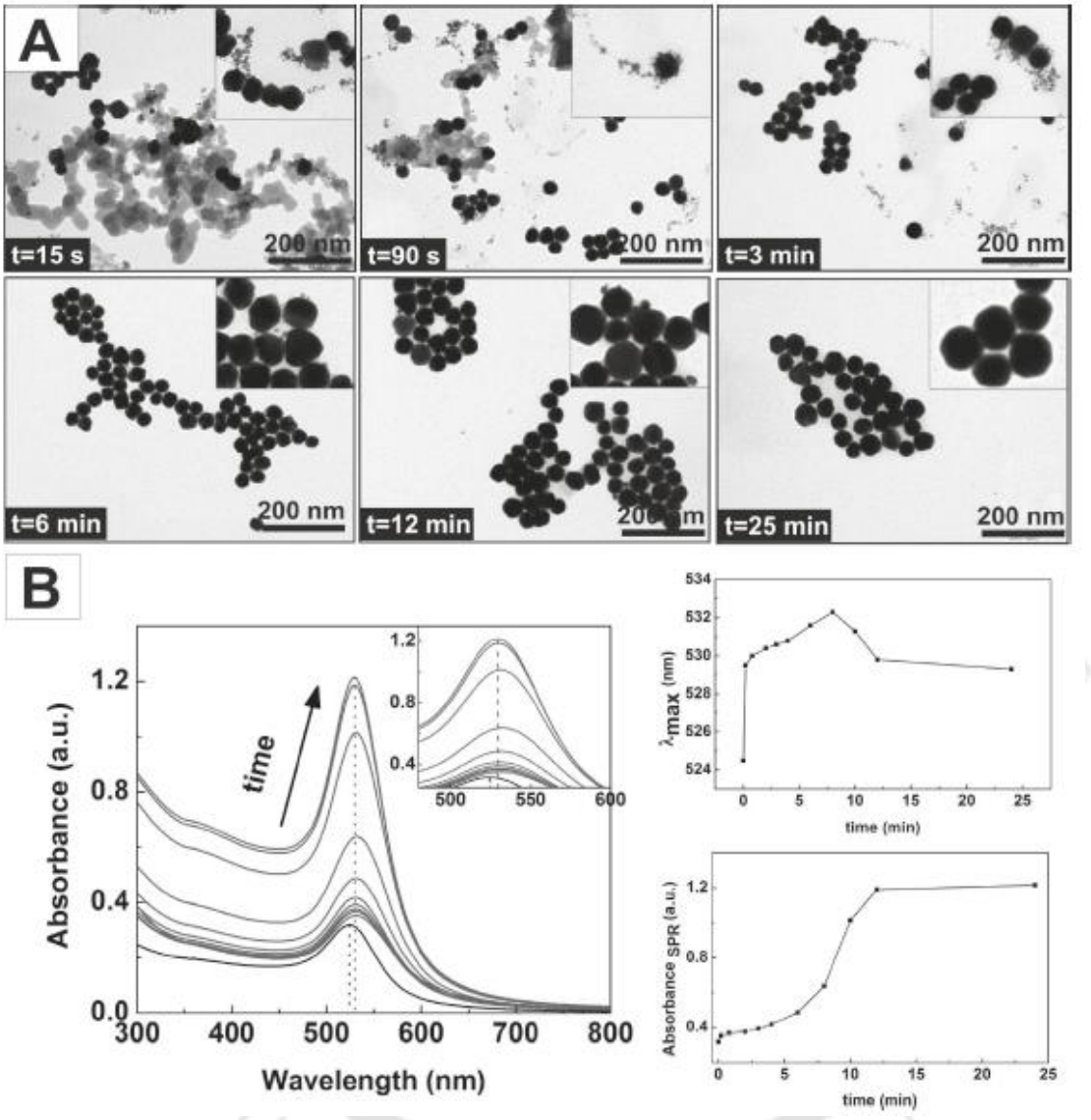

Figure 1.3. TEM images (A) and the corresponding UV-Vis spectra of the growth of Au nanoparticles as a function of time. Adapted with permission from reference 115. Copyright 2011 American Chemical Society.

1.4. Gold Nanorods

Various synthetic methods for gold and silver nanospheres were available since Chinese dynasties and Roman empire.[55-57] However, nonspherical or anisotropic metal nanostructures have been synthesized within the last two decades.[55-64] Gold nanorod (Au nanorod) was first synthesized using "hard template" (such as porous polycarbonate or

TH-2949_166122105

alumina membrane) in the mid-1990s and since then it has achieved the most attention among all anisotropic metal nanostructures.[55-57,63,65,66] After that a three-step convenient seeded growth approach was used to prepare gold nanorods having aspect ratios between 8 and 20 (**Figure 1.4**).[55,57,65,66]

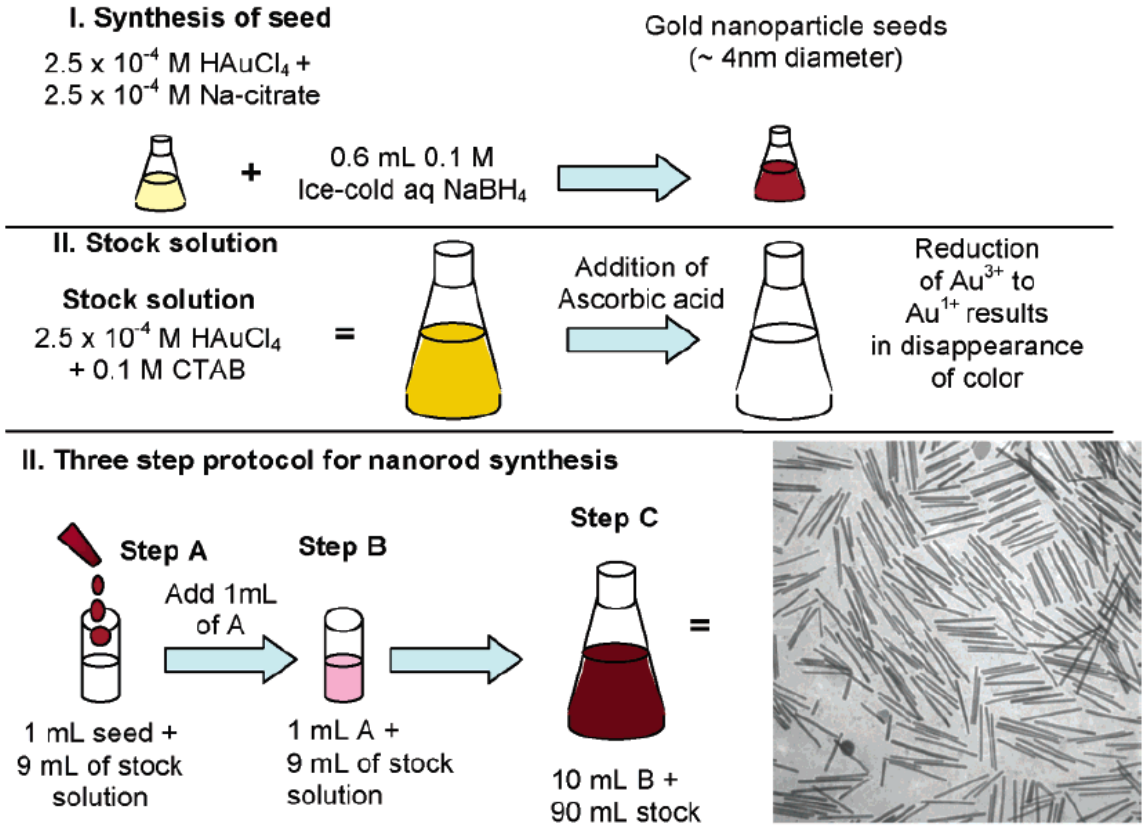

Figure 1.4. Seed-mediated growth approach for the synthesis of Au nanorods along with TEM image of Au nanorods. Adapted with permission from reference 59. Copyright 2005 American Chemical Society.

Out of all the synthetic methods, silver (Ag) assisted seeded growth approach is the most popular one till date.[67] Anisotropic metal nanostructures exhibit interesting shape dependent optical phenomena, which are not observed in spherical nanostructures.[55-58] In the UV-Vis spectrum, Au nanorod shows two plasmon bands (one for transverse plasmon and other band for longitudinal plasmon) and the longitudinal mode is significantly influenced by aspect

TH-2949_166122105

ratio of the Au nanorods.[55-58] In case of Au nanospheres the SPR energy is almost not dependent on its core diameter but for Au nanorods, longitudinal SPR energy is strongly dependent on its aspect ratio.[55-58,68-72] The wavelength of longitudinal SPR can be controlled from ~600 nm to ~1600 nm in the electromagnetic spectrum.[69-72] Light scattering of "large" Au nanorod is more as compared to "small" Au nanorod.[69-72] Thus, the extinction coefficient (ε) for larger Au nanorods is higher than the smaller Au nanorods.[72]

Like Au nanospheres, Au nanorods also can generate plasmon electromagnetic field under light illumination and thus it can be used to measure SERS spectra of chemical species present at the surface of Au nanorods.[73-77] Therefore, Au nanorod can be used as a potential candidate to enable plasmon-enhanced spectroscopies, sensing applications, photothermal therapy and biomedical imaging.[78-82]

1.5. Applications of Metal Nanostructures in Chemical Reactions

SPR is the unique optical property of metal nanoparticles (e.g., Au, Ag, and Cu nanoparticles).[83-85] Under the localized SPR excitation, electromagnetic field is coupled to the coherent oscillation of all free electrons on the surface.[86,87] Metal nanoparticles have significantly higher absorption cross section compared to any typical dye-sensitizer.[88] In addition, optical properties of plasmonic nanosructures can be tuned (by controlling their shape and size).[85,89] After excitation, non-radiative SPR dephasing generates hot electrons and hot holes having lifetime in the range of 1-100 fs that can take part in photochemical reactions.[90-93]

When metal nanoparticles absorb photons, hot carriers are generated because of electron transition. Here the momentum is conserved above the inter-band (transitions) threshold energies when the size of the plasmonic metal nanoparticle is less than half-wavelength of the incident radiation.[94,91] These hot electrons undergo interaction with the molecules present at the surface of metal nanoparticles (**Figure 1.5**).[90,94-99] Although, initially the hot electrons and hot holes are in a non-thermal distribution, they quickly thermalize according to Fermi−Dirac (F-D) distribution and that produces higher lattice temperature.[90,98,100] Then the heat gradually spreads to the surroundings (100 ps − 10 ns).[90,101] These highly energetic electrons of metal nanoparticles can be transferred to the adsorbate molecule that has

TH-2949_166122105

electron accepting orbital. This electron transfer occurs using two pathways – indirect transfer and direct transfer (**Figure 1.5**).[102,103, 104,105] In indirect electron transfer mechanism, after hot carrier generation the hot electrons are transferred into the LUMO of adsorbate, but in direct electron transfer mechanism a new dephasing channel – known as CID (chemical interface damping) – induces the direct hot electron generation in the adsorbate's electron accepting orbitals.[98,103,104,106] For both indirect and direct electron transfer from metal nanostructures to adsorbates require orbital overlap.[107, 108]For effective usage of hot electrons in photochemical reactions two major concerns need to be addressed – back-transfer process and thermalization. Electron-transfer from plasmonic metal nanostructure to adsorbate rises the electron density in vacant molecular orbitals of adsorbate molecule and that results in new features in the Raman spectrum.[109-111]

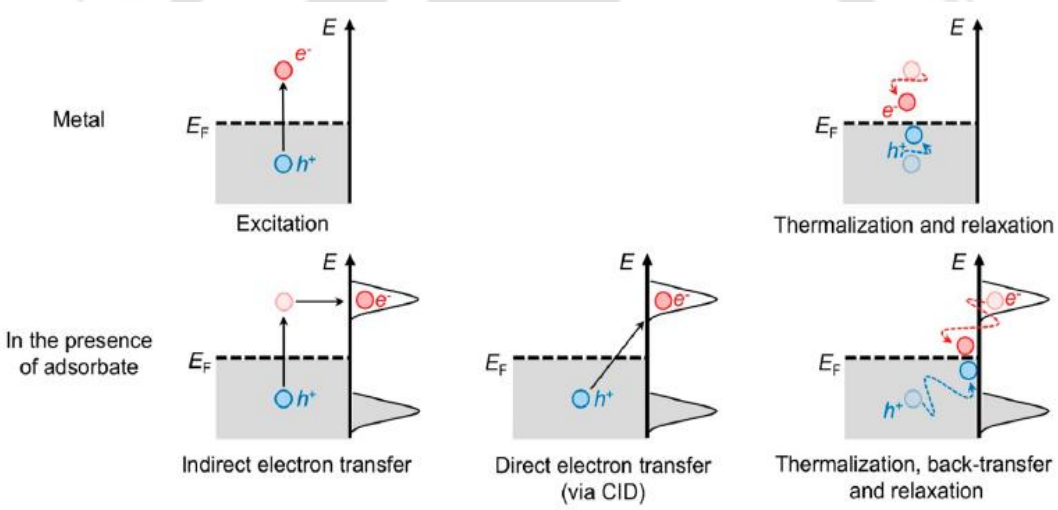

Figure 1.5. Hot carriers generation and hot electron (e^-) transfer (direct and indirect) and back-transfer processes in metal and metal/adsorbate systems. E_F represents the Fermi level of metal and the right component (relative to energy y-axis) represents the HOMO and LUMO for adsorbate. The gray parts illustrate the population of electronic states. Adapted with permission from reference 14. Copyright 2018 American Chemical Society.

Literatures show that hot-electron can induce photochemical transformation of adsorbate molecule on plasmonic-nanostructures.[94,112,95,98,103,104,113] Hot electron driven photochemical reactions on the metal nanostructures can effectively use visible light.[114] Since absorption characteristics of metal nanostructures are tunable (on the basis of shape and size),

TH-2949_166122105

combining metal nanostructures having different morphologies results in full-spectrum photocatalysts.[115-121] Hot-electron driven photochemical transformation on plasmonic metal nanostructures was first studied on 4-aminothiophenol (4-ATP) using SERS spectra.[113,122] Two strong peaks appeared in the SERS spectrum when 4-ATP attached metal nanostructures (e.g., Au or Ag nanoparticles) were irradiated with appropriate light. These peaks were not present in the Raman spectrum of 4-ATP.[122] Both electromagnetic (EM) and chemical enhancement (CE) mechanisms were unsuccessful to explain the above observation.[113] The appearance of these two peaks indicated the formation of a new molecular species, 4,4′ dimercaptoazobenzene (DMAB), due to the hot-electron-induced coupling of nearby 4-ATP molecules.[113,123-130]

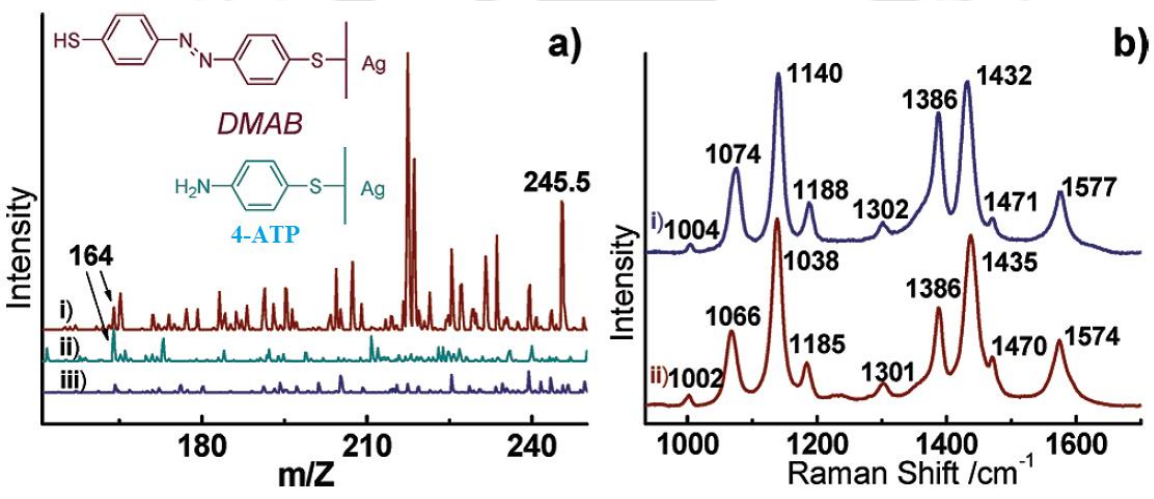

Figure 1.6. (**a**) DESI-MS spectra of 4-ATP attached at Ag electrodes irradiated with laser (i) and without any illumination (ii) and Ag free of 4-ATP (iii). (**b**) SERS spectra of 4-ATP (i) and DMAB (ii) on the Ag electrode. Adapted with permission from reference 124. Copyright 2010 American Chemical Society.

Several researchers developed effective plasmonic reactor systems to understand the mechanism of plasmon catalyzed reactions. For example, the role of oxygen was discovered in azo-coupling of dibenzo-1,2-dithiine-3,8-diamine on the basis of typical Raman spectrum and SERS spectrum.[131] Interestingly, most of the modern research are focused on the mechanism of plasmon induced photochemical reactions. There is a need to improve the kinetic efficiency of such reactions. At the hot spot region generation of hot electrons are much higher compared to the surface of metal nanostructure.[132-134] Thus, any plasmon driven

TH-2949_166122105

photochemical reaction ought to have enhanced rate at the hot spot compared to that at other regions of the surface of nanostructure and that is yet to be reported. One of the most popular plasmon induced photochemical reactions is the conversion of 4-ATP into DMAB (**Figure 1.6**).[135-137] **Figure 1.6a** shows DESI-MS (desorption electrospray ionization mass spectrometry) spectra of 4-ATP attached at Ag electrodes irradiated with laser and that suggested the formation of DMAB. This reaction is influenced by laser excitation wavelength and intensity, pH, O_2, solvent and the nature of metal nanostructure.[138-148] There is a report that describes that only four metal ions (Au^{3+}, Ag^{+}, Hg^{2+} and Pt^{4+}) can drive the conversion of 4-ATP to DMAB[149] and the role of metal ions in the conversion is discussed elaborately in Chapter 3. Thus there is a need to explore this photochemical reaction in presence of other metal ions also and that would present the versatility and generality of the idea.

On the other hand, applications of metal nanostructures are not limited to the plasmon catalyzed reactions only. Molecular vibrations having low change in polarizability can be probed in the presence of plasmonic metal surface. Moreover, Raman scattering intensity is enhanced by multiple orders of magnitude under resonance condition.[150,151] The combination of the two - SERS and resonance Raman - is termed as surface-enhanced resonance Raman scattering (SERRS). SERRS provides the best opportunity to pursue vibrational probes at single molecule level.[150-155] Nevertheless, SERRS can characterize the bonding, structure and kinetics of formation of various complexes that are not acquiescent to many other spectroscopic techniques. Many inorganic complexes, for example, vitamin B_{12}, non-heme dioxygenase, 2-picolylamine based cobalt complexes, peroxo complexes etc. are important to understand biological functions, anti-tumor activities etc. and are appropriate candidates for study on the basis of SERRS.

Next, heavy water (D_2O) has a significant role in various fields such as nuclear reactor,[156-158] solvents used in infrared (IR) and nuclear magnetic resonance (NMR) spectroscopy,[159-161] preservation of pancreas[162] etc. Thus the purity of D_2O is vital for these applications,[163] but the discrimination between H_2O and D_2O is extremely difficult due to their almost identical size and shape.[164] Several well-known methods such as atomic absorption spectroscopy (AAS), NMR, FTIR, fluorescence and infrared laser spectroscopy may not be suitable to distinguish H_2O and D_2O.[165-171] This is because of time-consuming sample

TH-2949_166122105

preparation and detection, non-portability, expensive test cost, complex operation, complex sample preparation etc.[171] Moreover, conventional Raman spectroscopy produces broad characteristic peak associated with 5 different vibrations for pure D_2O or H_2O.[172-175] The peak broadness and Raman scattering for H_2O are higher compared to that of D_2O.[172-175] In addition, conventional Raman spectroscopy cannot distinguish HOD from H_2O and D_2O signals in their mixture. Thus, there is a need of such a system that can detect H_2O, D_2O and HOD at the same time in the same reaction mixture using single vibrational mode-based Raman spectrum. This would be highly beneficial if metal nanostructure-based Raman scattering would provide better signal-to-noise ratio in such a probe.

1.6. Salient Features of the Thesis

Although nanomaterials have been utilized in modern nanoscience and technology since last few decades, still there is huge scope to explore new science with the help of metal nanostructures. This is where the current thesis reports some of the important results of pursuing Raman spectroscopy using metal nanostructures, especially those involving chemical reactions using the plasmonic field.

The key objectives of the current thesis are:

- At hot spot region due to plasmon coupling significant enhancement of electric field occurs. If we pursue a photochemical reaction selectively at the hot spot region of assembled nanostructure, what will happen with the rate constant of that reaction? How it will be different when the same reaction is carried out at the surface (non- hot spot region) of non-assembled metal nanostructure?
- Since metal cation can accept electron, what will be the effect of transition metal cations on the plasmon induced photochemical reaction? Can metal cation increase the product yield of a photochemical reaction?
- How can one utilize SERRS to identify the structure of amorphous inorganic complex? What is the role of metal nanostructure on the rate of inorganic bridged complex formation?
- How can H_2O, D_2O and HOD be simultaneously detected in a single Raman spectrum using vibrational mode?

TH-2949_166122105

We carried out experiments addressing all the above issues and the corresponding results are presented in the following chapters of this thesis.

1.7. References

1. Tee, S. Y.; Ye, E. *Mater. Adv.* **2021**, *2*, 1507-1529.

2. Zhou, Z. Y.; Tian, N.; Li, J. T.; Broadwell, I.; Sun, S. G. *Chem. Soc. Rev.* **2011**, *40*, 4167-4185.

3. Zhou, K.; Li, Y. *Angew Chem. Int. Ed*. **2012**, *51*, 602-613.

4. Jain, P.K.; Huang, X.; El-Sayed, I. H.; El-Sayed, M. A. *Acc. Chem. Res.* **2008**, *41*, 1578-1586.

5. Chen, H. M.; Liu, R. S. *J. Phys. Chem. C* **2011**, *115*, 3513-3527.

6. Dreaden, E. C.; Alkilany, A. M.; Huang, X.; Murphy, C.J.; El-Sayed, M. A. *Chem. Soc. Rev.* **2012**, *41*, 2740-2779.

7. Lohse, S. E.; Murphy, C. J. *J. Am. Chem. Soc.* **2012**, *134*, 15607-15620.

8. Rao, C. N.; Ramakrishna Matte, H. S.; Voggu, R.; Govindaraj, A. *Dalton Trans.* **2012**, *41*, 5089-5120.

9. Khan, I.; Saeed, K.; Khan, I. *Arabian J. Chem.* **2019**, *12*, 908-931.

10. Faraday, M. *Philos. Trans.* **1857**, *147*, 145–181.

11. Au, L.; Chen, Y.; Zhou, F.; Camargo, P.H.; Lim, B.; Li, Z. Y.; Ginger, D. S.; Xia, Y. *Nano Res.* **2008**, *1*, 441-449.

12. Eustis, S.; El-Sayed, M. A. *Chem. Soc. Rev.* **2006**, *35*, 209.

13. Jones, M. R.; Osberg, K. D.; Macfarlane, R. J.; Langille, M. R.; Mirkin, C. A. *Chem. Rev.* **2011**, *111*, 3736.

14. Zhang, Y.; He, S.; Guo, W.; Hu, Y.; Huang, J.; Mulcahy, J. R.; Wei, W. D. *Chem. Rev.* **2018**, *118*, 2927-2954.

15. Noguez, C. *J. Phys. Chem. C*. **2007**, *111*, 3806.

16. Link, S.; El-Sayed, M. A. *J. Phys. Chem. B* **1999**, *103*, 8410.

17. Campion, A.; Kambhampati, P. *Chem. Soc. Rev.* **1998**, *27*, 241.

18. Merlen, A.; Lagugne´-Labarthet, F.; Harte, E. *J. Phys. Chem. C* **2010**, *114*, 12878.

TH-2949_166122105

19. Lakowicz, J. R.; Geddes, C. D.; Gryczynski, I.; Malicka, J.; Gryczynski, Z.; Aslan, K.; Lukomska, J.; Matveeva, E.; Zhang, J.; Ramachandram, B.; Huang, J. *Journal of Fluorescence* **2004**, *14*, 425.

20. Quinn, B. M.; Liljeroth, P.; Ruiz, V.; Laaksonen, T.; Kontturi, K. *J. Am. Chem. Soc.* **2003**, *125*, 6644.

21. Hao, E.; Schatz, G. C. *J. Chem. Phys.* **2004**, *120*, 357.

22. Dutta, A.; Chattopadhyay, A. *J. Phys. Chem. C* **2017**, *121*, 18854-18861.

23. Whitesides, G. M.; Grzybowski, B. *Science* **2002**, *295*, 2418-2421.

24. Deng, Z.; Tian, Y.; Lee, S. H.; Ribbe, A. E.; Mao, C. *Angew. Chem. Int. Ed*. **2005**, *44*, 3582-3585.

25. Mezour, M. A.; Perepichka, I. I.; Zhu, J.; Lennox, R. B.; Perepichka, D. F. *ACS Nano* **2014**, *8*, 2214-2222.

26. Nykypanchuk, D.; Maye, M. M.; van der Lelie, D.; Gang, O. *Nature* **2008**, *451*, 549-552.

27. Gramotnev, D. K.; Bozhevolnyi, S. I. *Nat. Photonics* **2010**, *4*, 83-91.

28. Atwater, H. A.; Polman, A. *Nat. Mater.* **2010**, *9*, 205-213.

29. Schuller, J. A.; Barnard, E. S.; Cai, W.; Jun, Y. C.; White, J. S.; Brongersma, M. L. *Nat. Mater.* **2010**, *9*, 193-204.

30. Wang, X.; Li, M.; Meng, L.; Lin, K.; Feng, J.; Huang, T.; Yang, Z.; Ren, B. *ACS Nano* **2014**, *8*, 528-536.

31. Saha, K.; Agasti, S. S.; Kim, C.; Li, X.; Rotello, V. M. *Chem. Rev*. **2012**, *112*, 2739.

32. Mie, G. *Ann. Phys.* **1908**, *25*, 377.

33. Kelly, K. L.; Coronado, E.; Zhao, L. L.; C. Schatz, G. C. *J. Phys. Chem. B* **2003**, *107*, 668-677.

34. Ghosh, S. K.; Pal, T. *Chemical Reviews* **2007**, *107*, 4797.

35. Turkevich, J.; Stevenson, P. C.; Hillier, J. Discuss. *Faraday Soc*. **1951**, *11*, 55.

36. Brust, M.; Walker, M.; Bethell, D.; Schiffrin, D. J.; Whyman, R. *J. Chem. Soc. Chem. Commun.* **1994**, 801.

37. Cappellari, P. S.; Buceta, D.; Morales, G. M.; Barbero, C. A.; Moreno, M. S.; Giovanetti, L. J.; Ramallo-López, J. M.; Requejo, F. G.; Craievich, A. F.; Planes, G. A. *J. Colloid Interface Sci.* **2015**, 441, 17.

TH-2949_166122105

38. Shelley, E. J.; Ryan, D.; Johnson, S. R.; Couillard, M.; Fitzmaurice, D.; Nellist, P. D.; Chen, Y.; Palmer, R. E.; Preece, J. A. *Langmuir* **2002**, *18*, 1791.

39. Leff, D. V.; Brandt, L.; Heath, J. R. *Langmuir* **1996**, *12*, 4723.

40. Chen, S.; Liu, Y.; Wu, G. *Nanotechnology* **2005**, *16*, 2360.

41. Weare, W. W.; Reed, S. M.; Warner, M. G.; Hutchison, J. E. *J. Am. Chem. Soc.* **2000**, *122*, 12890.

42. Sarkar, A.; Shukla, S. P.; Adhikari, S.; Mukherjee, T. *Int. J. Nano. Technol* **2010**, *7*, 1027.

43. Matei, I.; Buta, C. M.; Turcu, I. M.; Culita, D.; Munteanu, C.; Ionita, G. *Molecules* **2019**, *24*, 3395.

44. Bhargava, S. K.; Booth, J. M.; Agrawal, S.; Coloe, P.; Kar, G. *Langmuir* **2005**, *21*, 5949.

45. Selvakannan, P.; Mandal, S.; Phadtare, S.; Gole, A.; Pasricha, R.; Adyanthaya, S. D.; Sastry, M. J. *Colloid Interface Sci*. **2004**, *269*, 97.

46. Housni, A.; Ahmed, M.; Liu, S.; Narain, R. *J. Phys. Chem. C* **2008**, *112*, 12282.

47. Sirajuddin; Mechler, A.; Torriero, A. A. J.; Nafady, A.; Lee, C. Y.; Bond, A. M.; O' Mullane, A. P.; Bhargava, S. K. *Colloids Surf. A* **2010**, *370*, 35.

48. Xia, Y.; Halas, N. J. *MRS Bull*. **2005**, *30*, 338.

49. Astruc, D. *Chem. Rev.* **2020**, *120*, 461-463.

50. Yang, X.; Yang, M.; Pang, B.; Vara, M.; Xia, Y. *Chem. Rev*. **2015**, *115*, 10410.

51. Wang X.; Li, Maohua.; Meng, L.; Lin, K.; Feng, J.; Huang, T.; Yang, Z.; Ren, B. *ACS Nano* **2014**, *8*, 528.

52. Aslan, K.; Lakowicz, J. R.; Geddes, C. D. *Anal. Biochem.* **2004**, *330*, 145.

53. Zhao, J.; Nguyen, S. C.; Ye, R.; Ye, B.; Weller, H.; Somorjai, G. A.; Alivisatos, A. P.; Toste, F. D. *ACS Cent. Sci.* **2017**, *3*, 482.

54. Khandelia, R.; Jaiswal, A.; Ghosh, S. S.; Chattopadhyay, A. *J. Mater. Chem. B* **2014**, *2*, 6472.

55. Reguera, J.; Langer, J.; Aberasturi, D. J. D.; Liz-Marzan, L. M. *Chem. Soc. Rev*. **2017**, *46*, 3866-3885.

56. Dreaden, E. C.; Alkilany, A. M.; Huang, X.; Murphy, C. J.; El- Sayed, M. A. *Chem. Soc. Rev.* **2012**, *41*, 2740-2779.

57. Eustis, S.; El-Sayed, M. A. *Chem. Soc. Rev.* **2006**, *35*, 209-217.

TH-2949_166122105

58. Hulteen, J. C.; Martin, C. R. *J. Mater. Chem.* **1997**, *7*, 1075-1087.

59 Murphy, C. J.; Sau, T. K.; Gole, A. M.; Orendorff, C. J.; Gao, J.; Gou, L.; Hunyadi, S. E.; Li, T. *J. Phys. Chem. B* **2005**, *109*, 13857-13870.

60. Vigderman, L.; Khanal, B. P.; Zubarev, E. R. *Adv. Mater.* **2012**, *24*, 4811-4841.

61. Grzelczak, M.; Perez-Juste, J.; Mulvaney, P.; Liz-Marzan, L. M. *Chem. Soc. Rev.* **2008**, *37*, 1783-1791.

62. Langille, M. R.; Personick, M. L.; Zhang, J.; Mirkin, C. A. *J. Am. Chem. Soc*. **2012**, *134*, 14542-14554.

63. Burda, C.; Chen, X.; Narayanan, R.; El-Sayed, M. A. *Chem. Rev.* **2005**, *105*, 1025-1102.

64. Murphy, C. J.; Thompson, L. B.; Alkilany, A. M.; Sisco, P. N.; Boulos, S. P.; Sivapalan, S. T.; Yang, J. A.; Chernak, D. J.; Huang, J. *J. Phys. Chem. Lett.* **2010**, *1*, 2867-2875.

65. Murphy, C. J.; Gole, A. M.; Hunyadi, S. E.; Orendorff, C. *J. Inorg. Chem.* **2006**, *45*, 7544−7554.

66. Perez-Juste, J.; Pastoriza-Santos, I.; Liz-Marzan, L. M.; Mulvaney, P. *Coord. Chem. Rev.* **2005**, *249*, 17-1901.

67. Nafisah, S.; Morsin, M.; Jumadi, N. A.; Nayan, N.; Shah, N. Z. A. M.; Razali, N. L.; Soon, C. F. *International Journal of Engineering & Technology* **2018**, *7*, 121-125.

68. Jain, P. K.; El-Sayed, M. A. *Nano Lett.* **2007**, *7*, 2854-2858.

69. Orendorff, C. J.; Murphy, C. J. *J. Phys. Chem. B* **2006**, *110*, 3990-3994.

70. Ali, M. R. K.; Snyder, B.; El-Sayed, M. A. *Langmuir* **2012**, *28*, 9807-9815.

71. Prescott, S. W.; Mulvaney, P. *J. App. Phys*. **2006**, *99*, 123504-123507.

72. Link, S.; El-Sayed, M. A. *J. Phys. Chem. B* **1999**, *103*, 8410-8426.

73. Novo, C.; Funston, A. M.; Mulvaney, P. *Nat. Nanotechnol*. **2008**, *3*, 598-602.

74. Nusz, G. J.; Marianakos, S. M.; Curry, A. C.; Dahlin, A.; Hk, F.; Wax, A.; Chilkoti, A. *Anal. Chem*. **2008**, *80*, 984-989.

75. Gabudean, A. M.; Focsan, M.; Astilean, S. *J. Phys. Chem. C* **2012**, *116*, 12240-12249.

76. Lee, C. H.; Hankus, M. E.; Tian, L.; Pellegrino, P. M.; Singamaneni, S. *Anal. Chem*. **2011**, *83*, 8953-8958.

77. Zhao, T.; Wu, H.; Yao, S. Q.; Xu, Q.-H.; Xu, G. Q. *Langmuir* **2010**, *26*, 14937-14942.

78. O'Neal, D. P.; Hirsch, L. R.; Halas, N. J.; Payne, J. D.; West, J. L. *Cancer Lett.* **2004**, *209*, 171-176.

TH-2949_166122105

79. Loo, C.; Lowery, A.; Halas, N.; West, J.; Drezek, R. *Nano Lett.* **2005**, *5*, 709-711.

80. Huang, X.; El-Sayed, I. H.; Qian, W.; El-Sayed, M. A. *J. Am. Chem. Soc*. **2006**, *128*, 2115-2120.

81. Dreaden, E. C.; Gryder, B. E.; Austin, L. A.; Tene Defo, B. A.; Hayden, S. C.; Pi, M.; Quarles, L. D.; Oyelere, A. K.; El-Sayed, M. A. *Bioconjugate Chem.* **2012**, *23*, 1507-1512.

82. Kennedy, L. C.; Bickford, L. R.; Lewinski, N. A.; Coughlin, A. J.; Hu, Y.; Day, E. S.; West, J. L.; Drezek, R. A. *Small* **2011**, *7*, 169-183.

83. Giannini, V.; Fernández-Domínguez, A. I.; Heck, S. C.; Maier, S. A. *Chem. Rev.* **2011**, *111*, 3888-3912.

84. Hartland, G. V. *Chem. Rev.* **2011**, *111*, 3858-3887.

85. DuChene, J. S.; Niu, W.; Abendroth, J. M.; Sun, Q.; Zhao, W.; Huo, F.; Wei, W. D. *Chem. Mater.* **2013**, *25*, 1392-1399.

86. Willets, K. A.; Van Duyne, R. P. *Annu. Rev. Phys. Chem.* **2007**, *58*, 267-297.

87. Wu, C.; Zhou, X.; Wei, J. *Nanoscale Research Letters* **2015**, *10*, 354.

88. Jain, P. K.; Lee, K. S.; El-Sayed, I. H.; El-Sayed, M. A. *J. Phys. Chem. B* **2006**, *110*, 7238-7248.

89. Brongersma, M. L.; Halas, N. J.; Nordlander, P. *Nat. Nanotechnol.* **2015**, *10*, 25-34.

90. Khurgin, J. B. *Nat. Nanotechnol.* **2015**, *10*, 2-6.

91. Landau, L. *J. Phys.* **1946**, *10*, 25-34.

92. Liu, Y.; Chen, Q.; Cullen, D. A.; Xie, Z.; Lian, T. *Nano Lett.* **2020**, *20*, 4322-4329.

93. Brown, A. M.; Sundararaman, R.; Narang, P.; Goddard, W. A.; Atwater, H. A. *ACS Nano* **2016**, *10*, 957-966.

94. Linic, S.; Aslam, U.; Boerigter, C.; Morabito, M. *Nat. Mater*. **2015**, *14*, 567-576.

95. Christopher, P.; Xin, H.; Linic, S. *Nat. Chem.* **2011**, *3*, 467-472.

96. Christopher, P.; Xin, H.; Marimuthu, A.; Linic, S. *Nat. Mater*. **2012**, *11*, 1044-1050.

97. Naldoni, A.; Shalaev, V. M.; Brongersma, M. L. *Science* **2017**, *356*, 908-909.

98. Kale, M. J.; Avanesian, T.; Christopher, P. *ACS Catal.* **2014**, *4*, 116-128.

99. Christopher, P.; Moskovits, M. *Annu. Rev. Phys. Chem.* **2017**, *68*, 379-398.

100. Voisin, C.; Del Fatti, N.; Christofilos, D.; Vallée, F. *J. Phys. Chem. B* **2001**, *105*, 2264-2280.

TH-2949_166122105

101. Furube, A.; Du, L.; Hara, K.; Katoh, R.; Tachiya, M. *J. Am. Chem. Soc.* **2007**, *129*, 14852-14853.

102. Wu, K.; Chen, J.; McBride, J. R.; Lian, T. *Science* **2015**, *349*, 632-635.

103. Boerigter, C.; Campana, R.; Morabito, M.; Linic, S. *Nat. Commun.* **2016**, *7*, 10545.

104. Boerigter, C.; Aslam, U.; Linic, S. *ACS Nano* **2016**, *10*, 6108-6115.

105. Long, R.; Prezhdo, O. V. *J. Am. Chem. Soc.* **2014**, *136*, 4343-4354.

106. Persson, B. N. J. *Surf. Sci.* **1993**, *281*, 153-162.

107. Mukherjee, S.; Libisch, F.; Large, N.; Neumann, O.; Brown, L. V.; Cheng, J.; Lassiter, J. B.; Carter, E. A.; Nordlander, P.; Halas, N. J. *Nano Lett.* **2013**, *13*, 240-247.

108. Lindstrom, C. D.; Zhu, X. Y. *Chem. Rev.* **2006**, *106*, 4281-4300.

109. Osawa, M.; Matsuda, N.; Yoshii, K.; Uchida, I. *J. Phys. Chem*. **1994**, *98*, 12702-12707.

110. Hogiu, S.; Werncke, W.; Pfeiffer, M.; Elsaesser, T. *Chem. Phys. Lett.* **1999**, *312*, 407-414.

111. Gersten, J. I.; Birke, R. L.; Lombardi, J. R. *Phys. Rev. Lett.* **1979**, *43*, 147-150.

112. Mukherjee, S.; Zhou, L.; Goodman, A. M.; Large, N.; Ayala- Orozco, C.; Zhang, Y.; Nordlander, P.; Halas, N. J. *J. Am. Chem. Soc.* **2014**, *136*, 64-67.

113. Wu, D.; Liu, X.; Huang, Y.; Ren, B.; Xu, X.; Tian, Z. *J. Phys. Chem. C* **2009**, *113*, 18212-18222.

114. Willis, D. E.; Taheri, M. M.; Kizilkaya, O.; Leite, T. R.; Zhang, L.; Ofoegbuna, T.; Ding, K.; Dorman, J. A.; Baxter, J. B.; McPeak, K. M. *ACS Appl. Mater. Interfaces* **2020**, *12*, 22778-22788.

115. Bastús, N. G.; Comenge, J.; Puntes, V. *Langmuir* **2011**, *27*, 11098-11105.

116. Tian, F.; Bonnier, F.; Casey, A.; Shanahan, A. E.; Byrne, H. J. *Anal. Methods*, **2014**, *6*, 9116-9123.

117. Yang, H.; Wang, Z.; Zheng, Y.; He, L.; Zhan, C.; Lu, X.; Tian, Z.; Fang, P.; Tong, Y. *J. Am. Chem. Soc.* **2016**, *138*, 16204-16207.

118. Pu, Y.; Wang, G.; Chang, K.; Ling, Y.; Lin, Y.; Fitzmorris, B. C.; Liu, C.; Lu, X.; Tong, Y.; Zhang, J. Z.; Hsu, Y. J.; Li, Y. *Nano Lett*. **2013**, *13*, 3817-3823.

119. Meng, X.; Liu, L.; Ouyang, S.; Xu, H.; Wang, D.; Zhao, N.; Ye, J. *Adv. Mater*. **2016**, *28*, 6781-6803.

TH-2949_166122105

120. Liu, L.; Ouyang, S.; Ye, J. *Angew. Chem. Int. Ed.* **2013**, *52*, 6689-6693.

121. Xu, C.; Anusuyadevi, P. R.; Aymonier, C.; Luque, R.; Marre, S. *Chem. Soc. Rev.* **2019**, *48*, 3868-3902.

122. Osawa, M.; Matsuda, N.; Yoshii, K.; Uchida, I. *J. Phys. Chem.* **1994**, *98*, 12702-12707.

123. Wu, D.; Zhao, L.; Liu, X.; Huang, R.; Huang, Y.; Ren, B.; Tian, Z. *Chem. Commun*. **2011**, *47*, 2520-2522.

124. Huang, Y.; Zhu, H.; Liu, G.; Wu, D.; Ren, B.; Tian, Z. *J. Am. Chem. Soc*. **2010**, *132*, 9244-9246.

125. Huang, Y.; Fang, Y.; Yang, Z.; Sun, M. *J. Phys. Chem. C* **2010**, *114*, 18263-18269.

126. Fang, Y.; Li, Y.; Xu, H.; Sun, M. *Langmuir* **2010**, *26*, 7737-7746.

127. Zhao, L.; Huang, Y.; Liu, X.; Anema, J. R.; Wu, D.; Ren, B.; Tian, Z. *Phys. Chem. Chem. Phys.* **2012**, *14*, 12919-12929.

128. Zhao, L.; Zhang, M.; Huang, Y.; Williams, C. T.; Wu, D.; Ren, B.; Tian, Z. *J. Phys. Chem. Lett.* **2014**, *5*, 1259-1266.

129. Dong, B.; Fang, Y.; Xia, L.; Xu, H.; Sun, M. *J. Raman Spectrosc.* **2011**, *42*, 1205-1206.

130. Dong, B.; Fang, Y.; Chen, X.; Xu, H.; Sun, M. *Langmuir* **2011**, *27*, 10677-10682.

131. Zhang, Z.; Kinzel, D.; Deckert, V. *J. Phys. Chem. C* **2016**, *120*, 20978-20983.

132. Lucas V. Besteiro and Alexander O. Govorov. *J. Phys. Chem. C* **2016**, *120*, 19329-19339.

133. Zhang, Z.; Gaudig, T. D.; Singha, P.; Deckert, V. *Chem. Commun*. **2015**, *51*, 3069-3072.

134. Liu, X. L.; Liang, S.; Nan, F.; Yang, Z. J.; Yu, X. F.; Zhou, L.; Hao, Z. H.; Wang, Q. Q. *Nanoscale* **2013**, *5*, 5368.

135. Choi, H. K.; Shon, H. K.; Yu, H.; Lee, T. G.; Kim, Z. H. *J. Phys. Chem. Lett*. **2013**, *4*, 1079.

136. Huang, Y. F.; Zhu, H. P.; Liu, G. K.; Wu, D. Y.; Ren, B.; Tian, Z. Q. *J. Am. Chem. Soc.* **2010**, *132*, 9244.

137. Wu, D. Y.; Liu, X. M.; Huang, Y. F.; Ren, B.; Xu, X.; Tian, Z. Q. *J. Phys. Chem. C* **2009**, *113*, 18212.

138. Wang, J. L.; Ando, R. A.; Camargo, P. H. C. *ACS Catal*. **2014**, *4*, 3815.

139. Xu, J. F.; Luo, S. Y.; Liu, G. K. *Spectrochim. Acta, Part A* **2015**, *143*, 35.

TH-2949_166122105

140. Xu, P.; Kang, L.; Mack, N. H.; Schanze, K. S.; Han, X.; Wang, H. L. *Sci. Rep*. **2013**, *3*, 2997.

141. Sun, M.; Huang, Y.; Xia, L.; Chen, X.; Xu, H. *J. Phys. Chem. C* **2011**, *115*, 9629.

142. Canpean, V.; Astilean, S. *Spectrochim. Acta, Part A* **2012**, *96*, 862.

143. Xu, J. F.; Liu, G. K. *Spectrochim. Acta, Part A* **2015**, *138*, 873.

144. Qiao, Q.; Shan, C. X.; Zheng, J.; Zhu, H.; Yu, S. F.; Li, B. H.; Jia, Y.; Shen, D. Z. *Nanoscale* **2013**, *5*, 513.

145. Nelson, D. A.; Schultz, Z. D. *J. Phys. Chem. C* **2018**, *122*, 8581.

146. Wu, H. Y.; Lai, Y. H.; Hsieh, M. S.; Lin, S. D.; Li, Y. C.; Lin, T. W. *Adv. Mater. Interfaces* **2014**, *1*, 1400119.

147. Tan, E.; Yin, P.; Yu, C.; Yu, G.; Zhao, C. *Spectrochim. Acta, Part A* **2016**, *166*, 15.

148. Liu, Y.; Yang, D.; Zhao, Y.; Yang, Y.; Wu, S.; Wang, J.; Xia, L.; Song, P. *Heliyon* **2019**, *5*, e01545.

149. Zhang, Z.; Merk, V.; Hermanns, A.; Unger, W. E. S.; Kneipp, J. *ACS Catal*. **2017**, *7*, 7803.

150. Langer, J.; Jimenez De Aberasturi, D.; Aizpurua, J.; Alvarez-Puebla, R. A.; Auguié, B.; Baumberg, J. J.; Bazan, G. C.; Bell, S. E. J.; Boisen, A.; Brolo, A. G.; Choo, J.; Cialla-May, D.; Deckert, V.; Fabris, L.; Faulds, K.; García De Abajo, F. J.; Goodacre, R.; Graham, D.; Haes, A. J.; Haynes, C. L.; et al. *ACS Nano* **2020**, *14*, 28-117.

151. McLintock, A.; Lee, H. J.; Wark, A. W. *Phys. Chem. Chem. Phys*. **2013**, *15*, 18835-18843.

152. Sengupta, K.; Chatterjee, S.; Dey, A. *ACS Catal*. **2016**, *6*, 6838.

153. Faulds, K.; Littleford, R. E.; Graham, D.; Dent, G.; Smith, W. E. *Anal. Chem*. **2004**, *76*, 592.

154. Eng, L. H.; Schlegel, V.; Wang, D.; Neujahr, H. Y.; Stankovich, M. T.; Cotton, T. *Langmuir* **1996**, *12*, 3055.

155. Alexander, B. D.; Crayston, J. A.; Dines, T. J. *Phys. Chem. Chem. Phys*. **2004**, *6*, 3576-3584.

156. Rowinski, M. K.; White, T. J.; Zhao, J. Y. *Renewable Sustainable Energy Rev.* **2015**, *44*, 643.

157. Bromley, B. P.; Colton, A. V.; Golesorkhi, S.; *Ann. Nucl. Energy* **2019**, *124*, 399.

TH-2949_166122105

158. Kluge, H.; Weise, K.; Hunt, J. B.; *Radiat. Prot. Dosim*. **1990**, *32*, 233.

159. Roberts, J. D. *Nuclear Magnetic Resonance: applications to organic chemistry, McGraw-Hill Book Company*, **1959**.

160. Emsley, J.; Feeney, J.; Sutcliffe, L. H. *High Resolution Nuclear Magnetic Resonance Spectroscopy* **1995**, *2*.

161. Baenziger, J. E.; Methot, N. *J. Biol. Chem*. **1995**, *270*, 29129.

162. Hesse, U. J.; Gores, P. F.; et al. *Transplant. Proc*. **1987**, *19*, 4167.

163. Tcelykh, L.; Kozhevnikova (Khudoleeva), V.; Goloveshkin, A.; Lepnev, L.; Popelensky, Th.; Utochnikova, V. *Analyst* **2020**, *145*, 759.

164. Dunning, S. G.; Nunez, A. J.; Moore, M. D.; Steiner, A.; Lynch, V. M.; Sessler, J. L.; Holliday, B. J.; Humphrey, S. M. *Chem* **2017**, *2*, 579-589.

165. Meijer, G.; Meulen, J. J. T.; Andresen, P.; Bath, A. *J. Chem. Phys.* **1986**, *85*, 6914-6922.

166. Olson, D. L.; Lacey, M. E.; Webb, A. G.; Sweedler, J. V. *Anal. Chem.* **1999**, *71*, 3070.

167. Xiong, F. B.; Zhu, W. Z.; Lin, H. F. *Appl. Mech. Mater*. **2013**, *303*, 59.

168. Armani, A. M.; Vahala, K. J. *Opt. Lett.* **2006**, *31*, 1896.

169. Xiong, F. B.; Zhu, W. Z.; Meng, X. G.; Lin, H. F.; Huang, X. H.; Huang, Y. Q. *Optik* **2013**, *124*, 2008.

170. Park, K.; Lee, Y. K. K. J.; Radioanal, J. *Nucl. Chem*. **2019**, *322*, 487.

171. Dong, B.; Lu, Y.; Song, W.; Kong, X.; Sun, Y.; Lin, W. *Chem. Commun.* **2020**, *56*, 1191.

172. Hu, Q.; Zhao, H.; Ouyang, S. *Phys.Chem.Chem.Phys.* **2017**, *19*, 21540.

173. Hu, Q.; Ouyang, S.; Lia, J.; Cao, Z. *J. Raman Spectrosc*. **2017**, *48*, 610-617.

174. Baschenko, S. M.; Marchenko, L. S. *Semiconductor Physics, Quantum Electronics & Optoelectronics* **2011**, *14*, 77-79.

175. Zarei, A.; Klumbach, S.; Keppler, H. *ACS Earth Space Chem.* **2018**, *2*, 925-934.

TH-2949_166122105

TH-2949_166122105

CHAPTER 2

In this chapter we report a centrifugal force driven end-to-end assembly of gold nanorod (Au NR) via H-bonded interaction of para-aminothiophenol (4-ATP) selectively bound to the longitudinal ends of Au NRs. The plasmonic hot-spots generated due to Au NR assembly served as catalytic center for carrying out photochemical coupling reaction of 4-ATP to dimercaptoazobenzene (DMAB). We also demonstrate the degradation of DMAB in the presence of hydrogen peroxide (H_2O_2) at the plasmonic hot-spot. The coupling reaction was carried out at the hot-spot of the assembled Au NR upon surface plasmon excitation using 632.8 nm laser. SERS kinetic data indicated that the plasmon mediated coupling reaction was 1.6-fold faster at the plasmonic hot-spot of the assembled Au NRs than that on the surface of longitudinal end of Au NR. This, therefore, showed a new way of carrying out photocatalytic reactions at the plasmonic hot spot with higher reaction rate.

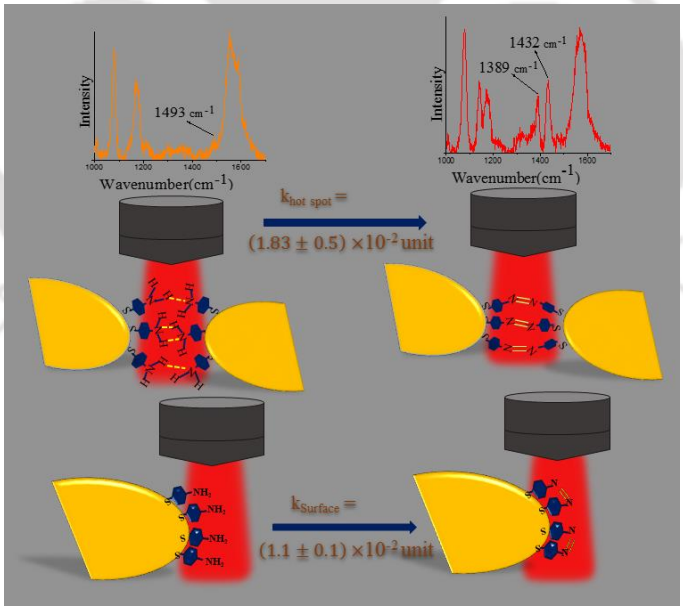

Ref.: Pal, S.; Dutta, A.; Paul, M.; Chattopadhyay, A. Plasmon-Enhanced Chemical Reaction at the Hot Spots of End-to-End Assembled Gold Nanorods. *J. Phys. Chem. C* 2020, *124*, 3204-3210.

TH-2949_166122105

2.1. Introduction

The electromagnetic field enhancement, due to SPR excitation in plasmonic metal nanostructures, provides a unique opportunity to detect and study molecules in the visible and infrared region, using the principle of SERS. On the other hand, the non-radiative decay of surface plasmons results in the generation of hot-electrons, which are capable of triggering chemical reaction within molecules adsorbed on the surface of metallic nanostructures.[1,2] In that regard, the plasmon driven photocatalysis has gained wide attention due to its high throughput, selectivity and most importantly low energy requirement in most of the organic conversion reactions.[3] In general, the excitation wavelength for typical organic conversion reaction lies in the ultraviolet region but proper selection of plasmonic catalyst allows one to tune the excitation energy to visible or the near infrared region (lower energy), irrespective of organic molecules involved.[4] Coincidentally, SERS provides us with the advantage of in-situ study of plasmon driven photocatalytic reactions – wherein the plasmonic nanostructure itself acts as photocatalyst and also provides large scattering cross section thus enhancing Raman scattering signal.[5]

The most widely studied plasmon driven surface catalytic reactions have been the oxidation of aromatic amine compounds and the reduction of nitro compounds, thus leaving opportunity to pursue other reactions.[1,6,7] Nevertheless, deeper understanding of the mechanism of SPR catalyzed reaction is essential and this has been under investigation by several research groups in order to develop efficient plasmonic reactor systems for investigating complex chemical reactions. For example, in the azo-coupling of dibenzo-1,2-dithiine-3,8-diamine (D3ATP) using normal Raman spectroscopy (NRS) and SERS conditions, the critical role of O_2 was revealed.[4] On the other hand, it has been reported that the plasmon assisted oxidative reaction of 4-ATP to dimercaptoazobenzene (DMAB) takes place via the formation of corresponding metal oxide.[8]

Interestingly, major attention for the reported plasmon assisted photocatalytic reactions has been on deciphering the mechanism of the catalytic reactions. On the other hand, there is also a need to probe the kinetic efficiency of such reactions. As mentioned earlier, the collective excitation of electrons on the metal surface generates the so called hot electrons, which are capable of driving photocatalytic reaction of molecules on the surface of plasmonic-nanostructures. In that sense, the coupling of surface plasmon at the nanogap of

TH-2949_166122105

the metallic nanostructures – leading to plasmonic hot-spot formation – ought to enhance the hot-electron generation significantly.[9,10, 11] This should also be capable of enhancing the rate of plasmon driven photocatalytic reaction at the hot-spot. Although the currently available literature presents a repertoire of such unique ways to generate different coupled plasmonic-nanostructures;[11-16] however field enhancement at the hot-spot based chemical catalysis is yet to be reported in the literature.

Herein we report plasmon driven photocatalytic conversion of 4-ATP to DMAB at the hot-spot of the longitudinal end-to-end assembled Au NRs and establish higher kinetic efficiency of the same reaction as compared to when carried out on the surface of non-assembled Au NR. The cetyltrimethyl ammonium bromides (CTAB) stabilized Au NRs were selectively functionalized with 4-ATP at their longitudinal ends. Interestingly, the 4-ATP molecule at longitudinal end of Au NR underwent facile dimerization via H-bonded interaction to generate linear assembly of Au NR upon centrifugation at 12000 rpm. Further, upon irradiation with 632.8 nm laser light, the dimerized 4-ATP, bridging the assembled Au NR, underwent chemical transformation to DMAB as the product via surface plasmon excitation at the hot-spot. This was reflected from the time-dependent SERS measurements recorded during the transformation of 4-ATP to DMAB. The results clearly indicated higher catalytic efficiency of the oxidative coupling reaction at the plasmonic hot-spot compared to the same on the surface of Au NRs.

2.2. Experimental Section

2.2.1. Materials

Hydrogen tetrachloroaurate(III) trihydrate ($HAuCl_4.3H_2O$), sodium borohydride ($NaBH_4$), cetyltrimethylammonium bromide (CTAB), silver nitrite ($AgNO_3$) and 4-Aminothiophenol (4-ATP) were purchased from Sigma Aldrich. Ascorbic acid was purchased from Sisco Research Laboratories Pvt. Ltd.(SRL) All the reagents were used as received. Milli-Q grade water was used in all the experiments.

2.2.2. Synthesis of CTAB stabilized gold nanorods (Au NRs)

Gold nanorod was synthesized by the well-known seeded growth method. [17,18]

Preparation of seed:

TH-2949_166122105

15 mL of 0.1 M CTAB solution was taken into a 100 mL conical flask. Then slowly 1 mL of 0.005 M $HAuCl_4$ solution was added into the conical flask with gentle shaking. In 30 s, 2 mL of 0.01 M chilled $NaBH_4$ solution was added at a once into the flask. Then immediate shaking was performed for 2 min and it was kept for 1.5 h.

Preparation of growth solution:

15 mL of 0.1 M CTAB solution was taken into a 100 mL conical flask. Then 1 mL of 0.005 M $HAuCl_4$ solution was slowly added into the flask with gentle shaking. In 30 s, 0.2 mL of 0.01 M $AgNO_3$ solution was gently added into it. After that within 20 s, 0.8 mL of 0.01 M ascorbic acid was gently added into the reaction mixture. Finally, in 20 s, 20 µL seed solution was added, which was followed by gentle shaking for 10 s and then the mixture was kept for 15 h. The as prepared growth dispersion was centrifuged at 15000 rpm for 10 min at 10°C, which was followed by redispersion of the pellet in the same volume of deionized water.

2.2.3. End to End assembly of 4-Aminothiophenol (4-ATP) treated Au NRs:

3 mL of as-synthesized gold Au NR dispersion was taken in a vial. To the above dispersion, 50 µL (10 µM) of freshly prepared aqueous solution of 4-ATP was added at room temperature while stirring. Prior to making the 10 µM aqueous solution, 4-ATP was dissolved in trace amount of methanol due to its limited solubility in water. The mixture was allowed to stir for 15 h. This was then followed by centrifugation at 12 000 rpm for 10 min at 10°C, which was followed by redispersion of the pellet in 1 mL deionized water.

2.2.4. Photocatalytic conversion of 4-Aminothiophenol to trans-dimercaptoazobenzene at the hot-spot of assembled Au NRs:

The Au NRs assembly dispersion obtained after centrifugation was drop cast (50 µL) on a pre-cleaned glass slide and was allowed to air dry. The time - dependent SERS spectra were then recorded after every 2 min of laser irradiation (at 632.8 nm) on a defined laser spot area of the sample. (laser: 632.8 nm, Objective: 20x, acquisition time: 5 s) The normalized plot of area under the curve at 1430 cm^{-1} was plotted with respect to different time interval after laser irradiation. All spectra were normalized with respect to peak at 1078 cm^{-1}. Similarly, kinetic measurements were carried out in several different spots of the sample for experiment carried out each time. We herein present kinetic data acquired from measurement carried out in three different spot areas of a sample.

TH-2949_166122105

2.2.5. Control experiment

Two control experiments were performed.

(A) 250 mM 4-ATP solution in water was drop-cast on glass slide and dried overnight. The sample was then irradiated with 632.8 nm laser and normal Raman spectra were recorded after every 2 min laser irradiation. (laser source: 632.8 nm, 20x, acqusition time: 5 s)

(B) In another control experiment, 4-ATP attached to the end to end assembled Au NR dispersion was drop-cast on glass slide. Then solid drop-cast sample was divided in to two regions. The reaction was followed by recording Raman spectrum with 632.8 nm laser after every 2 min of irradiation with 532 nm. Similarly, in the other region the same procedure was followed but the irradiation was done with 632.8 nm laser instead of 532 nm laser. The overall results of the study suggested that the conversion of 4-ATP into DMAB on Au NRs was catalytically more feasible with 632.8 nm than 532 nm laser radiation.

2.2.6. Decomposition reaction of DMAB formed at the hot-spot of assembled Au NRs following treatment with H_2O_2

The decomposition reaction was performed by treating the photocatalytic product DMAB with 10 uL of H_2O_2. Briefly, the laser spot region on the glass surface, where the oxidative coupling of 4-ATP to DMAB was carried out, was carefully injected with 10 uL H_2O_2 (of concentration 8 M and, (or) 10 M) and covered with coverslip. After an incubation time of 1 min, time - dependent SERS spectra were recorded on the same spot with 632.8 nm laser (with an acquisition time of 5 s) after an interval of 2 min.

2.3. Results and Discussions

Au NRs of aspect ratio 3.5±0.4 (52.5±4.0×14.8±1.4 nm) were synthesized following seed mediated growth method. [17,18] (Refer experimental Section 2.2) **Figure 2.1A** shows the transmission electron microscopic (TEM) image recorded for the as-synthesized Au NRs that showed surface plasmon band maxima at 516 nm and 762 nm (**Figure 2.1B**), corresponding to transverse and longitudinal plasmon modes, respectively. **Figure A2.1** (**Appendix**) shows additional TEM image of the as-synthesized CTAB - Au NR at different

TH-2949_166122105

magnifications along with histogram plot showing the aspect ratio distribution of 345 particles as obtained from different random batches of synthesis (**Figure A2.1(C)**). The as-synthesized rods were then treated with 10 µM aqueous solution of 4-ATP (containing trace amount of methanol) at room temperature and left to stir for 15 h. (Refer experimental section 2.2.3) The final reaction mixture was then centrifuged at 12000 rpm for 10 min at 10 °C. It is to be mentioned that selective binding of the thiolated ligand specifically to the end of the NRs over the side could be achieved by tuning the concentration of 4-ATP in the reaction mixture.[15] On the other hand, it has been reported that excess addition leads to the adsorption of 4-ATP on the end as well as side facets of Au NRs.[15] Therefore, treatment of as synthesized Au NRs with 10 µM 4-ATP solution led to the chemisorption of the 4-ATP preferentially onto the end of the NRs via the sulphydryl group leaving the amine group free. This was indirectly concluded from the transmission electron microscopy (TEM) study shown in **Figure 2.1(C-F)**, which indicated linear assembly formation. Additional TEM images supporting the end-to-end assembly formation can be found in **Figure A2.2, Appendix.**

The centrifugation of the reaction mixture at 12000 rpm led to the end to end linear assembly between the Au NRs. The selective attachment of 4-ATP at the end of individual Au NRs over the side of the Au NR allowed facile intermolecular H-bonded interaction between the 4-ATP molecules attached to each end of the adjacent Au NR. The H-bonding took place via the amine group following centrifugation, leading to the generation of the linear assembly of Au NRs.

TH-2949_166122105

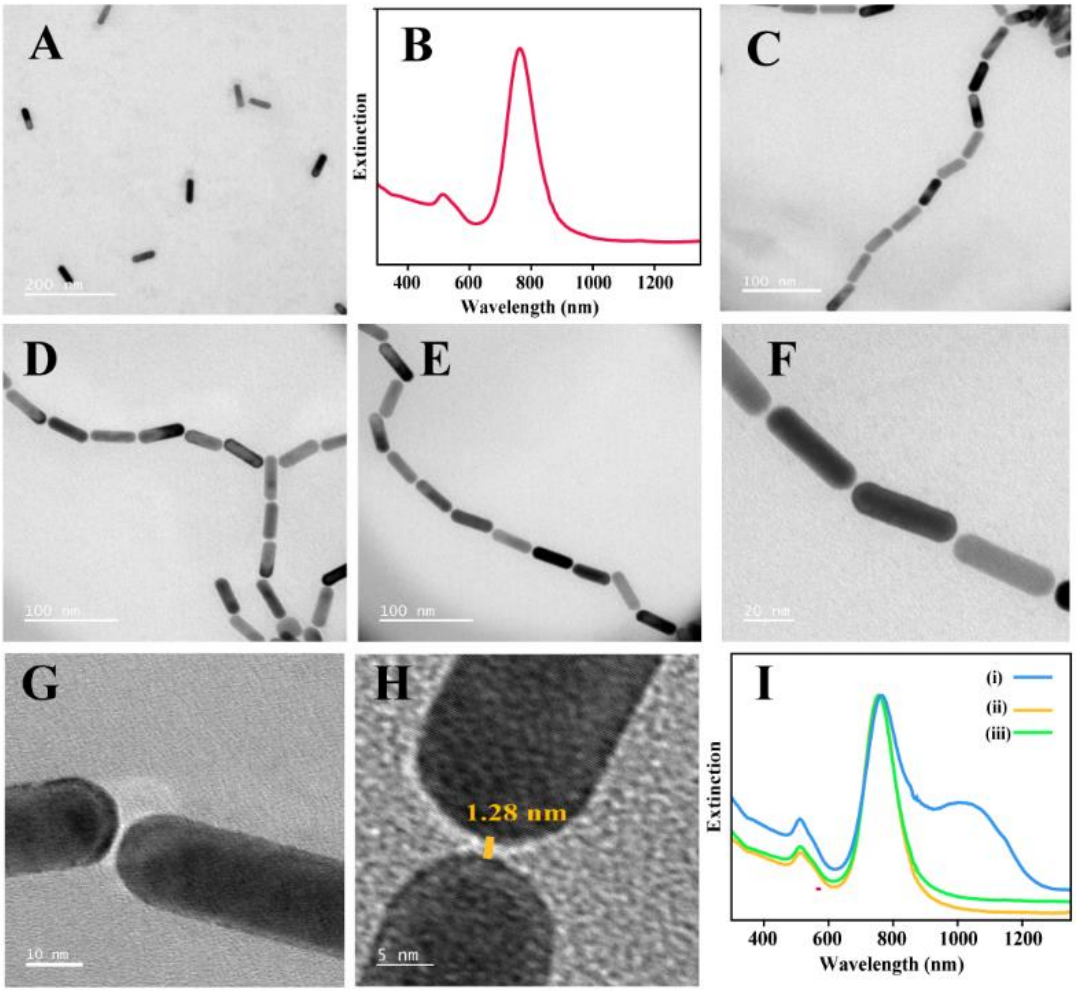

Figure 2.1. (**A**) TEM image and (**B**) UV-vis spectrum of as synthesized CTAB stabilized Au NR. (**C-F**) TEM images of as synthesized Au NR treated with 4-ATP and following centrifugation at 12000 rpm for 10 min at 10 °C. HRTEM image of 4-ATP treated Au NR showing (**G**) end to end assembly and (**H**) a typical gap-distance of 1.28 nm between the assembled NRs. (**I**) Normalized UV-vis spectra of (**i**) 4-ATP treated Au NRs and (**ii**) as synthesized Au NRs (with both being recorded) following centrifugation at 12000 rpm for 10 min at 10 °C and (**iii**) 4-ATP treated Au NRs before centrifugation.

A schematic depiction of the generation of assembled Au NRs using 4-ATP for carrying out catalytic conversion of 4-ATP to DMAB is shown in **Scheme 2.1**.

TH-2949_166122105

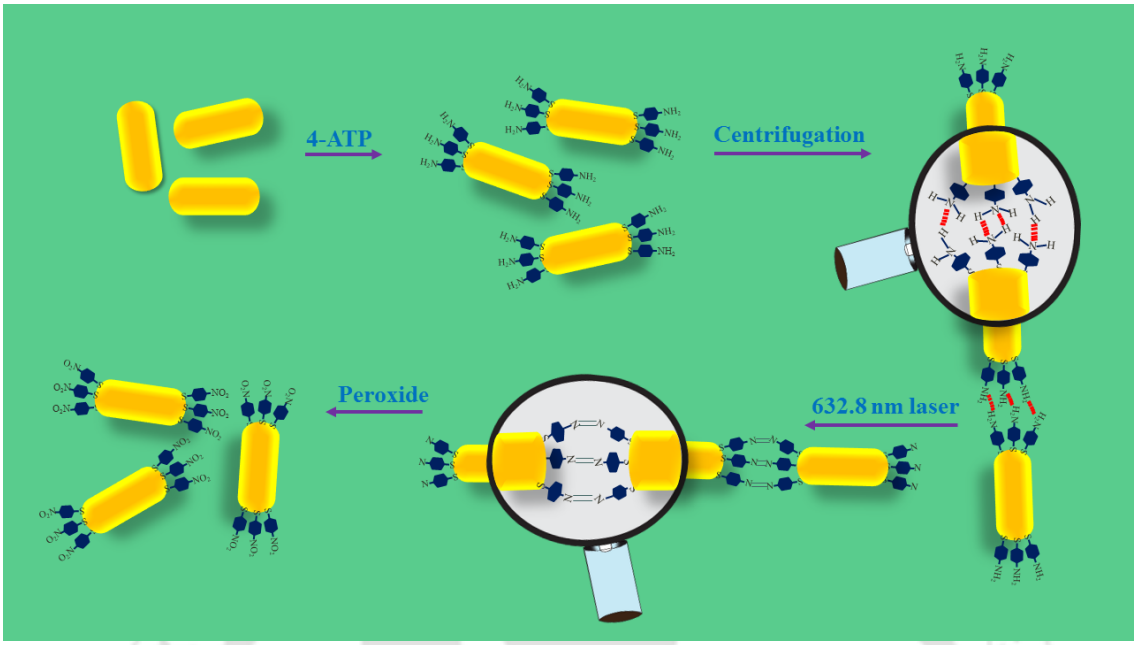

Scheme 2.1. Cartoon depiction of the formation of assembled Au NR via centrifugal action followed by photochemical conversion of 4-ATP into DMAB and degradation of DMAB in the presence of hydrogen peroxide (H_2O_2) at the plasmonic hot-spot.

Figure 2.1G shows the high resolution transmission electron microscopy (HRTEM) image of end to end assembled Au NRs with a typical gap-distance of ~1.28 nm between the adjacent assembled Au NRs at the hot-spot (**Figure 2.1H**). The absorption spectrum recorded for assembled Au NRs following centrifugation (and redispersion) showed an appearance of a new broad band at 1018 nm with red-shift of the primary longitudinal absorption band from 756 nm to 765 nm. (**Figure 2.1I(i)**, blue line) Additionally, the appearance of broad band at 1018 nm was also accompanied by corresponding decrease in the extinction of longitudinal band; however, the corresponding extinction spectrum shown in **Figure 2.1I** are normalized for the ease of comparison and further discussion. The appearance of the new band at 1018 nm could be attributed to the longitudinally coupled plasmon absorption originating from linear assembly of Au NR n-mers in the dispersion after centrifugation. [16,19]

On the other hand, no signature of assembly formation was observed in the dispersion of as synthesized Au NRs after centrifugation at 12000 rpm as was reflected from their

TH-2949_166122105

corresponding UV-Vis spectrum (**Figure 2.1I(ii)** and TEM (**Figure A2.3A**). Also, UV-vis spectrum (**Figure 2.1I(iii)** and TEM image (**Figure A2.3B**) recorded for Au NRs treated with 4-ATP (before centrifugation) showed no significant shift in SPR band and thus formation of assembly. Additionally, when centrifuged at a lower speed of 5000 rpm for 10 min at 10 ˚C, the as-synthesized Au NRs (**Figure A2.4A(i)**) did not undergo end-to end assembly formation via 4-ATP. This was reflected in the UV-Vis spectra shown in **Figure A2.4A(ii)**, which did not exhibit any significant change in the spectrum of the as-synthesized Au NRs. TEM images recorded for the same dispersion also reflected no indication of linear assembly. (**Figure A2.4B**) The results clearly indicated that the Au NR n-mer assembly formation was induced during the centrifugation. It is to be mentioned here that the different physical forces of interaction that play important roles in determining the dispersion of nanoscale particles in colloidal medium have been documented. [20] In the present context, the TEM images recorded for 4-ATP functionalized Au NRs (**Figure A2.3B**) revealed that the NRs were dispersed well in the medium. On the other hand, the centrifugal action – resulting in precipitation from the medium - acted as the driving force to induce H-bonding amongst the 4-ATP functionalized Au NRs, which led to assembly formation. Plausibly, the net centrifugal force, acting on the colloidal particles during precipitation (through centrifugation), is strong enough to overcome the electrostatic repulsion between the Au NRs that could arise from the electrical double layers in aqueous phase or from the remaining long chain CTAB moiety (positively charged) at the longitudinal end that could not be replaced completely by 4-ATP molecule in the medium. [21] Further, that the 4-ATP is less soluble in water might have helped the 4-ATP stabilized NRs to easily precipitate out of the dispersion - via H-bonding of the molecules - through centrifugation at 12000 rpm speed. Additionally, it is known that different centrifugal speeds exhibit different driving force towards the packing structure or sedimentation of the concentration gradient formed for a particular species.[22] This could be the one of the plausible reason towards the formation of assembled Au NRs structures when subjected to centrifugation at 12000 rpm over 5000 rpm. Further to validate the assembly formation of Au NRs via H-bonded interaction between the 4-ATP, the inter-particle distance between two Au NRs (determined from TEM measurement) was matched with the sum of the length of two 4-ATP molecule including the H-bond length determined using Avogadro. **Figure A2.5** shows the length of 4-ATP dimer

TH-2949_166122105

sharing one or two H-bond/s being calculated using Avogadro. The average inter-particle distance of 1.28 nm obtained from TEM measurement was found to be in close agreement with the length of 4-ATP dimer formed sharing one H-bond calculated using Avogadro (~ 1.26 nm). Thus the end-to-end assembly of Au NRs connected by H-bonded 4-ATP molecules opened up a facile approach to study dimerization reaction at the plasmonic hot spot.

The assembled Au NRs were further investigated for their potential as SERS substrate to monitor photochemical reaction at the hot-spot. The dispersion of Au NR assembly was dried on a pre-cleaned glass slide overnight prior to initiating the reaction. (Refer experimental section 2.2.4 for details) When light of 632 nm laser source was shone on the assembled Au NRs, the 4-ATP dimer at the hot-spot of assembled Au NRs underwent chemical conversion to DMAB. The success of the reaction was characterized by clear disappearance of Raman peak at 1493 cm^{-1} due to amine stretching (ν_{NH}) vibration of 4-ATP and subsequent appearance of peaks at 1389 cm^{-1} ($\nu_{NN} + \nu_{CC} + \nu_{CN}$) and 1432 cm^{-1} ($\nu_{NN} + \nu_{CC} + \nu_{CH}$) due to ring stretching vibration associated with ─N═N─ moiety of DMAB.[4,7] (**Figure 2.2A** and **B**) Additionally, the appearance of C–N symmetric stretching vibration bands at 1142 cm^{-1} indicated the trans-geometry of the final coupling product (DMAB).[23] On the other hand, no such product formation from 4-ATP treated with Au NRs was observed in dark condition, indicating photoinduced nature of the reaction.[8] It is also supported by the SERS spectrum (**Figure 2.2 A** and **B**) obtained for sample that was dried overnight and which showed no signature of product (DMAB) formation at the initial time (0 min) of the time-dependent study. Raman spectra of CTAB stabilized Au NRs and glass only are shown in **Figure A2.6A** and **B**, respectively, as references.

TH-2949_166122105

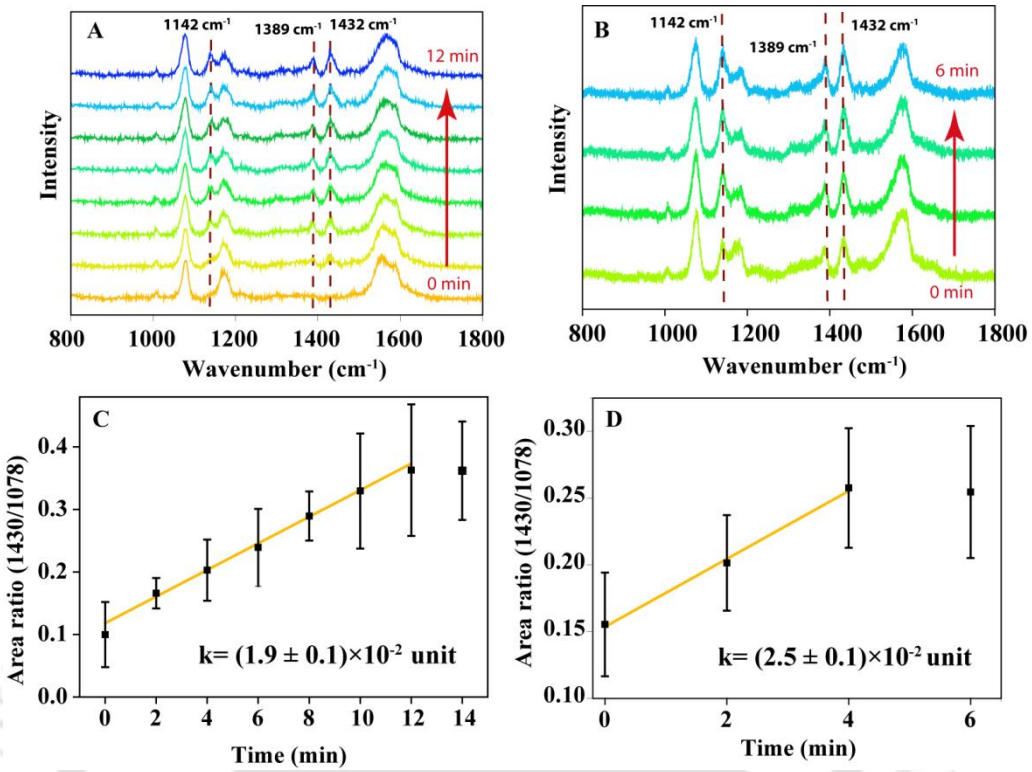

Figure 2.2. Time dependent change in SERS spectra recorded for assembled Au NR treated with 4-ATP upon irradiation at two different laser powers of (**A**) 0.3 mW and (**B**) 1.5 mW. (**C**) and (**D**) represent the corresponding normalized plot of area under the curve at 1430 cm^{-1} obtained with respect to different times of laser exposure. Data points so obtained were fitted to linear graph and rate constant values for zero order kinetics were extracted from the slope of the plot of normalized intensity versus time. For rate constant calculation, the final data values shown in (**B**) and (**D**) are neglected. They are, however, included in the respective plot to indicate the completion of reaction.

We have further recorded the time dependent normal Raman spectra for 250 mM solution of 4-ATP dried on glass slide as shown in **Figure A2.7A** and **B** that revealed no signature of chemical conversion to DMAB when shone with 532 nm or 632.8 nm laser, independently, over time under atmospheric conditions. (Refer experimental section 2.2.5 for details) The importance of oxygen in the light induced plasmon catalyzed azo-coupling of 4-ATP to DMAB has been reported in the literature.[7,8] Additionally, the roles of surface bound oxide agent and hot electrons generated by SPR excitation have also been

TH-2949_166122105

demonstrated.[8,10] In the current scenario, the reaction took place in atmospheric condition, which could well be the source of oxygen and plausibly hot holes generated by SPR excitation could easily capture electron from the HOMO of adsorbed molecule (4-ATP). Meanwhile hot electrons being quenched by atmospheric O_2 or adsorbed O_2 subsequently led to the photooxidation of aromatic amine group.[7, 24] Thus the conversion of 4-ATP to DMAB took place at the hot spot of linearly assembled Au NRs in the presence of 632.8 nm laser light.

To further understand the kinetics of photoinduced conversion reaction of dimerized 4-ATP (via H-bonding) at the hot-spot of the assembled Au NRs to DMAB, time dependent reaction kinetics was monitored for the same at two different powers (0.3 and 1.5 mW) using laser excitation at 632.8 nm. The kinetics was monitored following disappearance of Raman peak at 1493 cm^{-1} due to amine stretching (ν_{NH}) of 4-ATP and time dependent rise of peak at 1389 cm^{-1} ($\nu_{NN} + \nu_{CC} + \nu_{CN}$) and 1432 cm^{-1} ($\nu_{NN} + \nu_{CC} + \nu_{CH}$) due to ring stretching vibration associated with ─N═N─ moiety.[4,7] The SERS spectra at different time intervals were recorded (with 5 s acquisition time) after each irradiation period of 2 min with 632.8 nm laser. The kinetic study at different laser powers were carried out for different reaction times till the completion of product formation, which was ensured from the lack of further increment in the Raman peak intensity due to the product. **Figure 2.2A** and **B** shows the time - dependent SERS spectra recorded for the coupling reaction at the hot-spot of the assembled Au NRs. The normalized area under 1430 cm^{-1} was considered for monitoring the reaction kinetics in all the cases. As is clear from the figures, the intensities of the peaks and areas under the curves increased monotonically with time. Considering the fact that the reaction took place following H-bond formation between the two 4-ATP molecules positioned in between the nanorods in the linear assembly, the reaction rate could be considered to be independent of the concentration of the reactant (4-ATP). Thus the plasmon assisted photocatalytic de-hydrogenation of 4-ATP may be considered to follow zero order kinetics. The rate constant values for the zero order reaction kinetics was deduced from slope of the linear fit of the normalized area under 1430 cm^{-1} versus time plot. The rate constant value deduced for the sample illuminated at 0.3 mW was found to be $(1.9\pm0.13)\times10^{-2}$ unit (**Figure 2.2C**); whereas when the laser power was increased to 1.5 mW, the coupling reaction showed a higher rate constant value of $(2.5\pm0.16)\times10^{-2}$ unit (**Figure 2.2D**). The

TH-2949_166122105

increase in rate constant value with the laser power could be due to the increased hot-electron generation at the hot-spot that accelerated the coupling reaction rate.[10] However, it is to be noted that the kinetic experiment carried out at a third laser power of 0.75 mW did not show a marked difference in rate constant value for consideration. That is to say, rate constant value deduced in case of kinetics monitored at 0.75 mW was found to be $(2.3\pm0.2)\times10^{-2}$ unit (**Figure A2.8, Appendix)** which was within the error range of the rate constant value obtained from the kinetics carried out at 1.5 mW. Hence, we preferred to consider specifically two different powers viz, 0.3mW and 1.5 mW in the present case to delineate the laser power dependency.

On the other hand, SERS spectrum recorded for the same sample with 632.8 nm laser (1.5 mW) after irradiation for 2 min with 532 nm laser, did not show significant rise of peak at 1390 cm^{-1} and 1430 cm^{-1} (**Figure A2.7C**), indicating the poor feasibility of the reaction. It is plausible that the near resonance condition achieved with 632.8 nm laser light with the longitudinal LSPR of Au NRs – having the peak at 765 nm, provided sufficiently enhanced plasmon field to facilitate the coupling reaction of H-bonded 4-ATP dimer molecule at the hot-spot of end-to-end assembly. On the other hand, 532 nm laser wavelength, being away from the coupled plasmon resonance peak, could not efficiently catalyze the photoreaction of 4-ATP on the assembled Au NRs at the hot-spot or otherwise. Thus the de-hydrogenation reaction of 4-ATP dimers to DMAB at the hot-spot of the assembled Au NRs showed a laser wavelength dependent reactivity. Additionally, we would like to state that although selection of excitation laser close to the peak at 1018 nm (plasmon extinction maximum of the Au NR assembly) would have resulted better signal to noise ratio; however, the quality of spectra with excitation at 632.8 nm was deemed sufficient to pursue the same objective. As already explained above, centrifugation of the 4-ATP treated reaction mixture of Au NR at 5000 rpm, did not show any assembly formation. (**Figure A2.4**) Further, we compared the reaction kinetic rate of plasmon induced photoreaction of 4-ATP on Au NRs obtained after centrifugation at 5000 rpm and 12000 rpm, respectively. The results (**Figure 2.3**) suggested that the reaction was indeed made possible by the enhanced plasmons at the hot spots of the linear assembly. Interestingly, it was found that the rate of azo-coupling reaction on the Au NR assembly (obtained after centrifugation at 12000 rpm) was faster than the same coupling reaction that took place at the end of non-assembled Au NR surface for the sample obtained

TH-2949_166122105

after centrifugation at 5000 rpm. This was clearly reflected from the rate constant value of 1.1×10^{-2} unit obtained for Au NR sample centrifuged at 5000 rpm, whereas kinetic constant obtained for linearly assembled Au NR was calculated to be 1.8×10^{-2} unit shown in **Figure 2.3**. The reaction kinetics was monitored at the excitation wavelength of 632.8 nm (5 s acquisition time at 0.3 mW) after successive irradiation time of 2 min with the same laser source.

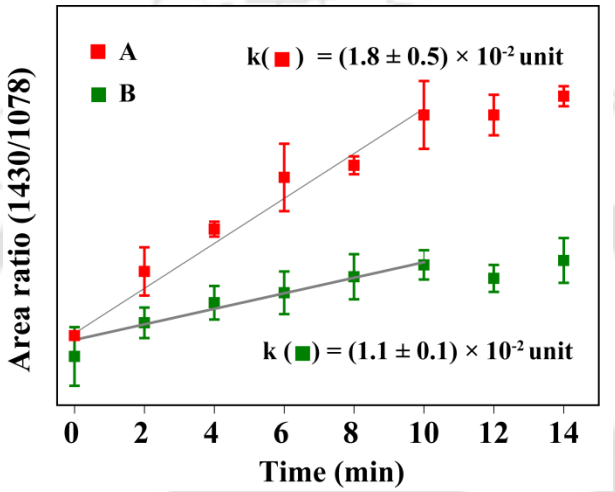

Figure 2.3. Plot of normalized area under peak at 1430 cm^{-1} at different time period of laser (632.8 nm) exposure of 4-ATP treated Au NRs following centrifugation at (**A**) 12 000 rpm and (**B**) 5000 rpm for 10 min at 10 °C. Spectra are normalized with respect to area under the peak at 1078 cm^{-1}. Slope of the linear fit was used to calculate the kinetic constant values. Data points show the average result of measurements carried out in triplicate.

We were further interested in pursuing reaction involving the product DMAB formed at the hot spot of the assembled Au NRs. For this, the samples were irradiated with 632.8 nm laser light for 6 min and the product formation was confirmed through SERS study as mentioned above following which the sample was treated with hydrogen peroxide (H_2O_2). (Refer experimental section 2.2.6 for details) The SERS results clearly indicated the oxidation of the azo group of DMAB and formation of a new species due to appearance of peak at 1330 cm^{-1} due to N─O stretching vibration. **Figure 2.4A** and **B** show the time dependent SERS spectra recorded following treatment with H_2O_2.

TH-2949_166122105

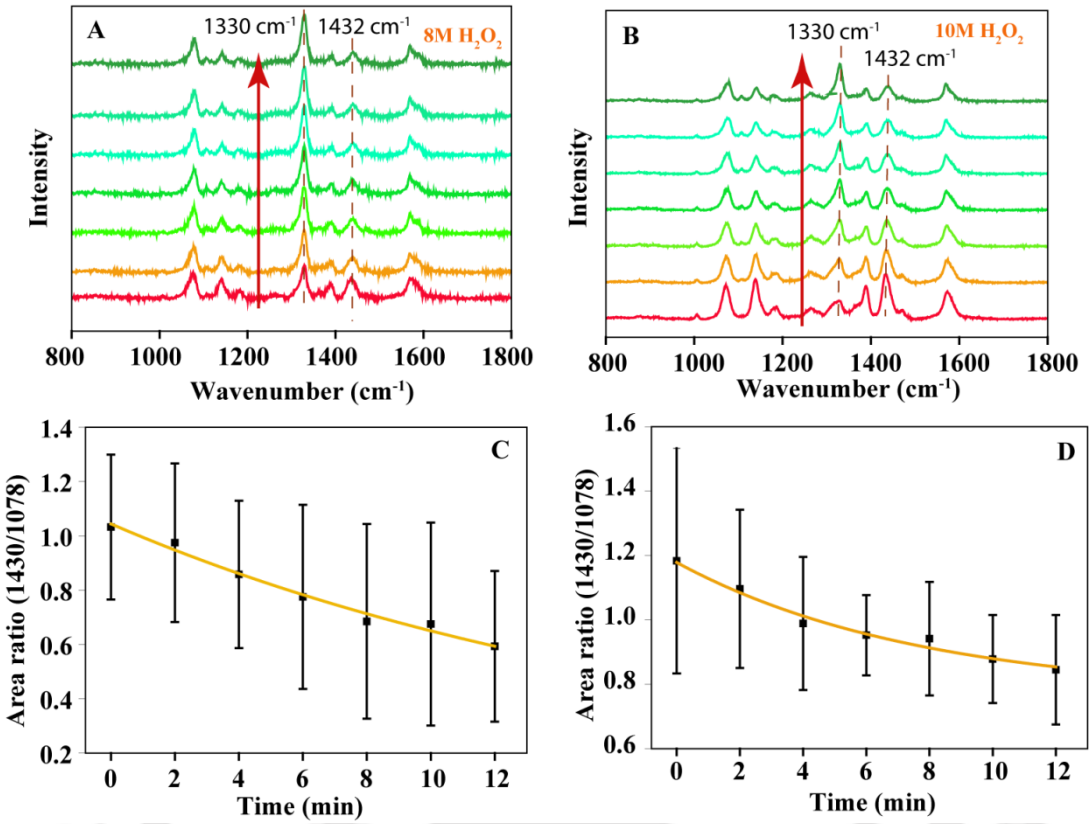

Figure 2.4. Time dependent change in SERS spectra recorded upon H_2O_2 treatment at two different concentrations - (**A**) 8M (23%) and (**B**) 10M (28%) on photoirradiated Au NR (treated with 4-ATP) assembly. (632.8 nm laser, 5 s acquisition time) (**C**) and (**D**) represent the plots of corresponding changes in normalized area under the curve at 1430 cm^{-1} at different time intervals following H_2O_2 treatment.

The SERS spectra were recorded with 632.8 nm laser (0.3 mW) with an acquisition time of 5 s after an interval of 2 min. Interestingly, a clear decrease in peak intensity at 1432 cm^{-1} and 1142 cm^{-1} with time was observed in conjunction with the appearance of a new peak at 1330 cm^{-1}. According to the literature report, sonochemical treatment of azo bond in the presence of hydroxyl radical leads to the formation of nitroso or nitro group. [25] Thus the time-dependent rise of the peak at 1330 cm^{-1} in SERS spectra shown in **Figure 2.4A** and **B** upon treatment with H_2O_2 could be assigned to the formation of nitro compound during the course of reaction.[5] We assign the band at 1330 cm^{-1} due to N─O stretching vibration indicating the oxidation of DMAB. The oxidative reaction kinetics of DMAB was monitored at two different concentrations of H_2O_2 viz, 8 M (23%) and 10 M (28%). Importantly, the

TH-2949_166122105

rate of oxidative reaction at the hot-spot of the linearly assembled Au NRs in the presence of 10 M (28%) H_2O_2 was found to be 1.7 fold higher than that observed in the presence of 8 M (23%) (**Figure 2.4 C** and **D**). Considering first order dependency, the rate was calculated from the slope (exponential fit) of the plot of normalized area under the curve at 1430 cm^{-1} at different times of laser irradiation. Although the exact mechanisms of the reactions are to be established, the results clearly indicated the feasibility of a secondary reaction out of the product of primary reaction i.e., formation of DMAB from 4-ATP at the plasmonic hot spot of a linearly assembled Au NRs and then oxidation of the azo group in the presence of H_2O_2.

2.4. Conclusions

In brief, the selective binding of 4-ATP to the end of Au NRs - which is a concentration dependent process - led to the linear assembly of Au NRs with 4-ATP dimer positioned at the hot-spot. The Au NR assembly was formed via H-bonded interaction between the 4-ATP molecules bound to the ends of Au NRs driven by the centrifugal force. Further, the hydrogen elimination reaction of 4-ATP was possibly mediated by hot-hole generation[7] at the hot-spot of the assembled Au NRs upon laser illumination of 632.8 nm. Time-dependent SERS measurements indicated the transformation of 4-ATP dimers at the hotspot of the assembled Au NRs to DMAB. Interestingly, the rate of plasmon induced coupling reaction at the hot-spot was found to be faster than that observed on the surface at the longitudinal end of non-assembled Au NRs. This was reflected from the rate constant value calculated for the proposed zero order kinetics that was found to be ~ 1.6 fold higher in case of reaction at the hot-spot when compared with the reaction at longitudinal end of non-assembled Au NRs. Further, addition of H_2O_2 to the DMAB generated as product from amine group of 4-ATP at the hot-spot via photochemical reaction - yielded the nitro product. The present study highlighted the utility of hierarchical metallic nanostructures or nano-assembly of Au NRs as SERS substrate for carrying out incident wavelength selective plasmon induced catalytic reaction at the hot spot, which could further be used for carrying out secondary catalytic reaction. The hot-spot generated due to Au NR assembly served as better and active catalytic center when compared to the surface of Au NRs. This, therefore, presents a newer platform that could be further exploited for carrying out plasmon induced complex chemical reaction by rational selection of excitation laser wavelength and hierarchical plasmonic substrate.

TH-2949_166122105

2.5. References

1. Ren, X., Cao, E.; Lin, W.; Song, Y.; Liangc, W.; Wang, J. *RSC Adv.* **2017**, *7*, 31189-31203.

2. Zhang, Y.; He, S.; Guo, W.; Hu, Y.; Huang, J.; Mulcahy, J.R.; Wei, W.D. *Chem. Rev.* **2018**, *118*, 2927-2954.

3. Zhang, Z.; Lacroix, M. R.; Deckert, V. *Faraday Discuss* **2017**, *205*, 213-226.

4. Zhang, Z.; Kinzel, D.; Deckert, V. *J. Phys. Chem. C* **2016**, *120*, 20978-20983.

5. Yan, X.; Wang, L.; Tan, X.; Tian, B.; Zhang, J. *Scientific Reports*, **2016**, *6*, 30193.

6. Sun, M.; Xu, H. *Small* **2012**, *8*, 2777-2786.

7. Wang, J.; Ando, R. A.; Camargo, P. H. C. *Angew. Chem.* **2015**, *54*, 6909-6912.

8. Zhang, Z.; Merk, V.; Hermanns, A.; Unger, E. S. W.; Kneipp, J. *ACS Catal.* **2017**, *7*, 7803-7809.

9. Dutta, A.; Chattopadhyay, A. *J. Phys. Chem. C* **2017**, *121*, 18854-18861.

10. Zhang, Z.; Gaudig, T.D.; Singha, P.; Deckert, V. *Chem. Commun.* **2015**, *51*, 3069-3072.

11. Liu, X. L., Liang, S., Nan, F., Yang, Z. J., Yu, X. F., Zhou, L., Hao, Z. H.; Wang, Q. Q. *Nanoscale* **2013**, *5*, 5368.

12. Wang, L., Zhu, Y., Xu, L., Chen, W., Kuang, H., Liu, L., Agarwal, A., Xu, C., Kotov, N. A. *Angew. Chem.* **2010**, *49*, 5472-5475.

13. Leung, F. C., Leung, S. Y. L., Chung, C. Y. S., Yam, V. W. W. *J. Am. Chem. Soc.* **2016**, *138*, 2989-2992.

14. Liu, K., Ahmed, A. Chung, S., Sugikawa, K., Wu, G., Nie, Z., Gordon, R., Kumacheva, E. *ACS Nano* **2013**, *7*, 5901-5910.

15. Tan, S. F.; Anand, U.; Mirsaidov, U. *ACS Nano* **2017**, *11*, 1633-1640.

TH-2949_166122105

16. Thomas, K. G.; Barazzouk, S.; Ipe, B. I.; Joseph, S. T. S.; Kamat, P. V. *J. Phys. Chem. B* **2004**, *108*, 13066-13068.

17. Sau, T. K.; Murphy, C. J. *Langmuir* **2004**, *20*, 6414-6420.

18. Nikoobakht, B.; Sayed, M. A. E. *Chem. Mater* **2003**, *15*, 1957-1962.

19. Abtahi, S. M. H.; Burrows, N. D.; Idesis, F. A.; Murphy, C. J.; Saleh, S. B.; Vikesland, P. J. *Langmuir* **2017**, *33*, 1486-1495.

20. Liang, Y.; Hilal, N.; Langston, P.; Starov, V. *Advances in Colloid and Interface Science* **2007**, *134–135*, 151–166.

21. Fan, W.; Chen, M.; Yang, S.; Wu, L. *Scientific Reports* **2015**, *5*, 12100.

22. Chen, M.; Colfen, H.; Polarzb, S. *Z. Naturforsch* **2013**, *68b*, 103-110.

23. Lang, X. F.; Yin, P. G.; Tan, E. Z.; You, T. T.; Guo, L. *J. Raman Spectrosc*. **2013**, *44*, 425-432.

24. Zhao, L. B.; Huang, Y. F.; Liu, X. M.; Anema, J. R.; Wu, D. Y.; Ren, B.; Tian, Z. Q. *Phys. Chem. Chem. Phys*. **2012**, *14*, 12919-12929.

25. Joseph, Z. M.; Destaillats, H.; Hung, H. M.; Hoffmann, M. R. *J. Phys. Chem. A* **2000**, *104*, 301-307.

TH-2949_166122105

Appendix of Chapter 2: A2

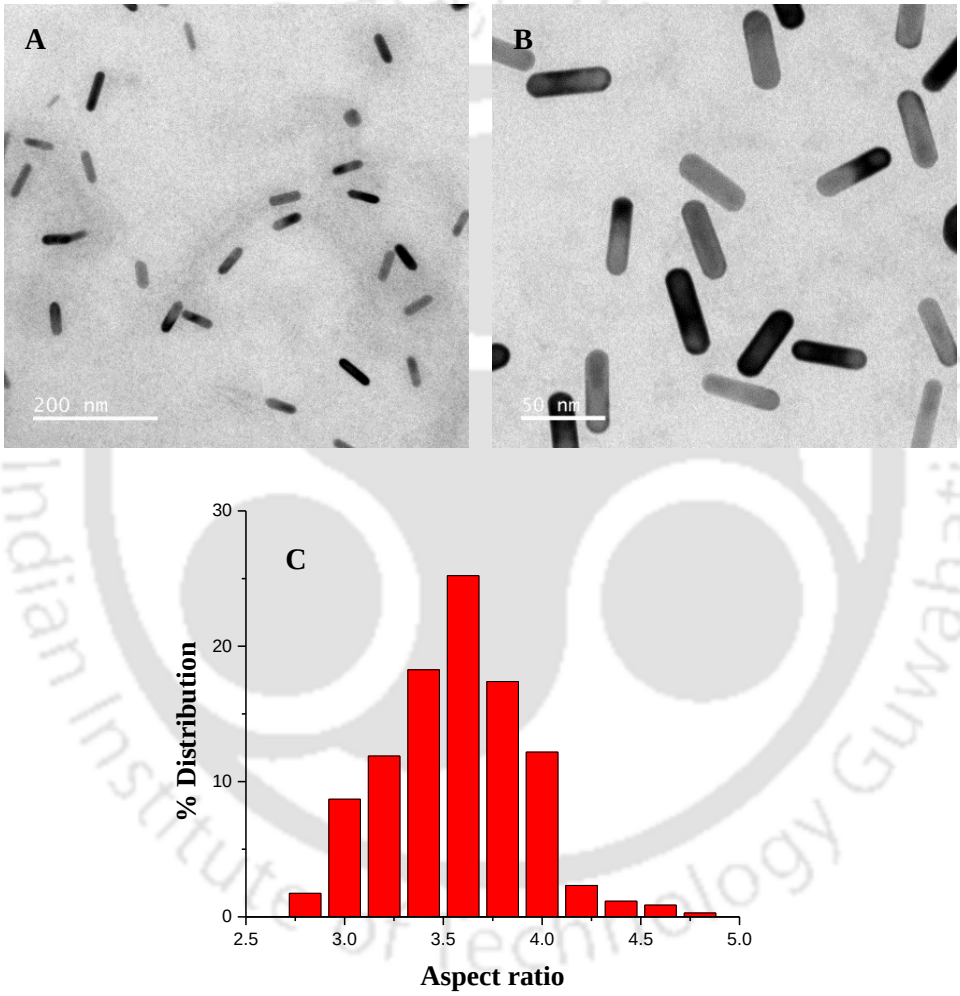

Figure A2.1. TEM images of as synthesized CTAB stabilized Au NRs (**A**) at low magnification; (**B**) at high magnification and (**C**) histogram plot showing aspect ratio distribution considering random 345 Au NRs.

TH-2949_166122105

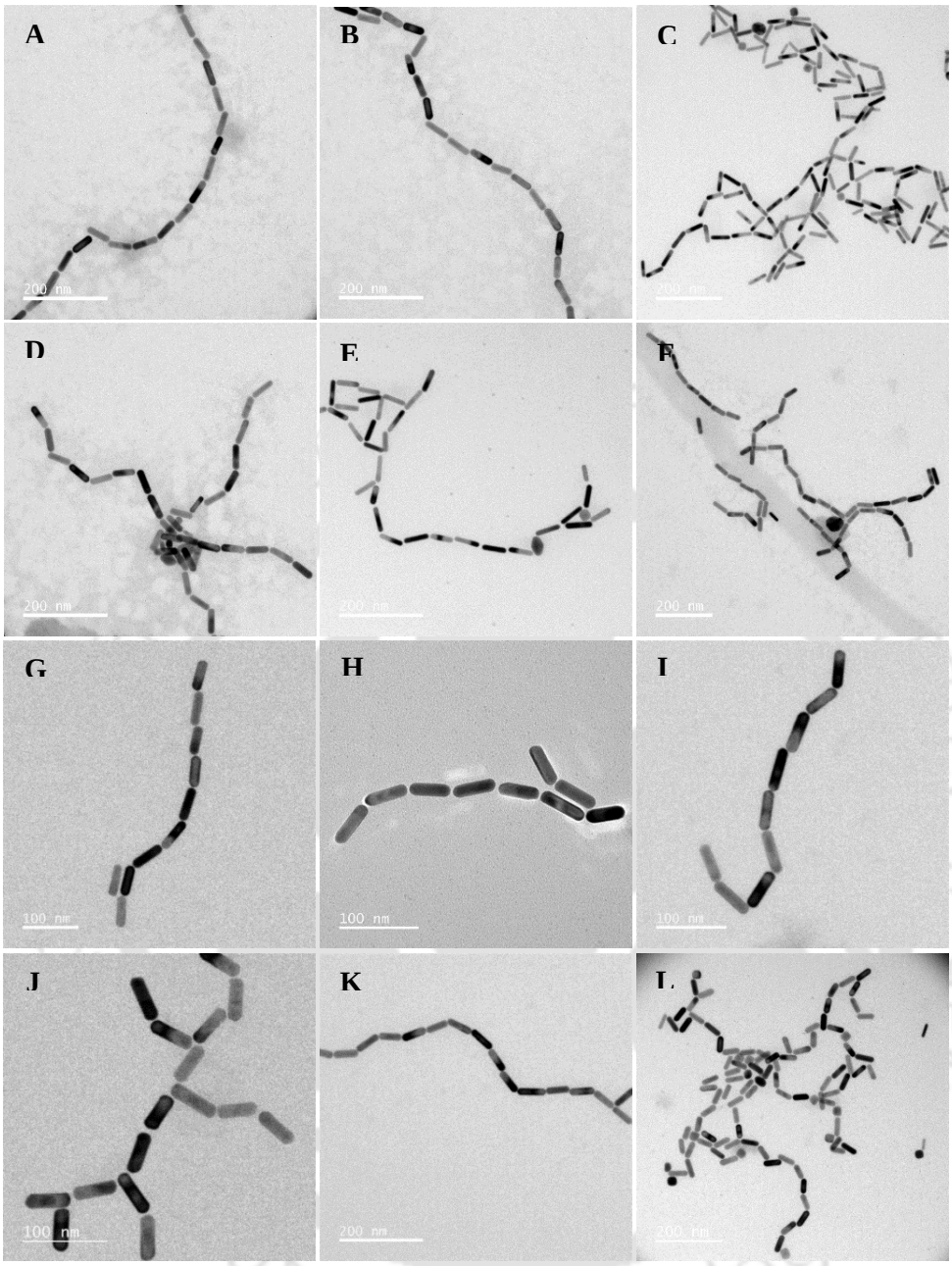

Figure A2.2. TEM images of 4-ATP treated Au NRs at different magnifications showing end-to-end assembly.

TH-2949_166122105

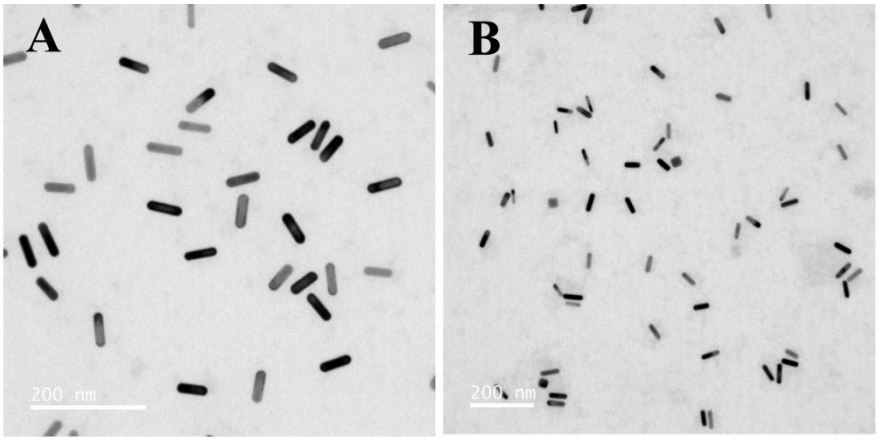

Figure A2.3. TEM images of as synthesized Au NRs (**A**) after centrifugation at 12000 rpm; those of Au NRs treated with 4-ATP (**B**) before centrifugation.

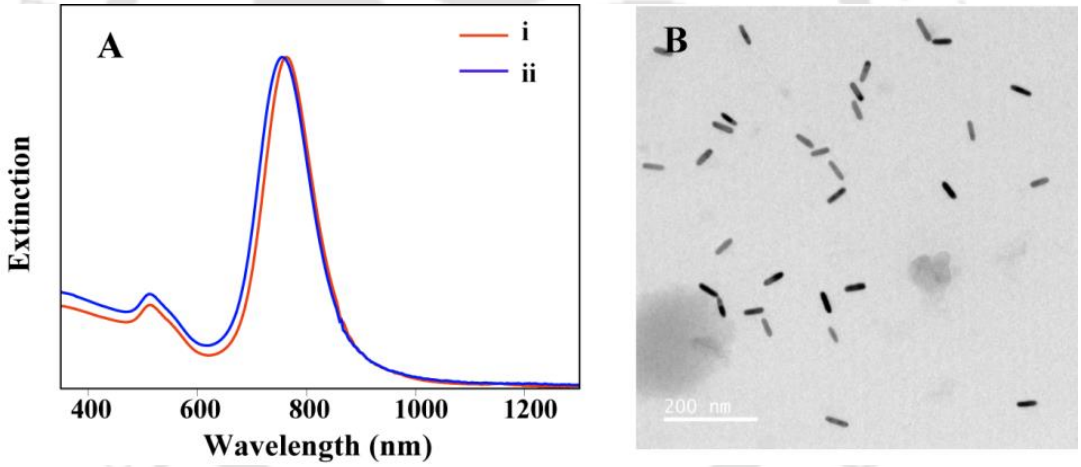

Figure A2.4. (**A**) UV-Vis spectra of (i) 4-ATP treated Au NRs and (ii) of that after centrifugation at 5000 rpm for 10 min (10 °C). (**B**) TEM image of 4-ATP treated Au NRs after centrifugation at 5000 rpm.

TH-2949_166122105

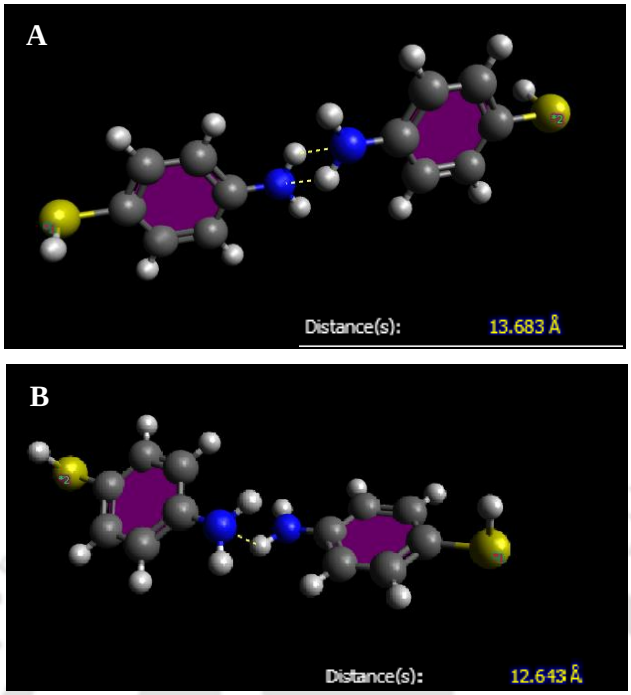

Figure A2.5. Energy optimized computed geometry of dimerized 4-ATP molecule at the hot-spot of the assembled Au NRs bridged via (**A**) two H-bonds and (**B**) one H-bond.

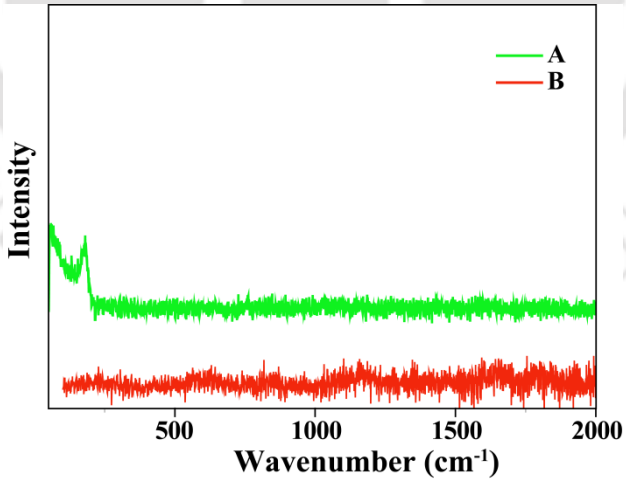

Figure A2.6. Raman spectra recorded for (**A**) CTAB stabilized Au NRs and (**B**) glass substrate.

TH-2949_166122105

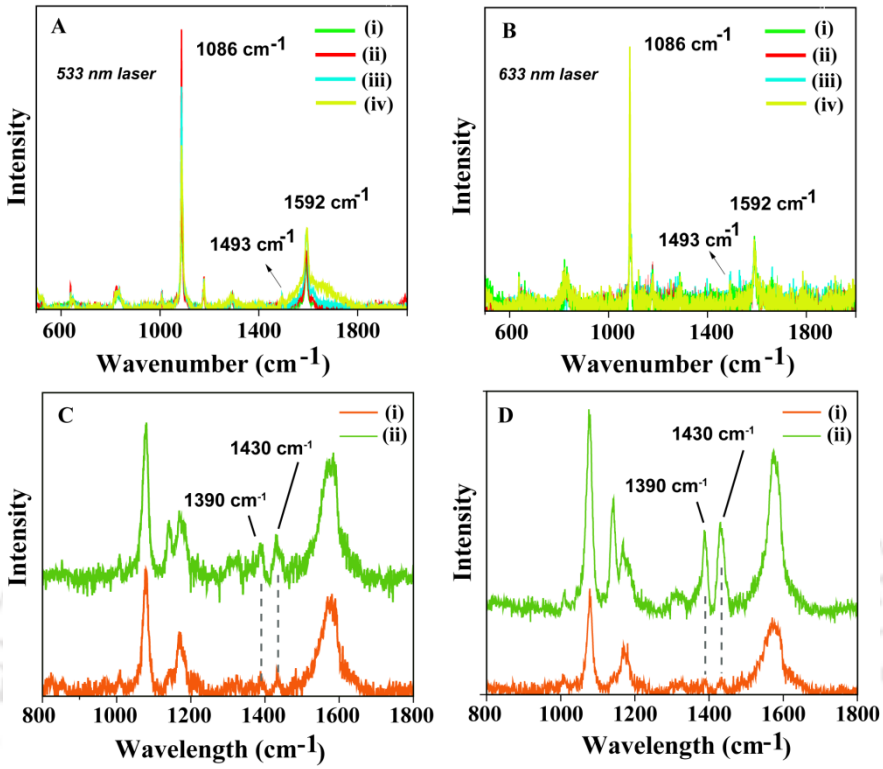

Figure A2.7. Time dependent normal Raman spectra of 4-ATP (250 mM) recorded at time intervals of (**i**) 2 min, (**ii**) 4 min, (**iii**) 6 min and (**iv**) 8 min with (**A**) 532 nm and (**B**) 632 nm laser excitation. Time dependent monitoring of oxidative coupling reaction of 4-ATP on assembled Au NRs recorded using 632.8 nm laser excitations after irradiation with (**C**) 532 nm and (**D**) 632.8 nm laser at (**i**) 0 min and at an interval of (**ii**) 2 min each. (Acquisition time 5s, 20x objective)

TH-2949_166122105

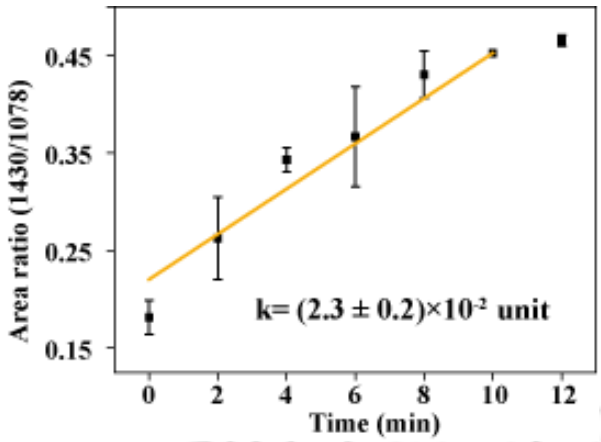

Figure A2.8. Normalized plot of area under the curve at 1430 cm^{-1} obtained with respect to different time interval of laser exposure at 0.75 mW. Data points (first five) so obtained were fitted to linear graph and rate constant values for zero order kinetics were extracted from the slope of the plot of normalized intensity versus time. For rate constant calculation, the final datum point shown in the above plot is neglected. They are, however, included in the plot to indicate the completion of reaction.

TH-2949_166122105

CHAPTER 3

The effect of several metal cations (Mn^{2+}, Co^{2+}, Ni^{2+}, Cu^{2+} and Zn^{2+}) on the photochemical conversion of 4-ATP into DMAB is probed using SERS. The coupling reaction is carried out on the surface of Au nanoparticle and Au nanorod using 532 nm and 632.8 nm laser excitations, respectively, in absence and in presence of metal cations. Here, we report that DMAB formation on the surface of Au nanostructures - when carried out in the solid state - is augmented significantly (by a factor of 1.98 to 4.07 and 3.34 to 5.74 for Au nanoparticles and Au nanorods substrates, respectively, and depending on the metal). Furthermore, the SERS signal is also markedly enhanced. Thus, the results underpin a new way of carrying out photochemical reaction with higher yield along with higher SERS signal.

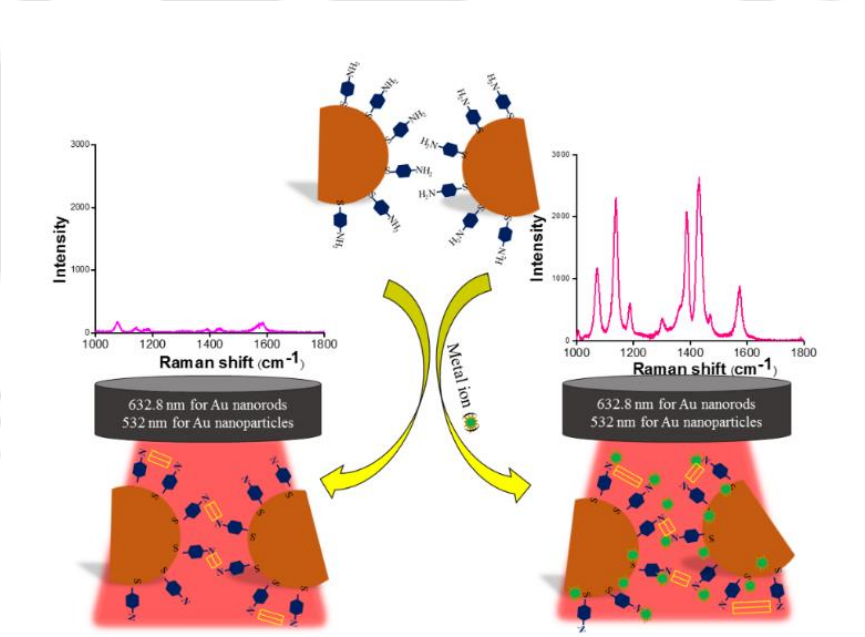

Ref.: Pal, S.; Paul, S.; Chattopadhyay, A. Enhanced Solid-State Plasmon Catalyzed Oxidation and SERS Signal in the Presence of Transition Metal Cations at the Surface of Gold Nanostructures. *Phys. Chem. Chem. Phys.* 2021, *23*, 21808-21816.

TH-2949_166122105

3.1. Introduction

LSPR excitation in metal nanoparticles by electromagnetic radiation has been proposed to provide a new opportunity for chemical catalysis especially in the presence of visible light.[1,2] The collective oscillations, in the presence of resonant electromagnetic radiation, produce hot-electrons on the surface that could help reduce the energy barrier of the reaction.[3] Since silver and gold metal nanoparticles exhibit visible and near infrared light LSPR excitations they represent prominent candidates for commercially viable plasmonic chemical catalysis. The low energy requirement of reactions also has helped generate interests in studying product-selective and high throughput plasmonic heterogeneous catalysis.[4-10] The popular choice for pursuing new ideas in this regard are the reduction of nitrothiophenol and oxidation of 4-ATP on silver and gold nanoparticles.[7,11,12] It is important to mention here that SERS is often used to study kinetics and mechanisms of plasmon catalyzed reactions.[11,13] This also helps in pursuing both plasmonic reactions and probing the product through SERS by the same laser excitation.

An important reaction that has been studied recently in respect of plasmonic catalysis is the conversion of 4-ATP to DMAB.[14-16] Investigations revealed that the reaction can be influenced by pH, O_2 , laser wavelength, laser intensity, laser exposure time, solvent and the nature of the metal nanoparticles.[17-27] Importantly, interest in visible light induced plasmon catalysis has brought renewed focus on the reaction as a test case with emphasis on the factors that can influence the rate and mechanism of the oxidation reaction. The mechanism of the plasmon catalyzed oxidation reaction depends on two main factors: 1) activation of surrounding oxygen by hot electrons and 2) the generation of holes to facilitate the oxidation process.[23,28] An interesting knowledge that might help in pursuing such reaction is that metal ions could be incorporated on the surface of plasmonic particles such as gold nanorods.[29] On the other hand, metal ions such as Ag^{+}, Au^{3+}, Pt^{4+} and Hg^{2+} have been reported to help drive the plasmon driven 4-ATP to DMAB reaction that was probed using SERS.[30] Thus, a question arises on whether the product formation is limited to the presence of those four metal ions only. This is important for addressing as knowledge about the possibility of the same or different reactions in the presence of other metal ions would help bring generality and versatility of the idea. It may be mentioned here that the referred reaction was carried

TH-2949_166122105

out in the liquid medium and in the presence of only above four metal ions. On the other hand, evaporation of such dispersion – consisting of metal cations and 4-ATP stabilized gold nanoparticles – may lead to increase in local concentrations of the metal ions in the solid state. The increased local concentrations of metal ions in turn might have led to subsequent chemical reaction with enhancement in yield and thus SERS signals for DMAB. That may be considered as an important possibility to be explored.

Herein we report that significant enhancement of yield of plasmonic conversion of 4-ATP to DMAB was observed through SERS probe in the solid state, and in the presence of metal cations such as Mn^{2+}, Co^{2+}, Ni^{2+}, Cu^{2+} and Zn^{2+}. The enhancement was observed for both gold nanoparticles and gold nanorods being used as the plasmon materials. Also, excellent improvement in the signal of the product DMAB was observed for the reaction with probe laser wavelength of 532 as well as 632.8 nm. Accompanying the oxidation of 4-ATP into DMAB in the presence of Au nanostructures and metal ions, it is proposed that the oxidation states of the metal ions underwent changes during the reaction and metal oxides were possibly formed in the process. This supports not only the higher yield of the product on the nanostructure surface but also so-formed metal oxide induced enhancement of Raman signal.

3.2. Experimental Section

3.2.1. Materials: Gold(III) chloride solution (30 wt. % in dilute HCl), hexadecyltrimethylammonium bromide (CTAB), silver nitrate, l-ascorbic acid, 4-aminothiophenol (4-ATP), cobalt(II) acetate tetrahydrate and nickel(II) acetate tetrahydrate were purchased from Sigma-Aldrich (India). Trisodium citrate dihydrate, sodium borohydride, manganese(II) acetate tetrahydrate, copper(II) acetate monohydrate, zinc acetate dihydrate and methanol were bought from Merck (India). All the chemicals were used without further purification. For all synthesis and experimental works, Milli-Q (MQ) grade water was used. All borosilicate glassware was cleaned with aqua regia.

3.2.2. Synthesis of CTAB Stabilized Spherical Au Nanoparticles: CTAB capped spherical gold nanoparticles were synthesized by following seed-mediated route reported by Fenger et al.[31]

TH-2949_166122105

Preparation of seed solution: 10 mL 2.5×10^{-4} M $HAuCl_4$ aqueous solution was added to 10 mL 2.5×10^{-4} M trisodium citrate aqueous solution while stirring. Color of the mixture became reddish-brown after addition of 0.3 mL freshly prepared, ice-cold aqueous 0.1 M sodium borohydride solution quickly at a time while vigorous stirring. This indicated the formation of gold seed solution. It was kept undisturbed and used after 1 h for the growth of CTAB stabilized spherical gold nanoparticles.

Seeding growth of CTAB capped Au nanoparticles: 20 mL clear amber colored aqueous solution containing 0.08 M CTAB and 2.5×10^{-4} M $HAuCl_4$ was used as growth solution. For our experiment, suitable CTAB capped Au nanoparticles were prepared at room temperature in two steps from the growth solution. In the first step, 9 mL growth solution was taken in a culture tube, which became colorless after addition of 50 μL of 0.1 M l-ascorbic acid solution dropwise while vigorous stirring. To that, 1 mL of seed solution was added at a time and stirring was continued for 10 min. The resultant deep purple colored solution was used as seed for the second step. In the second step, again 50 μL of 0.1 M l-ascorbic acid solution was mixed with 9 mL growth solution and 1 mL of deep purple colored solution prepared in the first step was added and stirring was continued for 10 min. Color of the CTAB capped Au nanoparticles obtained in this step was lighter than that of the first step. It was then purified by centrifugation (10,000 rpm for 15 min at 10°C), re-dispersed in 12 mL MQ grade water and stored at room temperature for further experiments.

3.2.3. Synthesis of CTAB Stabilized Au Nanorods: CTAB capped Au nanorods were prepared by reported seed mediated growth method.[32]

Preparation of gold seed: 1.0 mL aqueous solution containing 8.4×10^{-3} M $HAuCl_4$ was added dropwise into 15 mL aqueous solution of 0.1 M CTAB with gentle shaking. After 45 s, into the light amber mixture, freshly prepared, ice-cold 2 mL 0.01 M sodium borohydride solution was added at a time with vigorous shaking which, was continued up to 2 min. Then the reddish-brown mixture was kept undisturbed and after 2 h was used for the growth of Au nanorods.

Growth of CTAB capped Au nanorods: Aqueous solutions of 1.0 mL 8.4×10^{-3} M $HAuCl_4$, 0.2 mL 0.01 M $AgNO_3$ and 0.8 mL 0.01 M l-ascorbic acid, respectively, were added dropwise into 15 mL aqueous solution of 0.1 M CTAB with gentle shaking. Finally, into the

TH-2949_166122105

colorless mixture, 20 μL seed solution was added at a time followed by gentle shaking for 10 s and then the mixture was kept undisturbed for 15 h. The synthesized Au nanorod was purified by centrifugation of the dispersion at 10000 rpm for 15 min at 10 °C and was re-dispersed in 15 mL Milli-Q grade water.

3.2.4. Characterization and Instruments: (i) UV-Vis spectra were recorded using PerkinElmer® Lambda 35 double beam UV-Vis spectrophotometer, (ii) Raman spectra were recorded from Horiba LabRAM HR Evolution microscope Raman instrument attached with 532 nm and 632.8 nm lasers. Baseline subtractions were done in LabSpec 6 software equipped with the Raman instrument, (iii) TEM images were obtained using JEOL JEM-2100 transmission electron microscope (operating voltage 200 kV) and (iv) Energy-dispersive X-ray spectroscopy (EDS) mapping was done using Zeiss model Sigma field emission scanning electron microscope (FESEM).

3.2.5. 4-ATP functionalization and sample preparation for Raman spectroscopy: 200 μL solution of 7.2×10^{-4} M 4-ATP in 1:1 methanol-water mixture was added dropwise in 12 mL of as-synthesized Au nanostructure solution (Au nanoparticle and Au nanorod, separately) and stirred for 15 h. Then it was divided into a set of six vials each containing 2 mL of the mixture and thereafter each of them was centrifuged at 6000 rpm for 20 min at 15 °C. Precipitate from each sample was then re-dispersed in 0.7 mL deionized water by sonication. Out of six, five samples were taken for further reaction with metal ions Mn^{2+}, Co^{2+}, Ni^{2+}, Cu^{2+} and Zn^{2+}. 20 μL of 3.6×10^{-2} M metal(II) acetate solution was added with 0.7 mL of re-dispersed mixture so that the final concentration of metal ion in the resultant mixture was 1×10^{-3} M and stirred for 2 h.

3.2.6. Samples for FESEM EDS analysis and SERS measurement: Thin film was made by drop-casting 2 μL mixture of each sample on pre-cleaned aluminum foil for FESEM EDS analysis.

For SERS measurement an aliquot of 20 μL mixture from each sample was drop-cast on a pre-cleaned rectangular borosilicate glass slide and was then dried in vacuum desiccator. For samples of Au nanoparticles, all Raman spectra were recorded from the thin film developed on the glass substrate using 25% of 50 mW laser (at 532 nm wavelength) with acquisition time of 10 s and accumulation number of 2 under 20x microscopic objective lens. Diffraction

TH-2949_166122105

grating was set at 600 gr/mm. For samples of Au nanorods, 632.8 nm wavelength laser (50% of 16 mW) was used to record spectra. Measurements were done using 100× microscopic objective lens with acquisition time 2 s, accumulation number 2 and diffraction grating 1800 gr/mm.

3.3. Results and Discussions

Cetyltrimethylammonium bromide (CTAB) - stabilized Au nanoparticles and Au nanorods were synthesized following reported seed mediated growth routes [31,32] (**Experimental section**).

UV-Vis Spectra and TEM Images Analysis

Figure 3.1Ai shows the UV-Vis spectrum of the as-synthesized gold nanoparticles with absorption maximum at 527 nm. On the other hand, **Figure 3.1Bi** shows UV-Vis spectrum of the as-synthesized gold nanorods with absorption bands at 517 nm and 713 nm, representing transverse and longitudinal modes, respectively. TEM of the as-synthesized uniform-sized Au nanoparticles is shown in **Figure 3.1Ci** and the average particle size was calculated to be 23.9±2.3 nm **(Appendix, Figure A3.1Ai)**. Given the extensive literature on the influence of the size of nanoparticle in the enhancement of SERS,[33] our interest was centered on the effect of metal cations on the photochemical conversion of 4-ATP into DMAB on surface of different Au nanostructures. Since Au nanoparticle having ~25 nm diameter represents a model particle for SERS enhancement, we have attempted to generalize the effect of metal cation on the oxidation reaction of 4-ATP into DMAB by using the same. TEM image of the as-synthesized gold nanorods shown in **Figure 3.1Di** revealed the aspect ratio of 4.2±0.5 **(Appendix, Figure A3.1Bi)** and the average length and breadth of Au nanorods used were 52.67 (±3.44) and 12.55 (±1.25) nm, respectively. Plasmonic property of Au nanorod depends on its length and breadth (longitudinal and transverse modes)[34-35]. Thus, it is speculated that with the change in length and breadth of Au nanorod, it might affect the conversion of 4-ATP into DMAB. Since we were interested on the catalytic effect of metal cations on the conversion of 4-ATP into DMAB at the surface of different Au nanostructures (Au nanoparticle and Au nanorod), we focused more on the metal cations keeping the lengths and breadths of Au nanorod unchanged.

TH-2949_166122105

As-synthesized gold nanostructures (both gold nanoparticles and gold nanorods, separately) were treated with 4-ATP and the mixtures were allowed to stir for 15 h. (**Described in experimental section**). This was followed by centrifugation of the reaction mixture and then redispersion into water. The presence of a broad second peak - at 712 nm - in the UV-Vis spectrum of 4-ATP attached Au nanoparticles shown in **Figure 3.1Aii** indicated that there might have been assembled structures in the dispersion. The assembly formation could have taken place through hydrogen bonding between 4-ATP molecules attached to the nanoparticles. The formation of assembled structures of Au nanoparticles was further confirmed through TEM measurements the results of which are shown in **Figure 3.1Cii**. The images revealed the formation of linear as well as higher order assembly of the nanoparticles. On the other hand, there was no additional peak in the UV-Vis spectrum of 4-ATP attached Au nanorod samples as shown in **Figure 3.1Bii.** The results **i**ndicated lack of assembled structure formation in the dispersion. This was further supported by TEM result as shown in **Figure 3.1Dii**.

Since both the layers (internal-layer along with the outer-layer) of positively charged CTAB bilayer on the surface of Au nanoparticle are in dynamic equilibrium with the medium[36] thus it was easier for 4-ATP molecules to get attached to Au nanoparticles on their surfaces, possibly through the thiol group. During precipitation through centrifugation the so-attached 4-ATP molecules of one nanoparticle formed hydrogen bonds with 4-ATP molecules of another nanoparticle.[37] The change in the UV-Vis characteristic spectra of Au nanoparticles in the presence of 4-ATP indicated assembly formation.

On the other hand, only the outer layer of CTAB bilayer on the surface of Au nanorod is in dynamic equilibrium with the medium but the internal layer is more permanent.[36] This might have prevented significant attachment of 4-ATP molecules on the surface of Au nanorods although enough reaction time was given and in addition, it also restricted the formation of hydrogen bonds through the above mechanism. Thus, upon centrifugation at lower speed (6000 rpm) the presence of CTAB molecules prevented association of Au nanorods during precipitation.

TH-2949_166122105

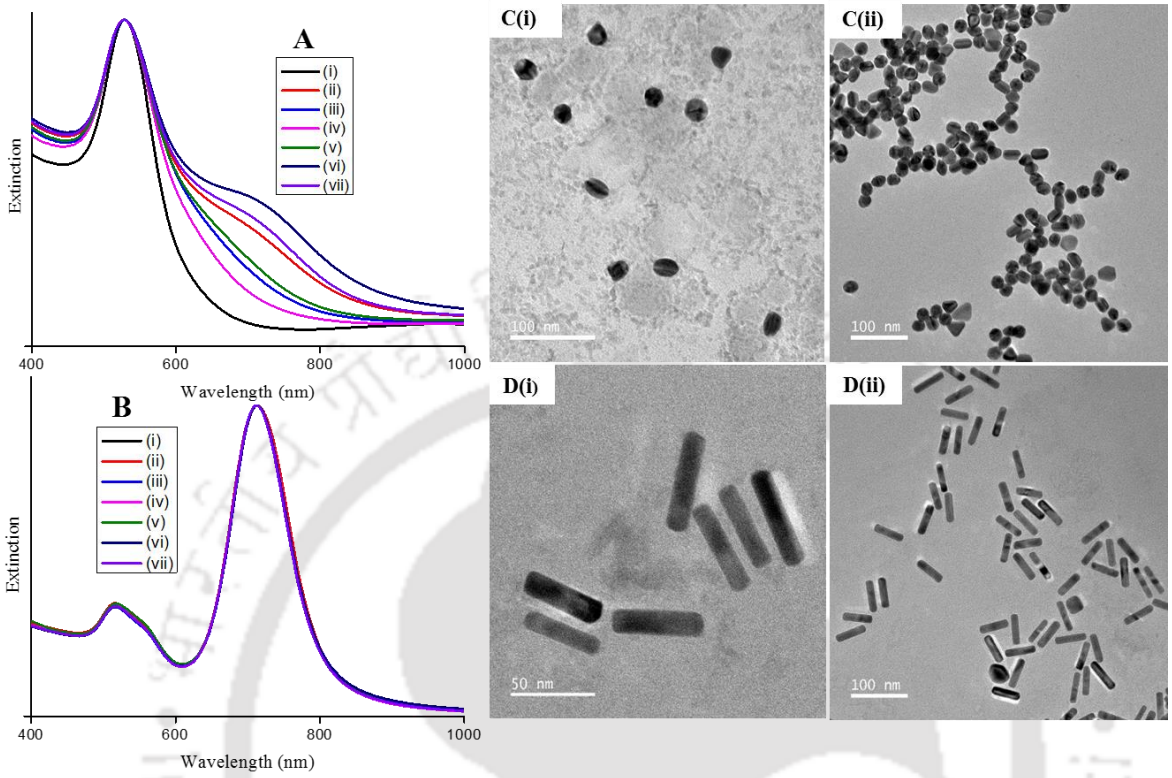

Figure 3.1. (**A**) UV-Vis spectra of (**i**) as-synthesized Au nanoparticles, (**ii**) 4-ATP attached Au nanoparticles, and 4-ATP attached Au nanoparticles in presence of (**iii**) Mn^{2+}, (**iv**) Co^{2+}, (**v**) Ni^{2+}, (**vi**) Cu^{2+} and (**vii**) Zn^{2+}, respectively. (**B**) UV-Vis spectra of (**i**) as-synthesized Au nanorods, (**ii**) 4-ATP attached Au nanorods, and 4-ATP attached Au nanorods in the presence of (**iii**) Mn^{2+}, (**iv**) Co^{2+}, (**v**) Ni^{2+}, (**vi**) Cu^{2+} and (**vii**) Zn^{2+}, respectively. **(C)** TEM images of **(i)** as-synthesized Au nanoparticles, **(ii)** 4-ATP attached Au nanoparticles with samples prepared after centrifugation and redispersion**. (D)** TEM images of **(i)** as-synthesized Au nanorods, **(ii)** 4-ATP attached Au nanorods with samples prepared after centrifugation and redispersion.

Following centrifugation and re-dispersion, the 4-ATP attached Au nanostructures (Au nanoparticles and nanorod systems, separately) were treated with metal cations (Mn^{2+}, Co^{2+}, Ni^{2+}, Cu^{2+} and Zn^{2+} ions, independently) and were allowed to stir for 2 h. Next, UV-Vis spectra of 4-ATP attached Au nanoparticles - in the presence of Mn^{2+}(**iii**), Co^{2+}(**iv**), Ni^{2+}(**v**), Cu^{2+}(**vi**) or Zn^{2+}(**vii**) cation - were recorded and the results are shown in **Figure 3.1A.** The appearance of a second peak at about 712 nm could be observed (**Figure 3.1A**). Although

TH-2949_166122105

the clarity and broadness of the second peak differed for different metal ion, it was there nonetheless for all metal cation added dispersions. The metal cation can interact with 4-ATP molecule through the lone pair of electrons on nitrogen.[38] In 4-ATP attached gold nanoparticle assembly, presence of metal cation possibly interfered with the hydrogen bonding interaction between 4-ATP molecules leading to different levels of assembly resulting in different absorbance at the second peak as shown in the UV-Vis spectra (**Figure 3.1A (iii, iv, v, vi, vii))**. UV-Vis spectra of Au nanoparticles in the presence of metal cations (used for the current studies) did not indicate significant aggregation in the medium (**Appendix, Figure A3.2**). Thus, the assembly formation in the medium consisting of Au nanoparticles might have been induced by 4-ATP molecules. TEM images of the samples of 4-ATP attached gold nanoparticles in presence of metal cations (Mn^{2+}, Co^{2+}, Ni^{2+}, Cu^{2+} and Zn^{2+}, separately) were also recorded**.** Investigation of the images, as shown in **Figure 3.2A,** suggest that the assembled structures of gold nanoparticles were largely retained in the presence of metal cations thus supporting the observations with respect to the UV-Vis spectra.

On the other hand, when metal cations were added to 4-ATP attached Au nanorod dispersions (following the same procedure as in the case of Au nanoparticles), no distinct changes in the UV-Vis spectra were observed, as are shown in **Figure 3.1B (iii, iv, v, vi, vii).** Investigation of TEM images shown in **Figure 3.2B** also underpins that there were no apparent changes in the structures of Au nanorods in the presence of metal cations in the media. The results generally suggest that 4-ATP-stablized Au nanoparticles were more prone to assembly formation whether metal cations were present in the medium or not. Hydrogen bonding between the stabilizing 4-ATP molecules could be the primary reason for such assembly formation. On the other hand, such hydrogen bonding may not be feasible in the case of Au nanorods and thus they were present in the media (even in the presence of metal cations) as independent entities.

TH-2949_166122105

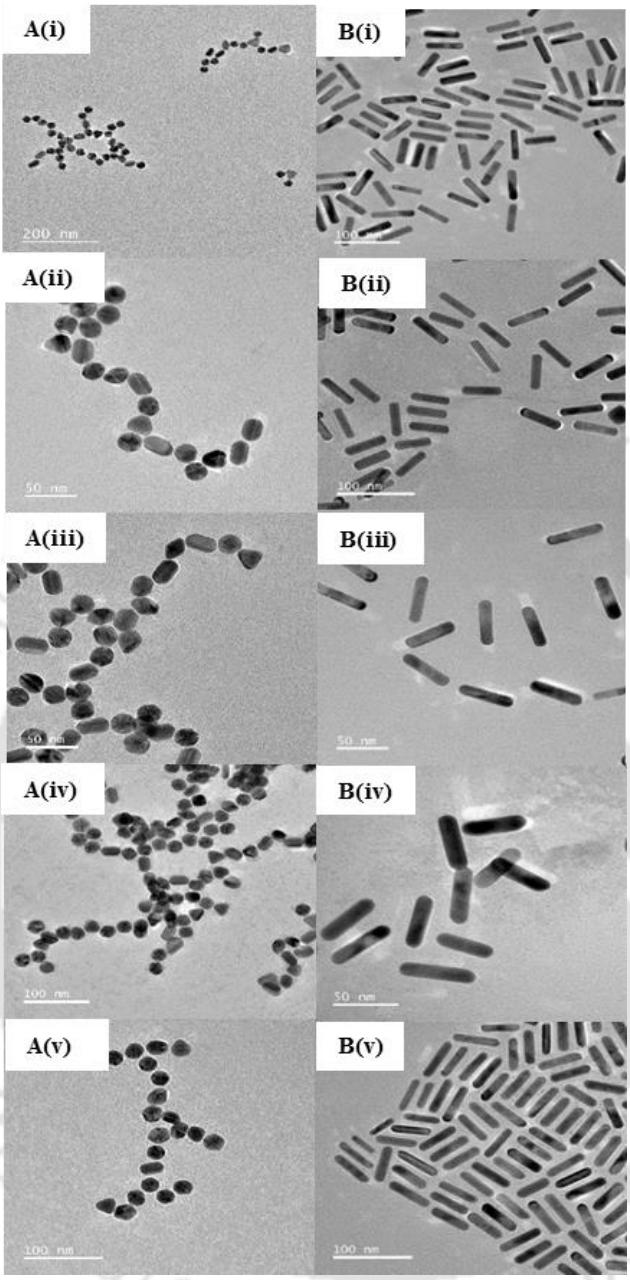

Figure 3.2. (**A**) TEM images of samples of (**i**) 4-ATP attached Au nanoparticles in the presence of Mn^{2+}, (**ii**) Co^{2+}, (**iii**) Ni^{2+}, (**iv**) Cu^{2+}, (**v**) Zn^{2+}, respectively. (**B**) TEM images of samples of (**i**) 4-ATP attached Au nanorods in the presence of Mn^{2+}, (**ii**) Co^{2+}, (**iii**) Ni^{2+}, (**iv**) Cu^{2+} and (**v**) Zn^{2+}, respectively.

UV-Vis spectrum shown in **Figure 3.1B (vii)** indicates that there was no clear assembly formation upon addition of Zn^{2+} ions to 4-ATP attached Au nanorod dispersion. The absence

TH-2949_166122105

of an additional peak or shift of any of the two peaks could be attributed to the lack of assembly formation in the medium. On the other hand, the image in **Figure 3.2B (V)** indicates that the apparent formation of assembly as observed in TEM could have been induced by evaporation during sample preparation.

SERS Measurements

We were interested in pursuing the effects of metal cations on the photochemical conversion of 4-ATP to DMAB in the presence of Au nanoparticles or nanorods. Also, as mentioned before, SERS was used as probe for the same. A schematic diagram of the process for the photochemical conversion of 4-ATP into DMAB in absence and in presence of metal cations on the surface of Au nanostructures is presented in **Scheme 3.1**.

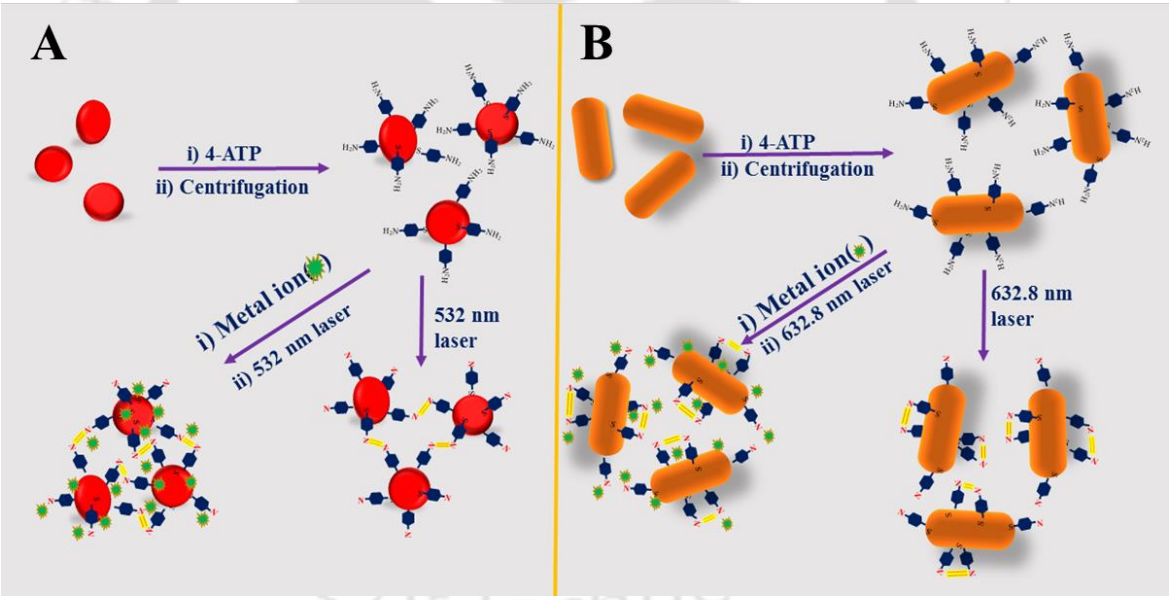

Scheme 3.1. Cartoon diagram of (**A**) photochemical conversion of 4-ATP into DMAB in the presence and in absence of metal cations on the surface of Au nanoparticles and (**B**) photochemical conversion of 4-ATP into DMAB in the presence and in absence of metal cations on the surface of Au nanorods.

Sample preparations for recording Raman spectra of 4-ATP attached Au nanostructures in absence and in presence of metal ions haves been described in the experimental section. When 4-ATP attached Au nanostructure was irradiated using laser (with the probe laser

TH-2949_166122105

wavelength of 532 nm for Au nanoparticle substrate and 632.8 nm for Au nanorod substrate), immediate photochemical conversion of 4-ATP into DMAB was observed. Although the laser excitation wavelengths (i.e., 532 nm and 632.8 nm) do not match exactly with the peaks of the assembled Au nanoparticles (which occurred at 527 nm) and that of Au nanorods (which occurred at 713 nm), the proximity of the respective excitation wavelength to the peak was sufficient to have observed excellent Raman signal in the SERS spectra. It may be mentioned here that the Raman signal intensities of the peaks originated due to 4-ATP at the surface of Au nanoparticles was much higher when excited at 532 nm as compared to that at 633 nm (**Appendix, Figure A3.3**). The success of the reaction was evident by the appearance of characteristic peaks at 1388 cm^{-1} (ν_{NN} + ν_{CN}) and 1430 cm^{-1} (ν_{NN} + β_{CH}) due to ring stretching vibration of azo (─N═N─) group in DMAB [39] (**Figure 3.3A & B**). In addition, C–N symmetric stretching vibration appeared at 1138 cm^{-1}, indicating the trans-geometry of DMAB.[40]

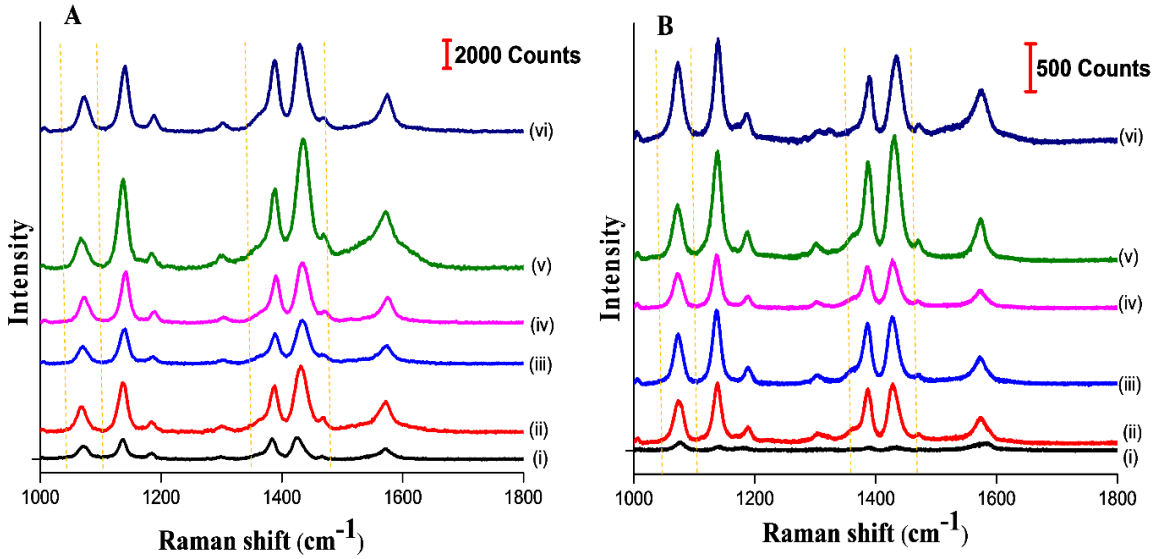

Figure 3.3. (**A**) SERS spectra of DMAB produced from (**i**) 4-ATP attached Au nanoparticles (S), (**ii**) 4-ATP attached Au nanoparticles in presence of Mn^{2+}, (**iii**) Co^{2+}, (**iv**) Ni^{2+}, (**v**) Cu^{2+}, (**vi**) Zn^{2+} when irradiated with laser (λ_{ex}: 532 nm, acquisition time: 10s). (**B**) SERS spectra of DMAB produced from (**i**) 4-ATP attached Au nanorods, (**ii**) 4-ATP attached Au nanorods in presence of Mn^{2+}, (**iii**) Co^{2+}, (**iv**) Ni^{2+}, (**v**) Cu^{2+}, (**vi**) Zn^{2+} when irradiated with laser (λ_{ex}: 632.8 nm, acquisition time: 2s).

TH-2949_166122105

The aggregation of Au nanoparticles due to 4-ATP was discernible. However, it was not more pronounced in the presence of meal cations. In addition, there could be additional aggregation due to evaporation of the liquid sample. However, the results suggest that the effect of metal cation on the yield and rate of reaction was more pronounced than that due to aggregation.

Mechanism of 4-ATP into DMAB Conversion

Under laser irradiation NH_2 groups of two molecules of 4-ATP on the surface of Au nanostructures were oxidized to N=N with the elimination of hydrogens.[41] We observed that the intensity of the SERS peaks for the product DMAB increased in the presence of laser light and metal cations, thus representing the product yield enhancement. When 4-ATP molecule was oxidized into DMAB at the surface of gold nanostructures, metal ions were consequently reduced. This might have been followed by oxidation into metal oxide.[30,41] The sequence of reactions leading to DMAB formation and consequent enhancement of Raman signal are shown below.[30,41] The proposition is further supported by literature reports of significant SERS effect by transition metal and their oxides.[39,40]

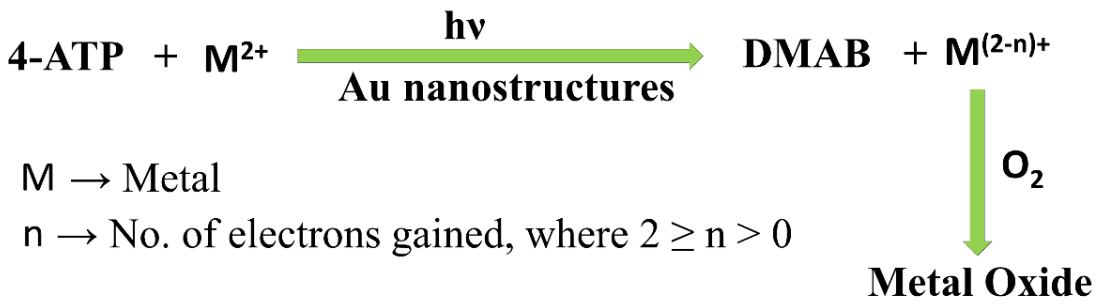

Herein we report that the peak at 1076 cm^{-1} (due to $\nu_{CC} + \nu_{CS}$) was significantly shifted in the SERS spectra recorded in the presence of both metal cations and Au nanostructures (**Appendix, Figure A3.4**). Interestingly, the peak at 1430 cm^{-1} (due to ring stretching vibration of azo (─N═N─) group in DMAB) was red-shifted in the presence of metal cations on the surface of Au nanorods but on the surface of Au nanoparticles the peak was red-shifted in the presence of Ni^{2+} or Co^{2+} ions and was blue-shifted in the presence of Mn^{2+},

TH-2949_166122105

Cu^{2+} or Zn^{2+} ions. As discussed before, literature reports suggest that while 4-ATP is converted to DMAB on the surface of a plasmon-active coinage metal nanostructure and in the presence of metal ion, the metal ions are consequently converted to plasmon-active metal oxide on the surface.[30,41] The product DMAB may well be chemically bonded to these newly formed metal oxide surface. Thus, not only the reduction potential and reactivity towards 4-ATP, of the metal ion, but also the properties of plasmon active oxide would determine the Raman peak intensity and frequency of the product DMAB. The DMAB bonded to different plasmon active metal oxides formed in the process might have led to different Raman frequencies as observed. This is further supported by the results of the experiments involving benzenethiol. When benzenethiol was treated with metal ion at the surface of Au nanostructures, which was followed by exposure to the appropriate laser, there was negligible change in the Raman peak (due to $\nu_{CC} + \nu_{CS}$) as shown in **Figure A3.5** and **Figure A3.6** (**Appendix**). It is plausible that the metal ions did not chemically interact with benzenethiol and were also not converted to their oxides upon exposure to laser radiation. Therefore, there was no discernible change in the peak intensity and positions of benzenethiol. Thus, we may conclude that the metal ion interacted with the 4-ATP molecules - possibly through binding with the amine group leading to DMAB formation.

FESEM and EDS Mapping Analysis

We have performed experiments that involved pursuing mapping of ions present on the surface of Au nanostructures when evaporated on Al foil surface. These experiments were performed using field emission scanning electron microscopy (FESEM) and EDS on the same spots (**Appendix, Figure A3.7**). The nature of depositions of both the Au nanostructures and metal ions were akin to the samples on which Raman scattering experiments were performed. As are evident from the images the metal ions were present on the pinned spots (of the original evaporating liquids) consisting of Au nanoparticles or nanorods. Although metal ions were also present on the other parts of the sample surface, that the ions were present on the nanostructures and that the reactions were carried out exclusively on those spots also supports the presence and thus influence of the metal ions on the reactions.

TH-2949_166122105

Yield (of DMAB) Enhancement and SERS Signal Enhancement

It may be mentioned here that the fast conversion of 4-ATP into DMAB under the reaction conditions prevented us from making any measurement with regard to the rates of the reactions. Therefore, we were interested in pursuing calculations of the intensity increment especially in the presence of metal ions on the basis of the intensity of peak at 1076 cm^{-1} as this peak was prominently present in both the reactant (4-ATP) and the product (DMAB). Intensity enhancement was calculated as the ratio of area under the curve positioned at 1076 cm^{-1} (metal ion added sample) to that of the 1076 cm^{-1} (metal ion free sample) and the calculated results are shown in **Figure A3.8** (**Appendix**). It may be rather difficult to obtain highly reproducible values for solid samples as for each probe spot the number of metal nanoparticles and thus the sample compound (and also metal ion) concentration may not be identical. Therefore, we measured Raman spectra for each sample (20 different spots) and we also used 3 different samples for analysis of the results related to the addition of each ion. As are clear from **Figure A3.8** (**Appendix**), the signal enhancements for all the samples containing one metal ion – and for both the nanoparticle and nanorod containing samples - were at least an order of magnitude higher than the samples containing no added metal ion. The results clearly indicated the role of metal ions used for the experiments in enhancing the signal of plasmon enhanced Raman scattering. Control experiments involving benzenethiol on the surface of Au nanoparticles and nanorods indicated no significant change in the Raman signal in the presence of metal ions (**Appendix, Figure A3.6**), thus discounting the effect of the ions as such on the signal intensity.

It may be mentioned here that relative change in intensity at 1076 cm^{-1} (due to $\nu_{CC} + \nu_{CS}$) indicated the enhancement of the peak following the product formation in both the cases as that in the presence of metal ions as compared to that in absence. On the other hand, notwithstanding the enhancement of both the peaks, the ratio of product azo peak at 1430 cm^{-1} to that at 1076 cm^{-1} ought to have remained the same in case the metal ion did not alter the product yield. Thus, the increase in the ratio of the peaks suggested product yield enhancement with the azo peak representing the product DMAB exclusively. Bar diagrams representing DMAB formation from 4-ATP in absence and in the presence of metal ions at the surface of Au nanostructures are shown in **Figure 3.4**. The results indicated that from

TH-2949_166122105

4-ATP the product DMAB was produced on the surface of Au nanoparticles (**Figure 3.4A**) with yield of 1.55±0.60 under laser irradiation (532 nm) in absence of metal cation. However, in the presence of metal cations (and laser irradiation at 532 nm) the reaction from 4-ATP produced DMAB with yields of 3.5±0.83 (for Mn^{2+}), 3.62±0.91 (for Co^{2+}), 3.11±0.71 (for Ni^{2+}), 6.31±2.01 (for Cu^{2+}) and 3.07±0.54 (for Zn^{2+}), respectively, for the samples with metal ions mentioned in the parentheses.

On the other hand, the same reaction of 4-ATP to DMAB when carried out on the surface of Au nanorods (**Figure 3.4B**), the yield was 0.58±0.16 in absence of metal cation; however, in the presence of metal cations the yields were 2.58±0.32 (for Mn^{2+}), 2.52±0.51 (for Co^{2+}), 2.21±0.30 for Ni^{2+}), 3.33±0.91 (for Cu^{2+}) and 1.94±0.55 (for Zn^{2+}), respectively, for the metal cations mentioned in the parentheses.

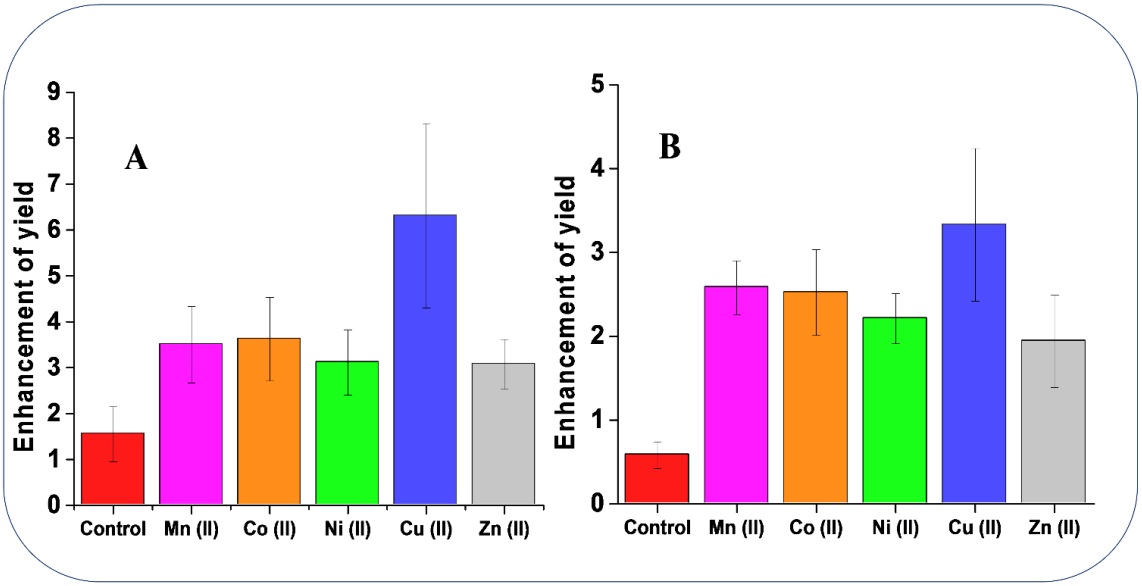

Figure 3.4. (**A**) Yield enhancement of 4-ATP attached Au nanoparticles in absence (control) and in presence of different metal ions as mentioned in the legends (Mn^{2+}, Co^{2+}, Ni^{2+}, Cu^{2+} and Zn^{2+}); (**B**) Yield enhancement of 4-ATP attached Au nanorods in absence (control) and presence of different metal ions mentioned in the legends (Mn^{2+}, Co^{2+}, Ni^{2+}, Cu^{2+} and Zn^{2+}). Yield (of DMAB) enhancement in the presence of metal ion was calculated as the ratio of area under the curve for peak at 1430 cm^{-1} to that at 1076 cm^{-1}.

TH-2949_166122105

Since it is easier for 4-ATP molecules to attach on the surface of Au nanoparticle than on the Au nanorod, the number of 4-ATP molecules present on the surface of Au nanoparticles and Au nanorods might not have been the same, even though we maintained the same 4-ATP concentration in the dispersion medium. Experimental parameters such as laser excitation wavelengths were also different for two different systems. Thus, we were unable to compare the results (signal enhancement and yield enhancement) between Au nanorod and Au nanoparticle systems.

3.4. Conclusions

Transformation of 4-ATP into DMAB was not only catalyzed by plasmons of Au nanoparticles and Au nanorods in the solid state but also the product yield increased significantly in the presence of metal ions. The results suggest that increase in the product yield in the presence of plasmonic field and metal ion may be a general phenomenon as opposed to what has been reported in the liquid phase for a few metal cations.[30] Thus, the oxidation states of the metal ions might have undergone changes during the conversion from 4-ATP into DMAB with possible formation of metal oxides in the process.[30, 41] This might have led to the higher yield of the product on the Au nanostructure surface as well as the so-formed metal oxide induced augmentation of Raman signal.[30,41] Thus, the product yield of any plasmonic oxidation reaction may be augmented in presence of metal cation. The enhancement in the product yield as well as the reaction rate could help in carrying out other important reactions on the surface of plasmonic-nanostructures and in the presence of metal cation. The observation of metal ion enhanced plasmon catalyzed oxidation reaction may help bring new ideas in the up and coming field of plasmon catalyzed reactions.

3.5. References

1. Ye, J.; Hutchison, J. A.; Uji-i, H.; Hofkens, J.; Lagae, L.; Maes, G.; Borghs, G.; Dorpe, P. V. *Nanoscale* **2012**, *4*, 1606.

2. Shen, Y.; Miao, P.; Hu, C.; Wu, J.; Gao, M.; Xu, P. *ChemCatChem* **2018**, *10*, 3520.

TH-2949_166122105

3. Cao, E.; Guo, X.; Zhang, L.; Shi, Y.; Lin, W.; Liu, X.; Fang, Y.; Zhou, L.; Sun, Y.; Song, Y.; Liang, W.; Sun, M. *Adv. Mater. Interfaces* **2017**, *4*, 1700869.

4. Linic, S.; Christopher, P.; Xin, H.; Marimuthu, A. *Acc. Chem. Res.* **2013**, *46*, 1890.

5. Aslam, U.; Chavez, S.; Linic, S. *Nature Nanotech.* **2017**, *12*, 1000.

6. Christopher, P.; Xin, H.; Linic, S. *Nature Chem.* **2011**, *3*, 467.

7. Sun, M.; Xu, H. *Small* **2012**, *8*, 2777.

8. Zhang, Z.; Fang, Y.; Wang, W.; Chen, L.; Sun, M. *Adv. Sci.* **2016**, *3*, 1500215.

9. Zhang, Z.; Xu, P.; Yang, X.; Liang, W.; Sun, M. *Journal of Photochemistry and Photobiology C: Photochemistry Reviews* **2016**, *27*, 100.

10. Zhang, Z.; Lacroix, M. R.; Deckert, V. *Faraday Discuss.* **2017**, *205*, 2013.

11. Ren, X.; Cao, E.; Lin, W.; Song, Y.; Liang, W.; Wang, J. *RSC Adv.* **2017**, *7*, 31189.

12. Wang, J.; Ando, R. A.; Pedro, H. C. C. *Angew. Chem. Int. Ed.* **2015**, *54*, 6909.

13. Yan, X.; Wang, L.; Tan, X.; Tian, B.; Zhang, J. *Sci. Rep.* **2016**, *6*, 30193.

14. Choi, H. K.; Shon, H. K.; Yu, H.; Lee, T. G.; Kim, Z. H. *J. Phys. Chem. Lett.* **2013**, *4*, 1079.

15. Huang, Y. F.; Zhu, H. P.; Liu, G. K.; Wu, D. Y.; Ren, B.; Tian, Z. Q. *J. Am. Chem. Soc.* **2010**, *132*, 9244.

16. Wu, D. Y.; Liu, X. M.; Huang, Y. F.; Ren, B.; Xu, X.; Tian, Z. Q. *J. Phys. Chem. C* **2009**, *113*, 18212.

17. Wang, J. L.; Ando, R. A.; Camargo, P. H. C. *ACS Catal.* **2014**, *4*, 3815.

18. Xu, J. F.; Luo, S. Y.; Liu, G. K. *Spectrochimica Acta Part A: Molecular and Biomolecular Spectroscopy* **2015**, *143*, 35.

19. Xu, P.; Kang, L.; Mack, N. H.; Schanze, K. S.; Han, X.; Wang, H. L. *Sci. Rep.* **2013**, *3*, 2997.

20. Sun, M.; Huang, Y.; Xia, L.; Chen, X.; Xu, H. *J. Phys. Chem. C* **2011**, *115*, 9629.

TH-2949_166122105

21. Canpean, V.; Astilean, S. *Spectrochimica Acta Part A: Molecular and Biomolecular Spectroscopy* **2012**, *96*, 862.

22. Xu, J. F.; Liu, G. K. *Spectrochimica Acta Part A: Molecular and Biomolecular Spectroscopy* **2015**, *138*, 873.

23. Qiao, Q.; Shan, C. X.; Zheng, J.; Zhu, H.; Yu, S. F.; Li, B. H.; Jia, Y.; Shen, D. Z. *Nanoscale* **2013**, *5*, 513.

24. Nelson, D. A.; Schultz, Z. D. *J. Phys. Chem. C* **2018**, *122*, 8581.

25. Wu, H. Y.; Lai, Y. H.; Hsieh, M. S.; Lin, S. D.; Li, Y. C.; Lin, T. W. *Adv. Mater. Interfaces* **2014**, *1*, 1400119.

26. Tan, E.; Yin, P.; Yu, C.; Yu, G.; Zhao, C. *Spectrochimica Acta Part A: Molecular and Biomolecular Spectroscopy* **2016**, *166*, 15.

27. Liu, Y.; Yang, D.; Zhao, Y.; Yang, Y.; Wu, S.; Wang, J.; Xia, L.; Song, P. *Heliyon* **2019**, *5*, e01545.

28. Papa, L.; Freitas, I. C. D.; Geonmonond, R. S.; Aquino, C. B. D.; Pieretti, J. C.; Domingues, S. H.; Ando, R. A.; Camargo, P. H. C. *J. Mater. Chem. A* **2017**, *5*, 11720.

29. Baaske, M. D.; Vollmer, F. *Nature Photon.* **2016**, *10*, 733.

30. Zhang, Z.; Merk, V.; Hermanns, A.; Unger, W. E. S.; Kneipp, J. *ACS Catal.* **2017**, *7*, 7803.

31. Fenger, R.; Fertitta, E.; Kirmse, H.; Thünemann, A. F.; Rademann, K. *Phys. Chem. Chem. Phys.* **2012**, *14*, 9343.

32. Sau, T. K.; Murphy, C. J. *Langmuir* **2004**, *20*, 6414.

33. Hong, S.; Li, X. *Journal of Nanomaterials* **2013**, *2013*, 790323.

34. Lin, K. Q.; Yi, J.; Hu, S.; Liu, B. J.; Liu, J. Y.; Wang, X.; Ren, B. *J. Phys. Chem. C* **2016**, *120*, 20806-20813.

35. Gu, G. H.; Kim, M. Y.; Yoon, H. J.; Suh, J. S. *Bull. Korean Chem. Soc.* **2014**, *35*, 725.

TH-2949_166122105

36. Barbero, F.; Moriones, O. H.; Bastús, N. G.; Puntes, V. *Bioconjugate Chem*. **2019**, *30*, 2917-2930.

37. Pal, S.; Dutta, A.; Paul, M.; Chattopadhyay, A. *J. Phys. Chem. C* **2020**, *124*, 3204.

38. Lang, X. F.; Yin, P. G.; Tan, E. Z.; You, T. T.; Guo, L. *J. Raman Spectrosc.* **2013**, *44*, 425.

39. Huang, Y. F.; Wu, D. Y.; Zhu, H. P.; Zhao, L. B.; Liu, G. K.; Ren, B.; Tian, Z. Q. *Phys. Chem. Chem. Phys.*, **2012**, *14*, 8485.

40. Ye, Y.; Liu, H.; Yang, L.; Liu, J. *Nanoscale* **2012**, *4*, 6442.

41. Yu, L.; Ma, L.; Liu, Y.; Song, P.; Xia, L. *J. Raman Spectrosc.* **2020**, *51*, 838.

TH-2949_166122105

Appendix of Chapter 3: A3

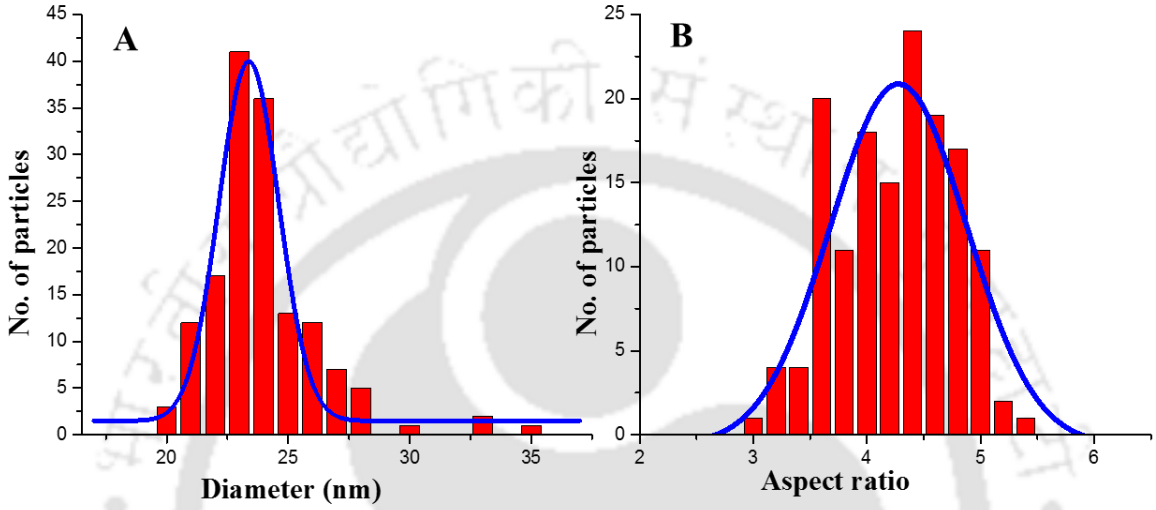

Figure A3.1. (A) Size distribution of as-synthesized Au nanoparticles. **(B)** Size distribution of as-synthesized Au nanorods.

TH-2949_166122105

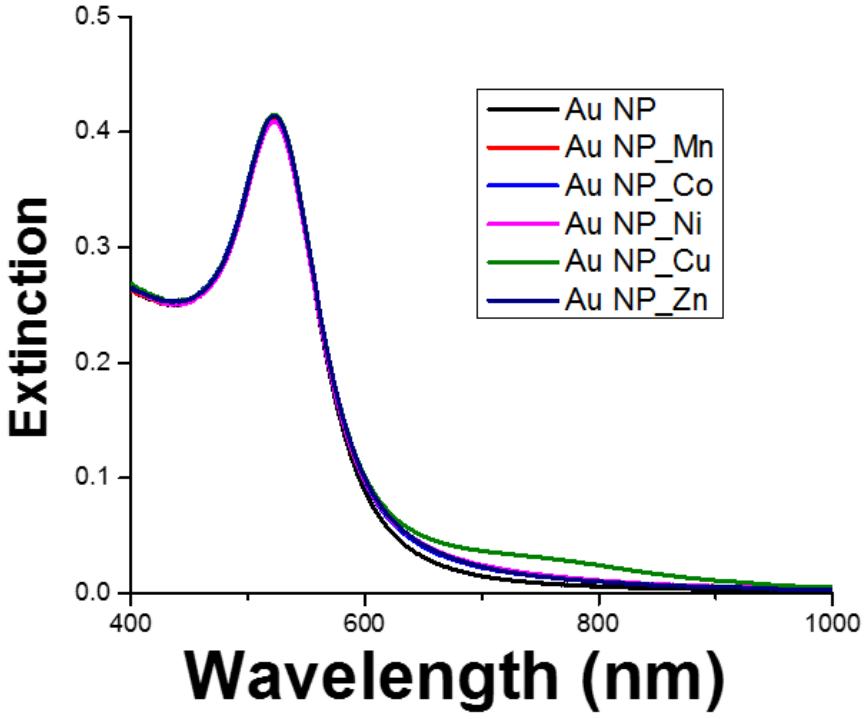

Figure A3.2. UV-Vis spectra of Au nanoparticles (Au NP) in absence and in presence of different metal cations. The concentration of the metal cations in the medium was kept at 1 mM.

TH-2949_166122105

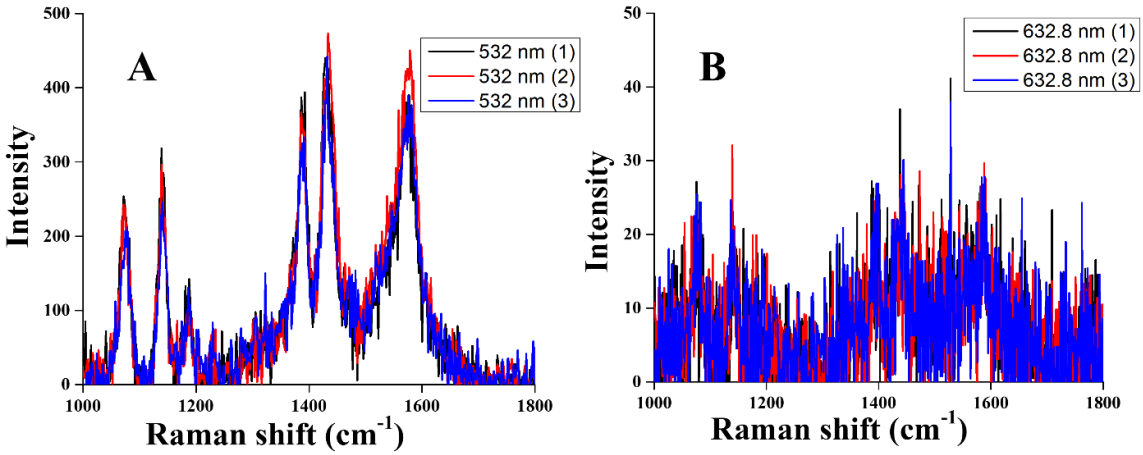

Figure A3.3. SERS spectra of 4-ATP attached Au nanoparticles recorded at laser excitations of 532 nm (**A**) and 632.8 nm (**B**), respectively, at three different spots (1, 2 and 3).

Description: From **Figure 3.1A** it is observed that – in the presence of 4-ATP - sharp intense plasmon band of Au nanoparticle occurred at 527 nm, which was strong as compared to its second plasmon band at 712 nm. Thus, in order to get the maximum Raman signal enhancement from Au nanoparticle systems as shown in **Figure A3.3,** we recorded all the Raman measurements with 532 nm laser excitation as it is closer to 527 nm. Further, as is clear from the figure, the Raman signal intensities of the peaks originated due to 4-ATP was much higher when excited at 532 nm as compared to that at 633 nm.

TH-2949_166122105

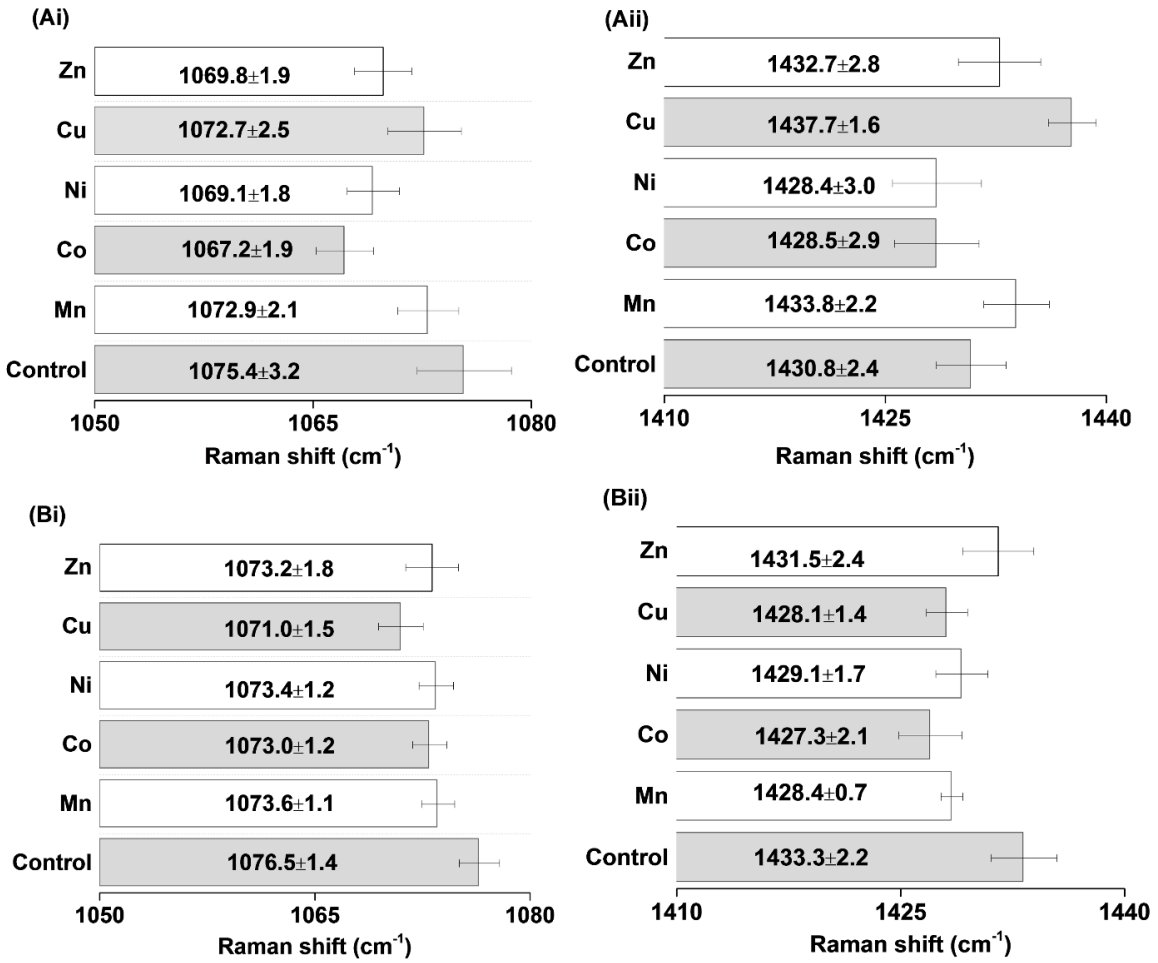

Figure A3.4. (**A**) Raman shift of peaks of DMAB produced on the surface of Au nanoparticle in absence (control) and presence of different metal ions. (**B**) Raman shift of peaks of DMAB produced on the surface of Au nanorod in absence (control) and presence of different metal ions ('i' represents peak due to $\nu_{CC} + \nu_{CS}$ and 'ii' represents peak due to ring stretching vibration of azo (─N═N─) group in DMAB).

TH-2949_166122105

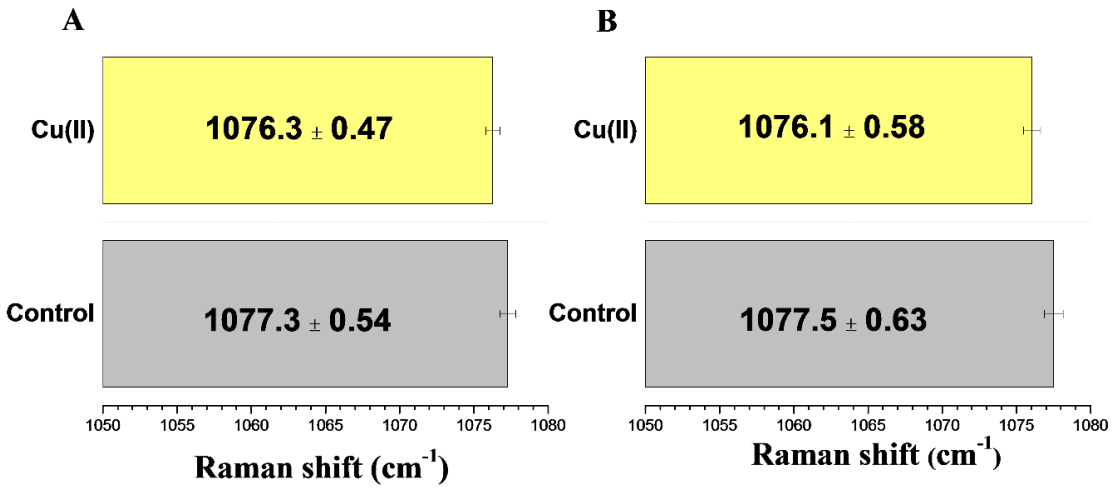

Figure A3.5. (**A**) Raman peak (due to $\nu_{CC} + \nu_{CS}$) of benzenethiol attached to Au nanoparticle in absence (control) and presence of Cu^{2+} ions. (**B**) Raman peak (due to $\nu_{CC} + \nu_{CS}$) of benzenethiol attached to Au nanorod in absence (control) and presence of Cu^{2+} ions. Since the effect of Cu^{2+} ion was maximum among those five metal ions on the conversion of 4-ATP into DMAB, this control experiment with benzenethiol was pursued using Cu^{2+} metal ion only.

TH-2949_166122105

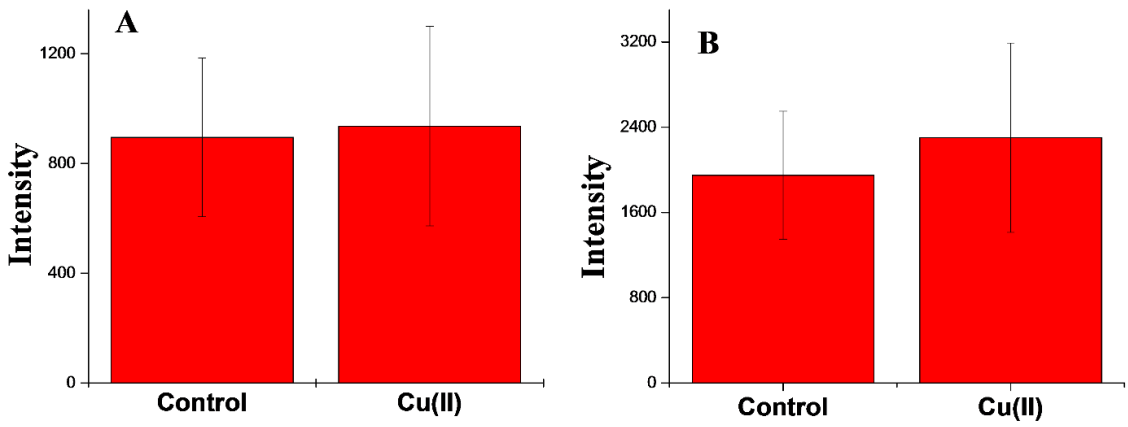

Figure A3.6. (**A**) SERS intensity of benzenethiol attached to Au nanoparticle in absence (control) and presence of Cu^{2+} ions. (**B**) SERS intensity of benzenethiol attached to Au nanorod in absence (control) and presence of Cu^{2+} ions. (**Since the influence of Cu^{2+} ion was maximum among those five metal ions used for the conversion of 4-ATP into DMAB, this control experiment with benzenethiol was performed using Cu^{2+} metal ion**).

TH-2949_166122105

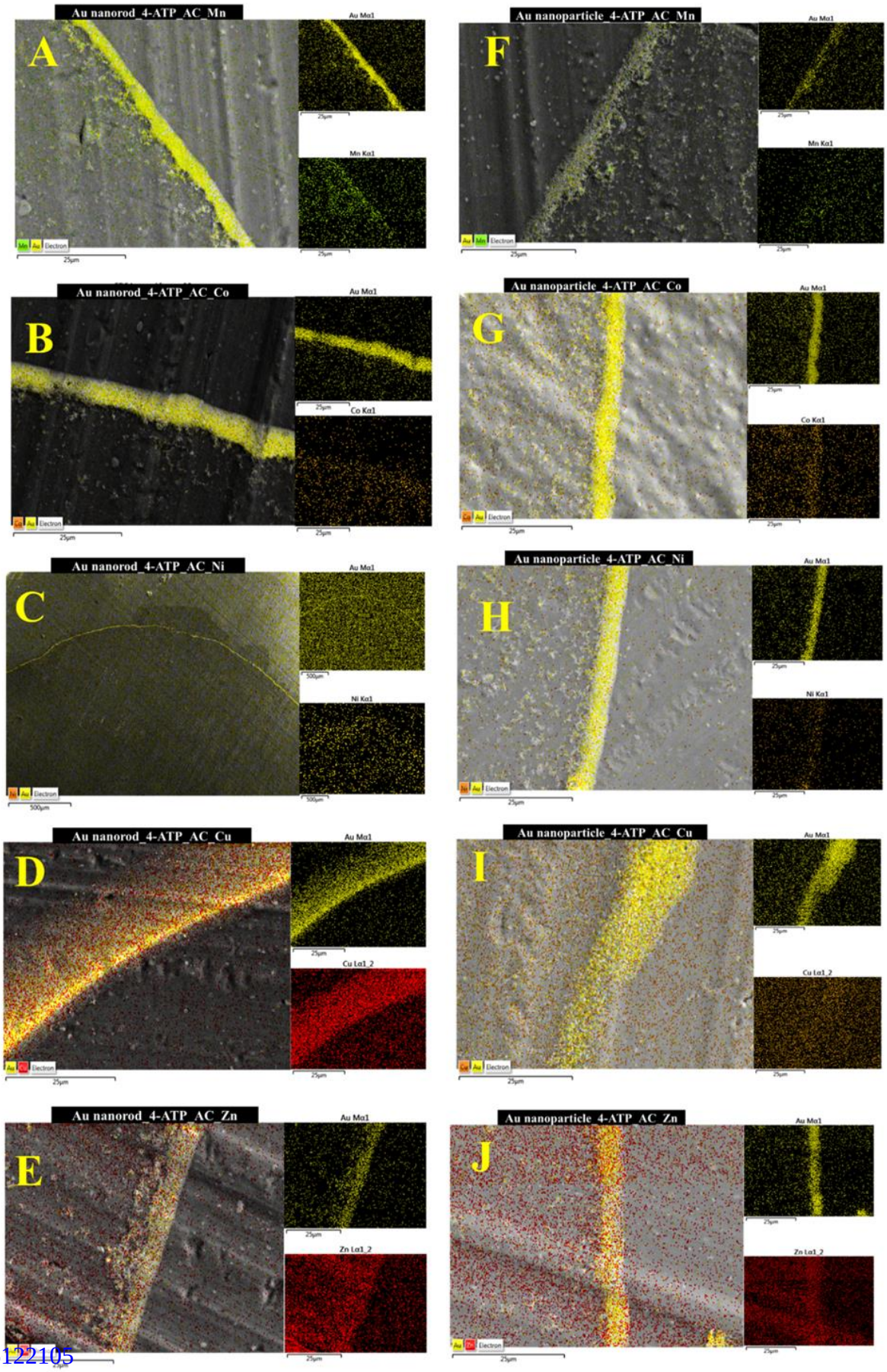

TH-2949_166122105

Figure A3.7. EDS mapping of 4-ATP attached Au nanorod in presence of (**A**) Mn^{2+}, (**B**) Co^{2+}, (**C**) Ni^{2+}, (**D**) Cu^{2+} or (**E**) Zn^{2+} ions and EDS mapping of 4-ATP attached Au nanoparticle in presence of (**F**) Mn^{2+}, (**G**) Co^{2+}, (**H**) Ni^{2+}, (**I**) Cu^{2+} or (**J**) Zn^{2+}ions, respectively.

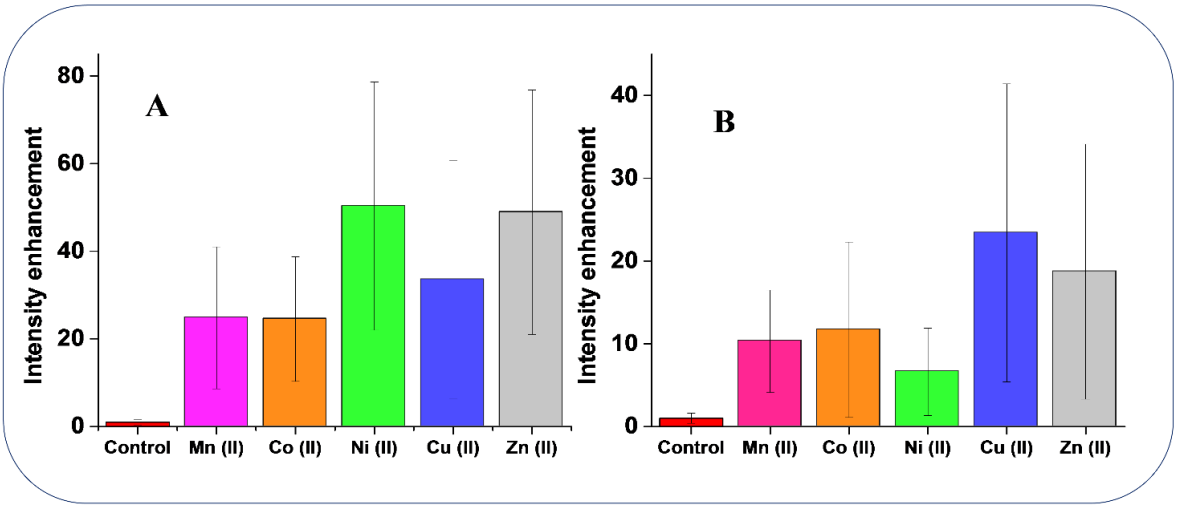

Figure A3.8. (**A**) Signal enhancement of 4-ATP attached to Au nanoparticle in absence (control) and presence of different metal ions. (**B**) Signal enhancement of 4-ATP attached to Au nanorod in absence (control) and presence of different metal ions.

Enhancement factor calculation:

$$\text{Enhancement factor} = \frac{I_{sers(\text{metal ion added})} \times N_{(\text{metal ion free})}}{I_{sers(\text{metal ion free})} \times N_{(\text{metal ion added})}}$$

where $N_{(\text{metal ion free})} = N_{(\text{metal ion added})}$ = Number of 4-ATP molecules attached on the surface of Au nanostructures, whereas $I_{sers(\text{metal ion added})}$ is the measured average intensity (considering area under the corresponding curve) of metal ion containing 4-ATP attached Au nanostructures sample and $I_{sers(\text{metal ion free})}$ is the measured average intensity (considering area under the corresponding curve) of metal ion free 4-ATP attached Au nanostructures sample. Hence the signal enhancement was calculated as the ratio of area under the curve positioned at 1076 cm^{-1} (metal ion added sample) to that of the 1076 cm^{-1} (sample without additional metal ions).

TH-2949_166122105

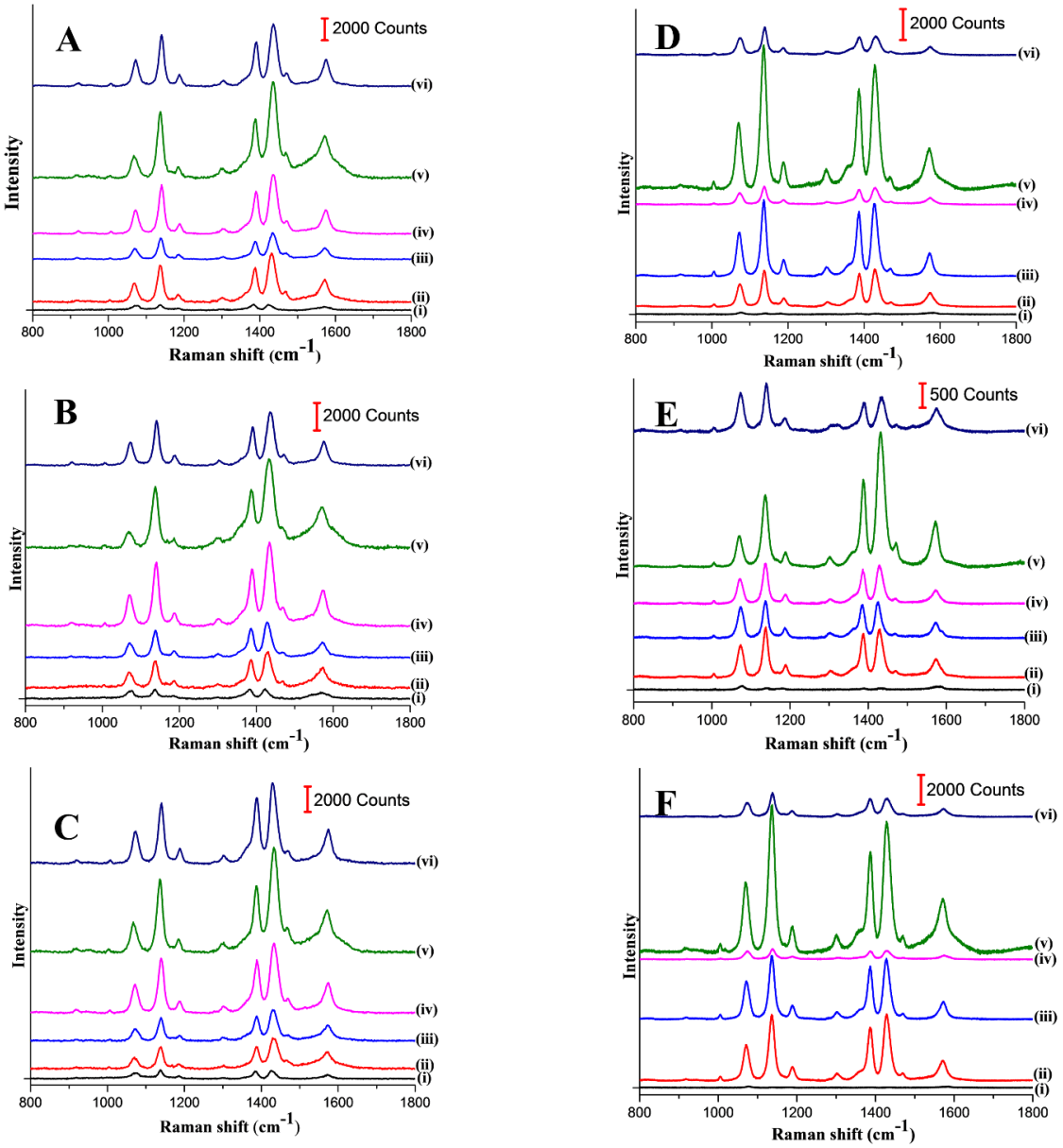

Figure A3.9. (**A-C**) SERS spectra of DMAB produced from (**i**) 4-ATP attached Au nanoparticles, (**ii**) 4-ATP attached Au nanoparticles in presence of Mn^{2+}, (**iii**) Co^{2+}, (**iv**) Ni^{2+}, (**v**) Cu^{2+}, (**vi**) Zn^{2+} when irradiated with laser (λ_{ex}: 532 nm, acquisition time: 10s), respectively. (**D-F**) SERS spectra of DMAB produced from (**i**) 4-ATP attached Au nanorods, (**ii**) 4-ATP attached Au nanorods in presence of Mn^{2+}, (**iii**) Co^{2+}, (**iv**) Ni^{2+}, (**v**) Cu^{2+}, (**vi**) Zn^{2+} when irradiated with laser (λ_{ex}: 632.8 nm, acquisition time: 2s), respectively. In continuation

TH-2949_166122105

with Figure 3.3, this additional figure is in support of the reproducibility of the metal ion effect on the photochemical conversion of 4-ATP to DMAB.

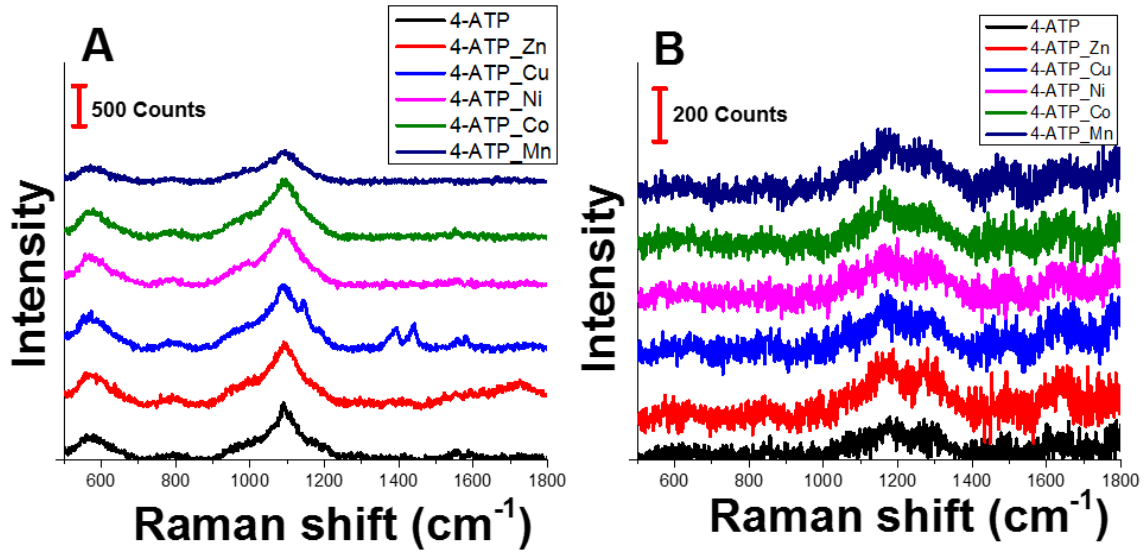

Figure A3.10. Raman spectra of 4-ATP in absence and in presence of different metal cations at laser excitations of 532 nm (**A**) and 632.8 nm (**B**), respectively.

Description: From the **Figure A3.10**, it is evident that photochemical conversion of 4-ATP into DMAB was not feasible (or at least not discernible herein) without the surface of Au nanostructures either in absence or presence of metal cations (Mn^{2+}, Co^{2+}, Ni^{2+} and Zn^{2+}). Since the reduction potential of Cu^{2+}/Cu is much higher compared to other metal cations (Mn^{2+}, Co^{2+}, Ni^{2+} and Zn^{2+}), Cu^{2+} ion is readily reduced by the oxidation of 4-ATP into DMAB, producing possibly nanoscale metallic copper in the vicinity. This in turn might have resulted in the observed enhancement of the yield and rate of reaction. Thus, photochemical conversion of 4-ATP into DMAB was feasible only (although with low yield) in the presence of Cu^{2+} ion without need of the surface of Au nanostructures as shown in **Figure A3.10A.**

TH-2949_166122105

CHAPTER 4

We report the catalytic formation of bridged polynuclear peroxo complex of Co(II) and 2-picolylamine (2-PA) in aqueous alkaline medium on the surface of Au nanoparticle. The reaction followed sigmoidal kinetics both in absence and presence of Au nanoparticle with an order of magnitude higher rate constant in the presence of nanoparticle. Importantly, using UV-Vis spectroscopy, mass spectrometry and SERRS, we conclude the formation of peroxo complex with 2-PA acting as a monodentate ligand. The absorbance of the polynuclear complex at 595 nm and the extinction maximum of (agglomerated) Au nanoparticles at 750 nm provided the right opportunity to pursue SERRS using 632.8 nm laser excitation. Density functional theoretical calculation indicated that the lowering of HOMO-LUMO energy gap of 2-PA bonded to the nanoparticle surface helped catalyze the reaction.

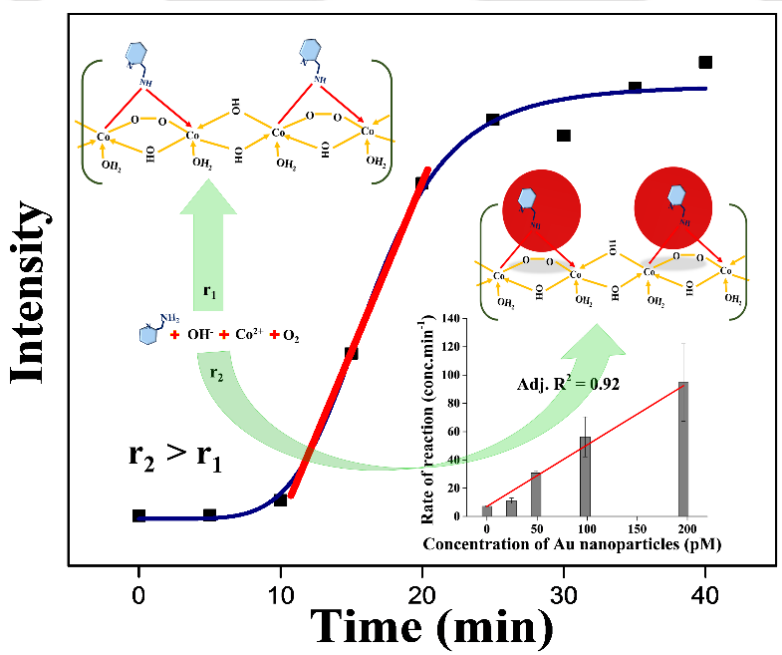

Ref.: Pal, S.; Paul, S.; Chattopadhyay, A. Dual Role of Au Nanoparticles in the Catalytic Formation of an Amorphous Polynuclear Peroxo Complex and Surface Enhanced Resonance Raman Scattering. *ChemistrySelect* 2022, *7*, e202201569.

TH-2949_166122105

4.1. Introduction

The introduction of coinage metal nanoparticles such as those of Au and Ag - with their strong extinction of visible light – helped bring a leap of applications of SERS in order to probe vibrational signatures of molecules under a plethora of conditions.[1-3] Thus, molecular vibrations with low change in polarizability could be probed with greater ease in the presence of not only bonding to the metal surface but also localized plasmonic field. The Raman scattering signal is further improved by up to two orders of magnitude when a resonance or near resonance condition is achieved with the molecular electronic state.[4,5] The combination of the two – referred to as SERRS – provides the best of opportunity in pursuing vibrational probes of an analyte down to single molecule level.[4-9] SERRS provides a mean to understand the structure, bonding and kinetics of formation of inorganic complexes under in situ reaction conditions that are not amenable to many other spectroscopic techniques. Also, the technique has the inherent advantage of studying such complexation reaction in the presence of Au or Ag as catalyst as well as plasmonic nanoparticle.

Inorganic complexes are specifically pertinent candidates for study. For example, cobalt is an essential trace element in human body and plays important roles in functions of vitamin B_{12}. Thus, understanding of the structure and function of the central complexes is key to the knowledge of the workings of the co-enzymes. Among others, 2-PA based cobalt complexes have received great recent interests in the synthesis of metal complexes having open coordination sites or to mimic non-heme dioxygenase.[10] Cobalt complexes with 2-PA moieties are deemed important for their potential antitumor activities.[10,11] In addition, they have been considered as hypoxia-activated prodrugs.[12] Biological activities of Schiff-base complex between cobalt and 2-PA are extensively studied in coordination chemistry because of the enhanced activities as compared to non – Schiff-base complex.[13] Moreover, cobalt complexes with 2-PA moieties have been considered as potential hydrogen-evolving catalysts under both the light-driven and electrochemical conditions.[14,15]

On the other hand, the peroxo complexes of transition metals exhibit catalytic activity and can thus act as active oxidants for organic and inorganic substrates.[16,17] But the synthesis of metal peroxo complex in aqueous medium, under ambient conditions, remains a challenge. Interestingly, a few decades ago, a report proposed the formation of hydroxo-

TH-2949_166122105

polynuclear species when Co(II) reacts with 2-PA (acting as bidentate ligand) under basic condition.[18] However, the nature of the complex and polymerization were not established and there was no experimental evidence for the structure of the products. This is an important reaction that has consequences in several applications and thus needs to be studied in further details.

Herein we report the use of SERRS to pursue in situ the formation of bridged polynuclear peroxo complex from the reaction of Co(II) with 2-PA in aqueous alkaline medium and under ambient conditions. The complexation reaction followed sigmoidal kinetics with the appearance of a peak at 595 nm in the UV-Vis spectrum that helped in following the reaction using resonance Raman spectroscopy at 633 nm laser excitation. Further, using mass spectrometry we established the structure of the polynuclear peroxo complex that was consistent with the results of Raman spectroscopy. Importantly, the reaction when carried out in the presence of Au nanoparticles occurred also with sigmoidal kinetics but with as much as an order of magnitude higher rate. The presence of Au nanoparticles and the peak due to the peroxo complex allowed us to probe the reaction using SERRS that revealed that 2-PA was bound to cobalt ion as a monodentate ligand while the other nitrogen was bonded to Au nanoparticle. The results also indicated identical Co(III)-2-PA peroxo complex formation in the presence as well as absence of Au nanoparticles.

4.2. Experimental Section

4.2.1. Materials: 2-PA, gold(III) chloride (30 wt. % in HCl), cobalt(II) acetate tetrahydrate, trisodium citrate dihydrate, sodium hydroxide, hydrogen peroxide (50%). All the chemicals were purchased from Sigma-Aldrich (India) and used without further purification. For all the experimental works, Milli-Q (MQ) grade water was used.

4.2.2. Au nanoparticle synthesis: Citrate stabilized Au nanoparticles were synthesized using a reported method.[19] 13.6 mg of trisodium citrate was dissolved in 25 mL MQ grade water and then the solution was heated at 120 °C while stirring. After 1 h, 123 µL of 29 mM $HAuCl_4$ was added into the solution. After sometime, the color of the reaction mixture appeared red representing the formation of Au nanoparticles. The reaction mixture was allowed to stir for 30 min more. Then the red colored reaction mixture was cooled to room

TH-2949_166122105

temperature and centrifuged at 20,000 rpm for 6 min. The obtained precipitate was dispersed into 12.5 ml MQ grade water and stored at room temperature for further use.

4.2.3. Bridged polynuclear complex synthesis: 50 µL of 0.5 M 2-PA solution was added into the 3 mL of 196 pM Au nanoparticle dispersion. Then 50 µL of 21 mM cobalt(II) acetate solution was added into the reaction mixture followed by the addition of 25 µL of 1 M sodium hydroxide solution. After 15 min the reaction mixture turned into blue, which represents the formation of bridged polynuclear complex. The above experiment was carried out with four more different concentrations of Au nanoparticles (98, 49, 24.5 and 0 pM).

4.2.4. Instruments: (i) Raman spectra were recorded using Horiba LabRAM HR Evolution microscope Raman instrument attached with 532, 632.8 and 784.5 nm lasers. (ii) UV-Vis spectra were measured using PerkinElmer® Lambda 35 double beam UV-Vis spectrophotometer. (iii) JEOL JEM-2100 transmission electron microscope (operating voltage 200 kV) was used to obtain TEM images, EDS and selected area electron diffraction (SAED). (iv) Mass spectral data were collected using Agilent Accurate Mass Spectrometer (Q-TOF 6520) by Electrospray Ionization (ESI) method in negative mode. (v) ^{1}H NMR measurements were done using 500 MHz NMR instrument.

4.3. Results and Discussions

When 2-PA was treated with Co(II) in the presence of base (pH 11), the reaction mixture immediately turned into yellow (**Figure A4.1A**, **Appendix**) with the appearance of a peak at 379 nm in the UV-Vis spectrum as shown in **Figure 4.1A**. Then the reaction mixture slowly turned blue with a peak at 595 nm (**Figure 4.1A**). Time-dependent UV-Vis study (**Figure 4.1A**) revealed that the absorbance due to the peak at 595 nm increased (and dominated the peak at 379 nm) with time, indicating the formation of the product. When 2-PA was reacted with Co(II), initially (at 0 min and in absence of a peak at 595 nm) characteristic peaks of the reactant (2-PA) as well as the product were absent in the Raman spectrum (λ_{ex}: 632.8 nm) as shown in **Figure 4.1B**. With the progress of the reaction, the Raman signal (λ_{ex}: 632.8 nm) intensity increased (**Figure 4.1B)** in concurrence with the absorbance at 595 nm (**Figure 4.1A**).

TH-2949_166122105

Literature report proposes complexation followed by polymerization as a result of reaction of Co(II) with 2-PA in alkaline conditions, which might be true here also.[18] The peak observed at 494 cm^{-1} is assigned to Co-N bond vibration[20,21] (**Figure A4.2**, **Appendix**). Raman Peaks observed at 644, 897, 1025, 1269 and 1512 cm^{-1} are assigned to symmetric stretching of cobalt-oxygen bond, stretching of peroxo, symmetric trigonal ring breathing mode, bending of CH_2, and in plane vibration, respectively.[20,22,23] Thus a peroxo complex of Co(III) and 2-PA was probably formed in the medium. The strong absorption of the bridged complex was possibly due to the charge transfer from peroxo group to the Co(III) center. Literature reports also suggest the existence of similar charge transfer band for peroxo bridged complexes.[24,25] The plot of the intensity of Raman signal of the peroxide peak (897 cm^{-1}) with time was sigmoidal as shown in **Figure 4.1C**. Thus, the complexation reaction might have been followed by polymerization reaction. The rate of reaction was calculated to be 7.2 conc.min^{-1} (For the unit of rate of reaction and calculation refer **Appendix**).

Importantly, Raman peaks for the product, when using 532 and 784.5 nm excitations, were weak; however, at 632.8 nm, strong signal could be observed (**Figure 4.1D**). Since 632.8 nm laser excitation wavelength is close to absorption maximum of the product i.e., 595 nm, the resonance condition might have been achieved. Thus, the enhanced signal observed for the product may be attributed to resonance Raman scattering. The vibrational modes at 644 cm^{-1} (symmetric stretching of cobalt-oxygen bond) and 897 cm^{-1} (stretching of peroxo) were enhanced in the presence of the charge transfer between peroxo group and the Co(III) center. A 632.8 nm laser excitation induced such a charge transfer and the charge separation generated local electric field that influenced the vibrational modes as reflected in the Raman spectra.[26] Since pyridine ring in the polymer species was spatially proximal to charge transfer groups, the intensity of the vibrational modes associated with the ring (1025 and 1512 cm^{-1}) and bending of CH_2 (1269 cm^{-1}) could be augmented because of the change in polarizability caused by the local electric field.[26] As a result, vibrational modes positioned at 644, 897, 1025, 1269 and 1512 cm^{-1} were found with intensity comparable to the RR spectrum under 632.8 nm laser excitation as shown in **Figure 4.1B**.

TH-2949_166122105

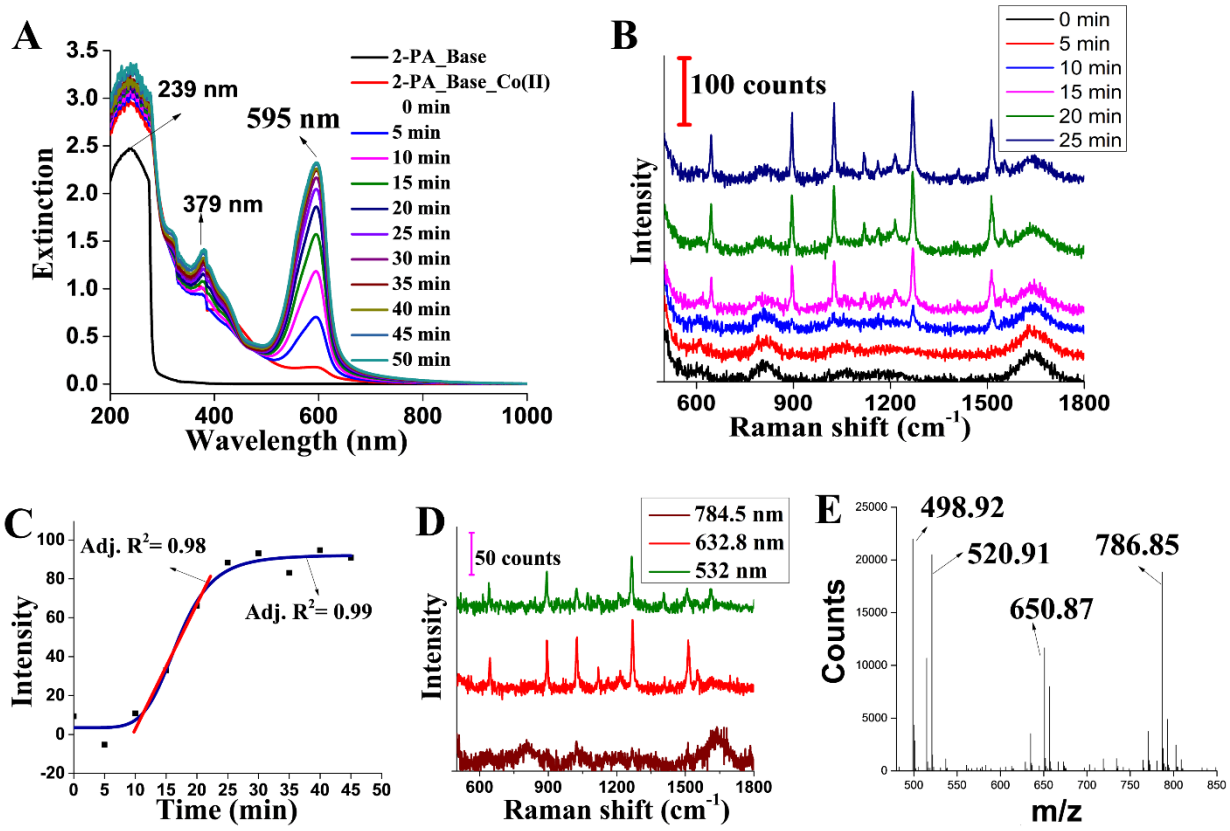

Figure 4.1. Time dependent (**A**) UV-Vis spectra and (**B**) Raman spectra of the formation of complex product in aqueous alkaline medium. (**C**) Sigmoidal kinetic profile for the formation of product. Rate was calculated with respect to the peroxide peak at 897 cm^{-1}. (**D**) Raman signal of the product measured at 532, 632.8 and 784.5 nm laser excitations. **(E)** Electrospray mass spectrum of the as-synthesized polynuclear complex.

Electrospray ionization mass (ESI-Mass) spectrum, as shown in **Figure 4.1E**, substantiated the formation of the polynuclear product. The major peaks at m/z = 498.92, 520.91, 650.87 and 786.85 in the ESI-mass spectrum are assigned to the fragments of polynuclear species, which appeared as $[C_{12}N_4H_{16}Co_2O_6Na_3]^{\bullet-}$, $[C_{12}N_4H_{15}Co_2O_6Na_4]^{\bullet-}$, $[C_{12}N_4H_{15}Co_3O_9Na_5]^{\bullet-}$ and $[C_{18}N_6H_{29}Co_4O_{11}Na_2]^{\bullet-}$. Overlay of the calculated and experimental mass spectra of these fragments (**Figure A4.3**, **Appendix**) revealed that the measured masses are consistent with the formation of a bridged polynuclear structure, of a Co-peroxo complex involving 2-PA. In addition, EDS mapping of the product polymer

TH-2949_166122105

(presented in **Figure A4.4A**, **Appendix**) showed large abundance of oxygen as compared to nitrogen (represents 2-PA), which supported oxygen enriched structure of the complex species. Crystallization of the product could not be achieved – possibly due to the formation of polynuclear species. Peak positions of protons in 2-PA were significantly shifted when the ligand (2-PA) participated in complexation reaction as shown in **Figure A4.5**. For example, the characteristic peak position of methylene proton (-CH_2-) of 2-PA appeared at 3.64 ppm (s) but it was shifted to 1.68 ppm (s) in the complex.[27] On the other hand, the peaks for ring protons of 2-PA occurring at 7.09, 7.21, 7.62 and 8.21 ppm were broadened and split due to the close proximity of cobalt.[28] Such observations regarding peak positions support the formation of complex as proposed above (**Figure A4.5, Appendix**). Thus, ^{1}H NMR data further supported the formation of the complex in the medium.

Typically, for a chelate compound, 2-PA or similar ligands are proposed to bind through both the nitrogen (pyridine-N as well as aminomethyl-N). However, one cannot fully discard the possibility of bonding through single nitrogen of the molecule. Mass spectrometric results – as discussed above – did not help resolve the issue fully. One way of addressing the question could be to carry out the reaction on the surface of plasmonic nanoparticles (such as those of Au) and probe the product using SERS. This was pursued by first incorporating the ligand (2-PA) on the surface of Au nanoparticles. UV-Vis spectrum of the as-synthesized Au nanoparticles consisted of a maximum at 524 nm (**Figure A4.6A**, **Appendix**). The TEM image of the nanoparticles shown in **Figure A4.6B** (**Appendix**) indicated formation of uniform spherical particles with the average particle diameter 28.4±1.6 nm **(Figure A4.6C**, **Appendix**).

When Au nanoparticles were treated with 2-PA (16.8 µM), there was a reduction in the absorbance at 524 nm and an appearance of a second peak at around 612 nm in the UV-Vis spectrum (**Figure A4.7A**, **Appendix**). The results indicated binding of 2-PA molecule to Au nanoparticle surface possibly through its pyridine-N site,[29] leaving the NH_2 group free for forming hydrogen bond with 2-PA molecule of another Au nanoparticle. As a result, there might have been formation of assembled Au nanoparticles in the dispersion medium resulting in the second (612 nm) peak. With increase in concentration of 2-PA, the assembled

TH-2949_166122105

structures of Au nanoparticles might have become larger and the second peak was consequently red shifted to 658 nm (**Figure A4.7A**, **Appendix**). The change in the position of the first peak (from 524 nm to 534 nm) might indicate bonding with 2-PA and thus altering the dielectric constant of the outer stabilizing layer of the nanoparticles. Further, TEM images as in **Figure A4.8** (**Appendix**) clearly showed the formation of Au nanoparticle assembled structure. Additionally, the absorbance due to the second peak (at 612 - 658 nm) in the UV-Vis spectrum (**Figure A4.7A**, **Appendix**) was directly proportional to the fraction of Au nanoparticle surface occupied (Ɵ) by 2-PA molecules. The reciprocal plot of surface area coverage versus concentration of 2-PA - with a linear fit – as in **Figure A4.7B** (**Appendix**) demonstrated that the 2-PA molecules on the surface of Au nanoparticles followed Langmuir adsorption isotherm.

Next when 2-PA (8.3 mM) attached Au nanoparticles were treated with Co(II) in the presence of base (pH 11), the reaction mixture immediately turned into yellow (**Figure A4.1B**, **Appendix**) with the appearance of peak at 379 nm in the UV-Vis spectrum as shown in **Figure 4.2A**. Then the reaction mixture slowly turned blue with the arrival of a peak at 594 nm (**Figure 4.2A**). Time-dependent UV-Vis study (**Figure 4.2A**) evidenced that the peak at 594 nm increased with time (and then dominated the peak at 379 nm), indicating the formation of the product similar to the one produced in absence of Au nanoparticles. The broad peak at 750 nm (**Figure 4.2A**) signified the assembled structures of Au nanoparticles. It is evident from the TEM image - as shown in **Figure 4.2B** - that Au nanoparticles were trapped into polymer-like amorphous product (**Figure A4.9**, **Appendix**), which might have been possible through the interaction between pyridine-N and Au nanoparticle surface.[30,31] When the complexation reaction (i.e., reaction between 2-PA and Co(II) in basic media) was carried out in the presence of Au nanoparticles (of 196 pM concentration), the time-dependent Raman signals improved significantly as shown in **Figure 4.2C**.

TH-2949_166122105

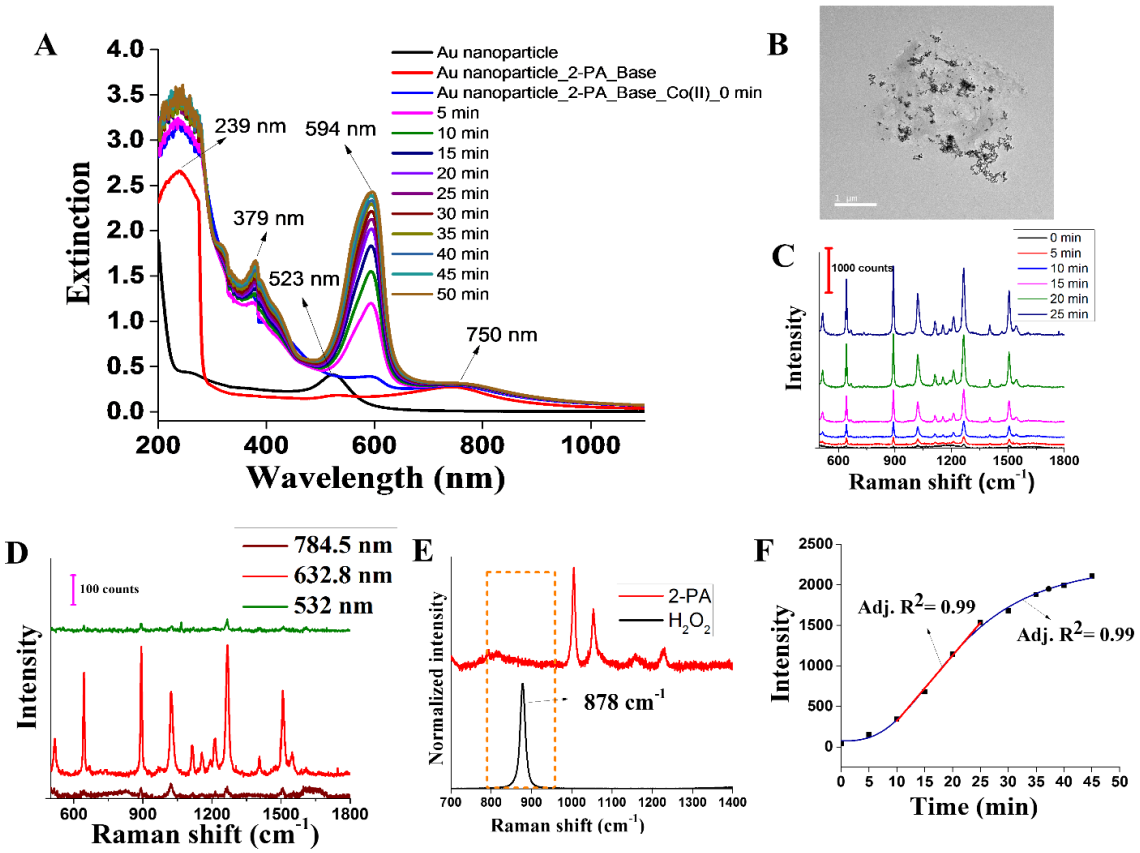

Figure 4.2. (**A**) Time-dependent UV-Vis spectra of the formation of complex product in presence of Au nanoparticles. The concentration of Au nanoparticle was 196 pM. (**B**) TEM images of Au nanoparticles trapped into polymer-like amorphous structure. (**C**) Time-dependent Raman spectra of the formation of product in presence 196 pM Au nanoparticle. (**D**) Raman signals of the product formed in the presence of Au nanoparticles and measured at 532, 632.8 and 784.5 nm laser excitations. (**E**) Raman spectrum of H_2O_2 (50%) and that of 4.85 M 2-PA ligand (in absence and presence of base) in presence of Au nanoparticles. (**F**) Sigmoidal kinetic profile for the formation of product on the basis of peroxide peak at 894 cm^{-1}.

The enhancement could be due to the attainment of SERRS condition (**Figure 4.2D**) at 632.8 nm laser excitation (as compared to 532 and 784.5 nm), which was supported by the observation of distinct peak of the product at 594 nm. In other words, the peak due to the complex at 594 nm and the broad peak due to assembled Au nanoparticles at 750 nm

TH-2949_166122105

provided the best conditions to observe SERRS at 632.8 nm excitation. The peak observed at 254 cm^{-1} in the SERRS spectrum, as shown in **Figure A4.2** (**Appendix**), substantiated the bonding between pyridine-N and Au nanoparticles.[32] The peak assigned to Co-N bond was shifted to 516 cm^{-1} (**Figure A4.2**, **Appendix**) due to the presence of Au nanoparticles.[30] The peaks assigned to symmetric stretching of cobalt-oxygen bond, stretching of peroxo, symmetric trigonal ring breathing mode, bending of CH_2, and in plane vibration were shifted to 641, 894, 1020, 1265 and 1506 cm^{-1}, respectively.[20,22,23] Similar observations were made at three other concentrations (24.5 pM, 49 pM and 98 pM) of Au nanoparticles (**Figure A4.10**, **Appendix**). Importantly, literature reports suggest the generation of peroxide through the reduction of dissolved oxygen accompanied by the oxidation of Co(II) into Co(III).[33-35] The Raman spectrum of H_2O_2 (50%) consisted of a peroxo peak at 878 cm^{-1} (**Figure 4.2E**). On the other hand, the spectrum due to the ligand (2-PA) recorded in the presence of Au nanoparticles - did not exhibit such a peak in the region between 800 to 1000 cm^{-1} (**Figure 4.2E**). Thus, peak appearing at 897 cm^{-1} from the reaction mixture may be considered to be due to the peroxo group in the cobalt complex.

At the surface of Au nanoparticles, the polymerization reaction still followed sigmoidal kinetic profile as shown in **Figure 4.2F** (and **Figure A4.10**, **Appendix**). The reaction rate came to be faster (11.2, 30.6, 56.3 and 94.7 conc.min^{-1}), and linearly dependent on concentration, in the presence of 24.5, 49, 98 and 196 pM Au nanoparticles, respectively (**Figure 4.3A**), evidencing catalytic polymerization. SERRS signal of the product formed in the presence of nanoparticles was significantly high and thus the main contribution was possibly from the complex (polymer) bonded to the nanoparticles while the UV-Vis signals would be from both catalyzed and uncatalyzed products formed in the reaction mixture. The observations also indicated that the 2-PA molecule – in the complex that was the unit of the polymer - might have been attached to Au surface through pyridine-N whereas aminomethyl-N participated in complexation. It is therefore plausible that 2-PA molecule acted as monodentate ligand in this complexation reaction that is different from the reported literature,[10,14,15,18] suggesting the flexidentate nature of the ligand. Based on the results, we

TH-2949_166122105

propose the formation of a bridged peroxo complex of Co(III) and 2-PA that polymerized upon formation (**Scheme 4.1**).[18, 33-35]

Under basic condition, NH_2 group of 2-PA (pK_1: 2.31(+2); pK_2: 8.79(+1) at 25 °C) could have undergone deprotonation and formed bridging complex with two Co(II) ions. The dissolved oxygen might have been reduced to peroxo with the concurrent oxidation of Co(II) into Co(III).[33-35] Thus a bridged peroxo complex was formed. Any binuclear species, which

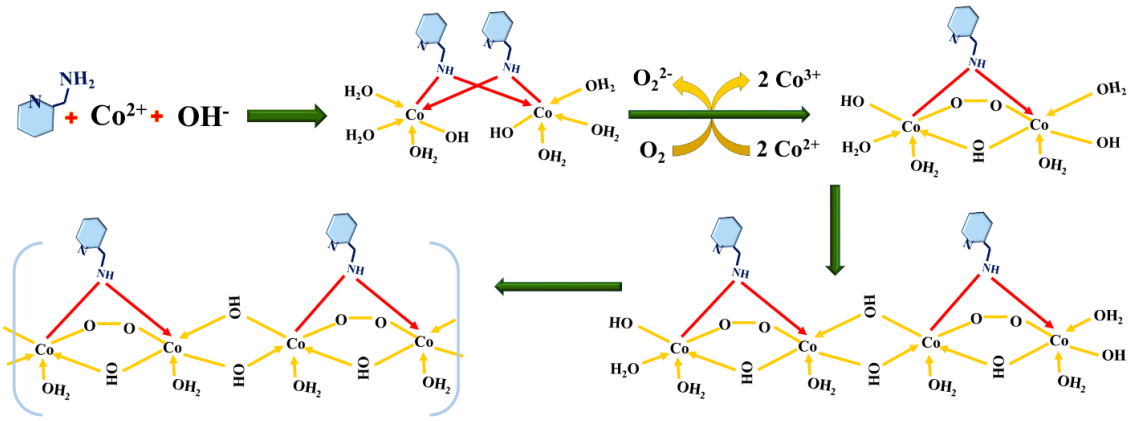

Scheme 4.1. Plausible mechanism of the formation of bridged polynuclear complex of cobalt and 2-PA under alkaline condition that is applicable for reactions both in the presence and absence of Au nanoparticles.

did form initially could instantaneously bridge to additional cobalt ion leading to polymerization.[18] The blue color (with absorption at 595 nm) is attributed to the formation of polynuclear species where each cobalt center is linked to μ-peroxo, μ-hydroxo and μ-amido bridges. The proposed structure of the bridged complex is consistent with the results of UV-Vis spectroscopy, mass spectrometry and SERRS. The above proposed mechanism of polynuclear complex formation is also consistent with the same reaction catalyzed by Au nanoparticles.

Density functional theory (DFT) study revealed the binding mode of guanine on Au nanoparticle that resulted in shifting of valence band towards the Fermi level.[31] In the present case, N of pyridine ring might have donated its lone pair of electrons to the vacant orbital of Au (σ donation) and π-back donation might have occurred from polarized Au valence orbital to N pyridine-π* orbital, leading to the shift of valence band, which facilitated faster reaction

TH-2949_166122105

pathway.[31] From DFT computational results as presented in **Figure 4.3B**, the energy difference between the highest occupied molecular orbital (HOMO) and the lowest unoccupied molecular orbital (LUMO) of 2-PA molecule was calculated to be 512.7 kJ/mol. That was reduced to 157.4 kJ/mol when 2-PA molecule was attached on Au surface through the lone pair of pyridine N. Thus, in presence of Au nanoparticle surface, the significant decrease (69.3%) in HOMO-LUMO energy gap increased the reactivity of 2-PA molecules, which led to significantly higher rate of polymerization reaction.

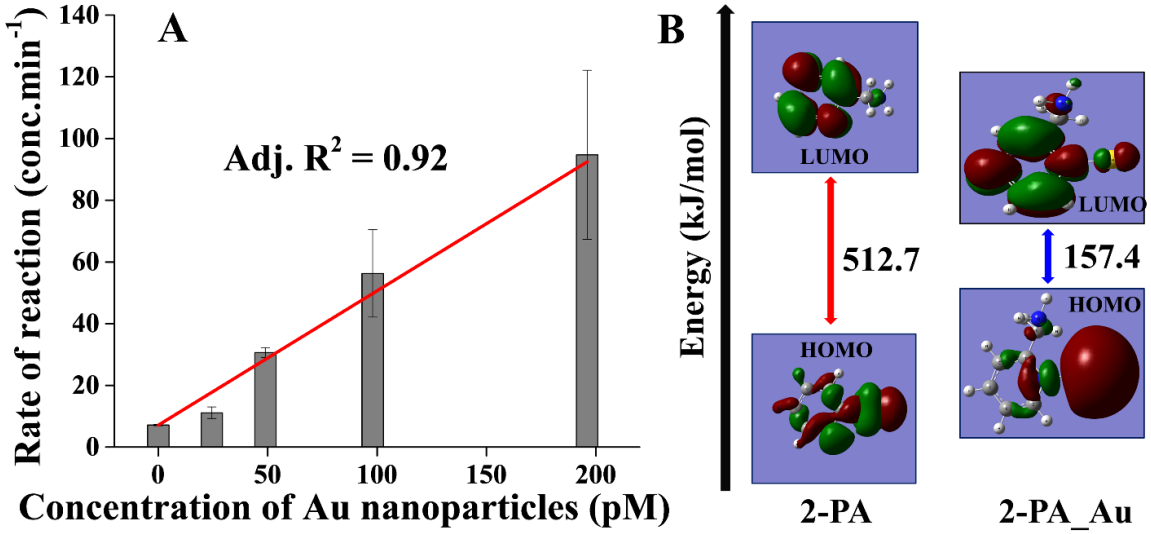

Figure 4.3. (**A**) Rate of the polynuclear complex formation reaction in the presence of different concentrations of Au nanoparticles. (**B**) HOMO-LUMO energy gap of 2-picolylamine and gold attached 2-picolylamine as calculated using density functional theory (DFT). DFT computations were done using functional B3LYP and basis set LanL2DZ on the optimized geometry. Gaussian-09 program was used for all the calculations and Gauss view 5 was used to create images.

It is important to mention here that since the product complex was a polymer, calculation involving multiple nanoparticles and the polymer being attached to them became a formidable challenge. However, considering the periodic nature of the structure of the polymer and the bonding between the nitrogen atoms and Au, we considered chemical interaction between one 2-PA molecule and one Au atom for simplicity. The results

TH-2949_166122105

indicated the change in reactivity of 2-PA molecule when bonded to the Au atom representing the nanoparticle. In that way, we concluded that the reduction of HOMO-LUMO energy gap of 2-PA molecule increased its reactivity and formed the complex product more rapidly in presence of Au nanoparticles.[31] Since Au nanoparticle was composed of large number of Au atoms, this calculation considering one Au atom and one 2-PA molecule represented a simplified version of the interaction between the polymer and the nanoparticle providing the possible reason for the higher product formation rate at the surface of Au nanoparticles

Another important point is that **Figure 4.2A** (which shows the UV-Vis absorption at 750 nm for the assembled Au nanoparticles in the presence of 2-PA) and **Figure A4.4B** (**Appendix**) (which shows TEM image along with EDS mapping for product polymer attached Au nanoparticles) indicated the presence and thus catalytic role of Au nanoparticle in the basic reaction condition.

4.4. Conclusions

In summary, literature reports[10,14,15,18] suggest that the reaction between Co(II) and 2-PA leads to the formation of a chelate complex. However, the current work – based on SERRS and mass spectrometric studies – revealed that in basic media Co(II) reacted with 2-PA to produce bridged polynuclear peroxo complex via sigmoidal kinetics, where 2-PA molecule acted as a monodentate ligand even in the presence of Au nanoparticles. The investigation of catalytic activity of Au nanoparticles on the rate of polynuclear product formation under in situ generated SERRS condition revealed that the rate of product formation was augmented significantly in presence of Au nanoparticles. The current work demonstrated not only polynuclear complexation reaction but also the same catalyzed by the nanoparticles and thus is promising for pursuing other complexation reactions on the surface of nanoparticles.

4.5. References

1. Kneipp, K.; Kneipp, H.; Itzkan, I.; Dasari, R. R.; Feld, M. S. *Chem. Rev.* **1999**, *99*, 2957.

TH-2949_166122105

2. Fateixa, S.; Nogueira, H. I. S.; Trindade, T. *Phys. Chem. Chem. Phys*. **2015**, *17*, 21046-21071.

3. Harper, M. M.; McKeating, K. S.; Faulds, K. *Phys. Chem. Chem. Phys.* **2013**, *15*, 5312-5328.

4. Langer, J.; Aberasturi, D. J.; Aizpurua, J.; Alvarez-Puebla, R. A.; Auguié, B.; Baumberg, J. J.; Bazan, G. C.; Bell, S. E. J.; Boisen, A.; Brolo, A. G.; Choo, J.; Cialla-May, D.; Deckert, V.; Fabris, L.; Faulds, K.; Abajo, F. J. G.; Goodacre, R.; Graham, D.; Haes, A. J.; Haynes, C. L.; Huck, C.; Itoh, T.; Käll, M.; Kneipp, J.; Kotov, N. A.; Kuang, H.; Ru, E. C. L.; Lee, H. K.; Li, J. F.; Ling, X. Y.; Maier, S. A.; Mayerhöfer, T.; Moskovits, M.; Murakoshi, K.; Nam, J. M.; Nie, S.; Ozaki, Y.; Pastoriza-Santos, I.; Perez-Juste, J.; Popp, J.; Pucci, A.; Reich, S.; Ren, B.; Schatz, G. C.; Shegai, T.; Schlücker, S.; Tay, L. L.; Thomas, K. G.; Tian, Z. Q.; Van Duyne, R. P.; Vo-Dinh, T.; Wang, Y.; Willets, K. A.; Xu, C.; Xu, H.; Xu, Y.; Yamamoto, Y. S.; Zhao, B.; Liz-Marzán, L. M. *ACS Nano*, **2020**, *14*, 28.

5. McLintock, A.; Lee, H. J.; Wark, A. W. *Phys. Chem. Chem. Phys*. **2013**, *15*, 18835-18843.

6. Sengupta, K.; Chatterjee, S.; Dey, A. *ACS Catal.* **2016**, *6*, 6838.

7. Faulds, K.; Littleford, R. E.; Graham, D.; Dent, G.; Smith, W. E. *Anal. Chem.* **2004**, *76*, 592.

8. Eng, L. H.; Schlegel, V.; Wang, D.; Neujahr, H. Y.; Stankovich, M. T.; Cotton, T. *Langmuir* **1996**, *12*, 3055.

9. Alexander, B. D.; Crayston, J. A.; Dines, T. J. *Phys. Chem. Chem. Phys*. **2004**, *6*, 3576-3584.

10. Fu, H. J.; Chen, Q. Y.; Huang, J.; Zhang, R. X. *Transition Met. Chem.* **2010**, *35*, 103.

11. Maiti, D.; Sarjeant, A. A. N.; Karlin, K. D. *Inorg. Chem.* **2008**, *47*, 8736.

12. Hambley, T. W. *Dalton Trans.* **2007**, 4929.

13. Kadhiravansivasamy, K.; Sivajiganesan, S.; Periyathambi, T.; Nandhakumar, V.; Chidhambram, S.; Manimekalai, R. *Mod. Chem. appl.* **2017**, *5*, 1000197.

14. Santos, N. A. C.; Natali, M.; Badetti, E.; Wurst, K.; Licini, G.; Zonta, C. *Dalton Trans.* **2017**, *46*, 16455.

TH-2949_166122105

15. Call, A.; Casadevall, C.; Romero-Rivera, A.; Martin-Diaconescu, V.; Sommer, D. J.; Osuna, S.; Ghirlanda, G.; Lloret-Fillol, J. *ACS Catal.* **2019**, *9*, 5837.

16. Patai, S. *The Chemistry of Functional Groups, Peroxides*, John Wiley & Sons Ltd, **1983**.

17. Conte, V.; Furia , F. D.; Modena, G. Chap. 11.2. in *Organic Peroxides*, ed. W. Ando, Wiley, Chichester **1992**, pp. 559–598.

18. Huchital, D. H.; Debesis, E. *Inorganica Chimica Acta* **1987**, *126*, 167.

19. Jiménez, I. O.; Romero, F. M.; Bastús, N. G.; Puntes, V. *J. Phys. Chem. C* **2010**, *114*, 1800.

20. T. Shibahara, T.; Mori, M. *Bulletin of the Chemical Society of Japan* **1978**, *51*, 1374.

21. Freedman, T. B.; Yoshida, C. M.; Loehr, T. M. *J. Chem. Soc., Chem. Comm.* **1974**, 1016.

22. Vacque, V.; Sombret, B.; Huvenne, J. P.; Legrand, P.; Suc, S. *Spectrochimica Acta Part A* **1997**, *53*, 55.

23. Mühlig, A.; Cialla-May, D.; Popp, J. *J. Phys. Chem. C* **2017**, *121*, 2323.

24. Huchital, D. H.; Debesis, E. *Inorganica Chimica Acta* **1985**, *98*, 79.

25. Vogler, A.; Kunkely, H. *Coordination Chemistry Reviews* **2006**, *250*, 1622.

26. Davari, N.; Haghdani, S.; Astrand, P. O.; Schatz, G. C. *RSC Adv.* **2015**, *5*, 31594.

27. Roy, S.; Bhandari, S.; Manna, M.; De, S.; Chattopadhyay, A. *Phys. Chem. Chem. Phys.* **2019**, *21*, 589-596.

28. Santos, T. M.; Goodfellow, B. J.; Madureira, J.; Jesus, J. P.; Felix, V.; Drew, M. G. B. *New J. Chem*. **1999**, *23*, 1015-1025.

29. Moon, S. W.; Ha, J. W. *Analyst* **2019**, *144*, 2679.

30. Han, D.; Li, C.; Chen, H. *Spectroscopy Letters* **1998**, *31*, 1263.

31. Zhang, X.; Sun, C. Q.; Hirao, H. *Phys. Chem. Chem. Phys.* **2013**, *15*, 19284.

32. Juhlin, L.; Mikaelsson, T.; Hakonen, A.; Schmidt, M. S.; Rindzevicius, T.; Boisen, A.; Käll, M.; Andersson, P. O. *Talanta* **2020**, *211*, 120721.

33. Carter, D. E. *Environmental Health Perspectives* **1995**, *103*, 17.

34. Goodman, G. L.; Hecht, H. G.; Weil, J. A. *Advances in Chemistry* **1962**, *8*, 90.

35. Wu, J.; Mehmood, A.; Zhang, G.; Wu, S.; Ali, G.; Kucernak, A. *ACS Catal.* **2021**, *11*, 5035.

TH-2949_166122105

Appendix of Chapter 4: A4

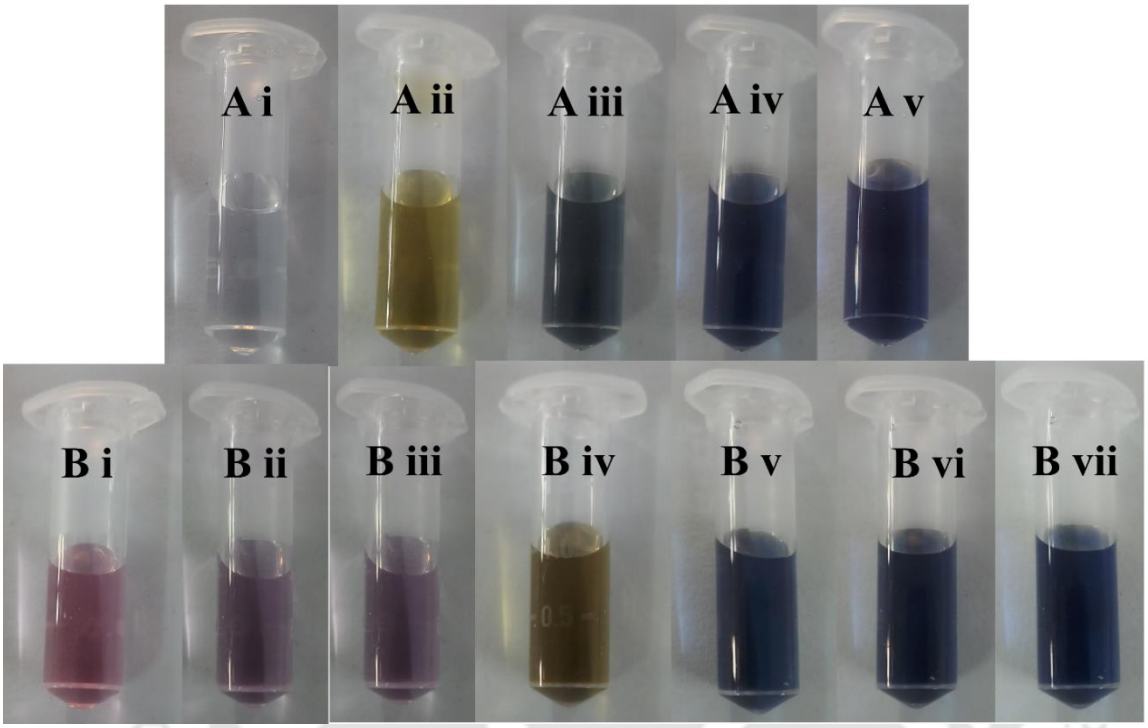

Figure A4.1. Digital photographs of (**A**) mixture of 2-PA and NaOH in H_2O (**i**); mixture of 2-PA, NaOH and Co(II) in H_2O (without Au nanoparticles) at 0 min (**ii**), 5 min (**iii**), 10 min (**iv**) and 15 min (**v**). (**B**) Photographs of Au nanoparticle dispersion (**i**), 2-PA added Au nanoparticle dispersion (**ii**), mixture of 2-PA and NaOH in Au nanoparticle dispersion (**iii**) and mixture of 2-PA, NaOH and Co(II) in Au nanoparticle dispersion at 0 min (**iv**), 5 min (**v**), 10 min (**vi**) and 15 min (**vii**).

TH-2949_166122105

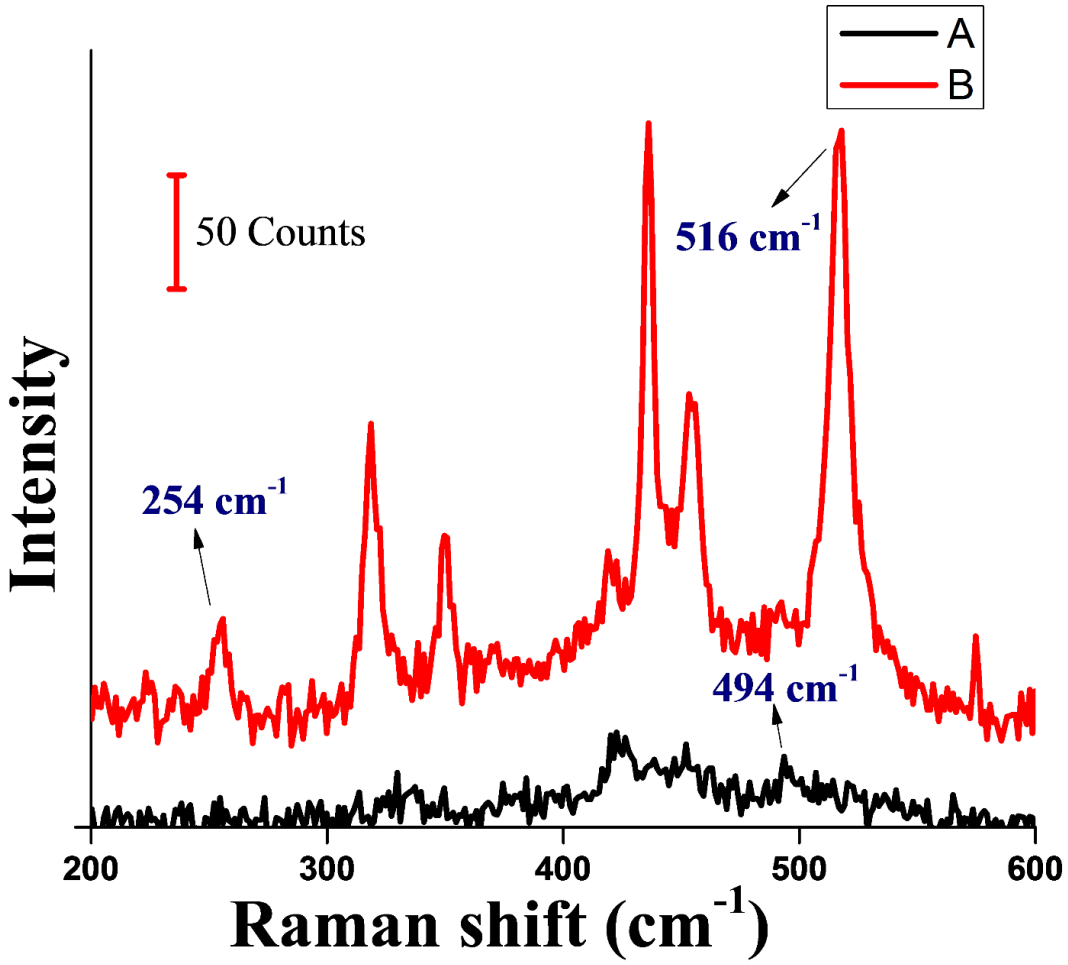

Figure A4.2. Raman spectra of polynuclear complex (product) (**A**) in absence of Au nanoparticles and (**B**) in presence of Au nanoparticles (recorded with laser excitation wavelength of 632.8 nm).

TH-2949_166122105

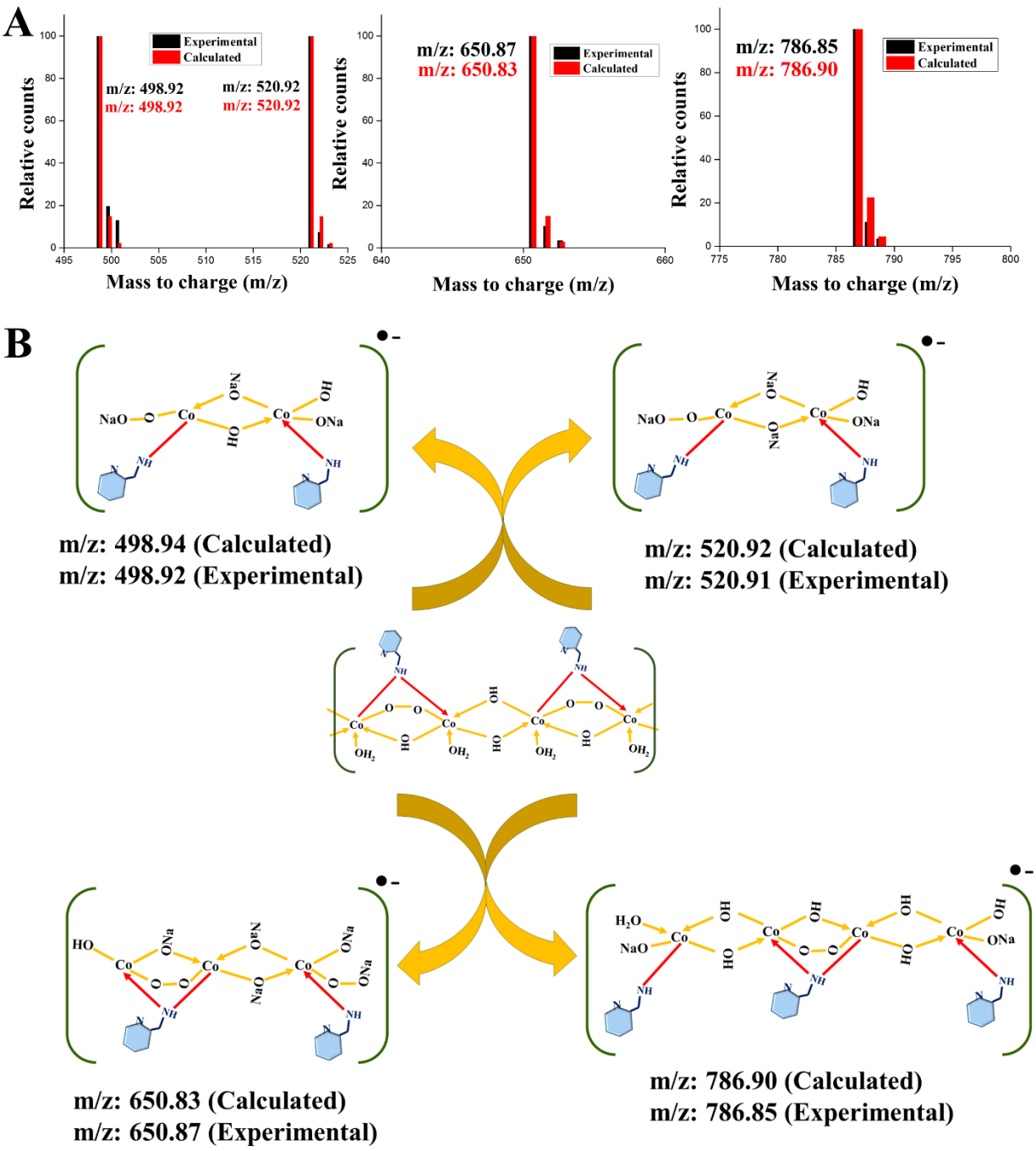

Figure A4.3. (**A**) Overlay of calculated and experimental mass spectra (major peaks) of as-synthesized polynuclear complex (product). (**B**) Possible fragmentations of as-synthesized bridged polynuclear complex as observed in the mass spectra.

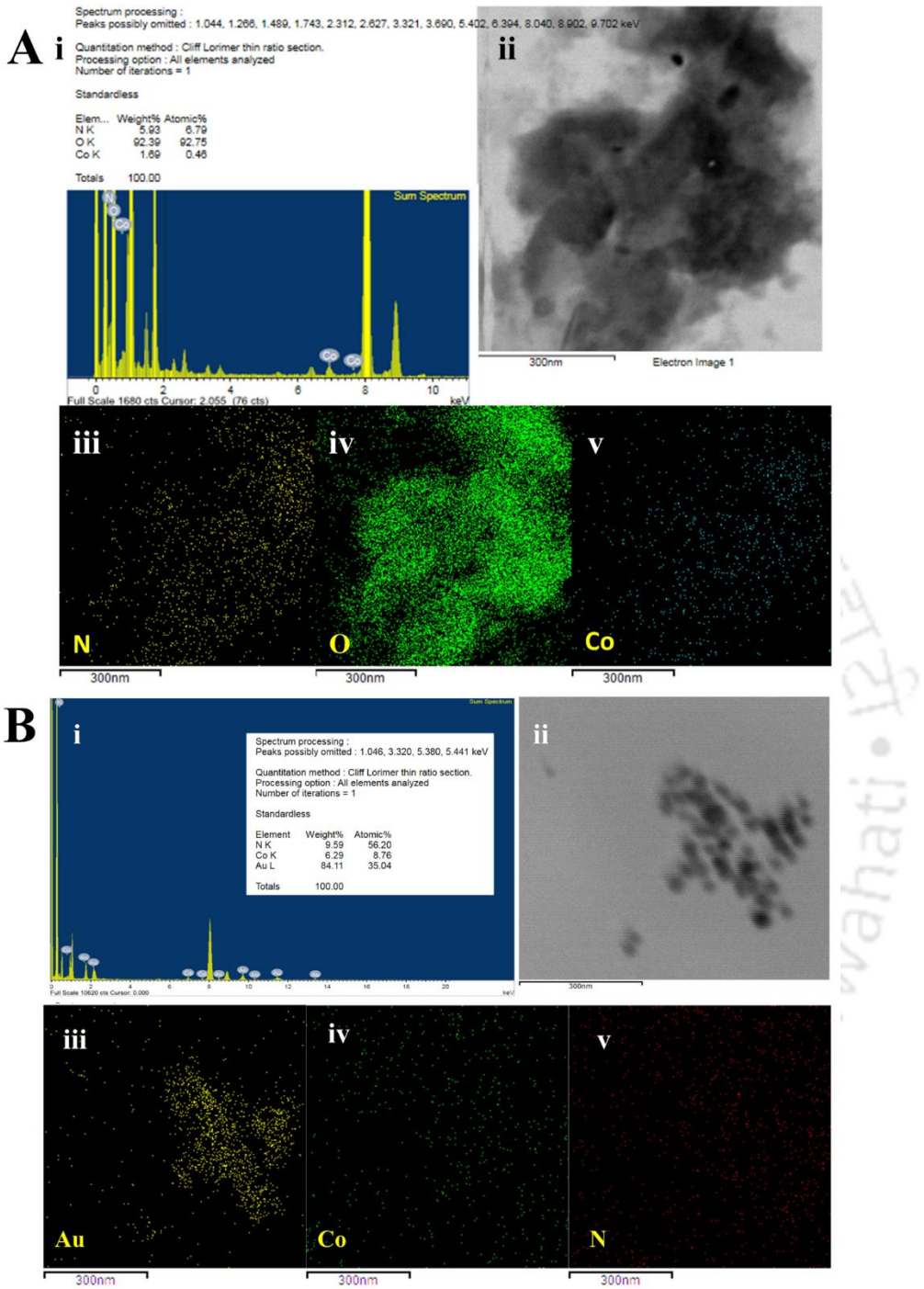

Figure A4.4. (**A**) EDS spectrum (**i**) and corresponding TEM image (**ii**) along with elemental mapping (**iii**, **iv** and **v** for N, O and Co, respectively) for product polymer only. (**B**) EDS spectrum (**i**) and corresponding TEM image (**ii**) along with elemental mapping (**iii**, **iv** and **v** for Au, Co and N, respectively) for product polymer attached Au nanoparticles.

TH-2949_166122105

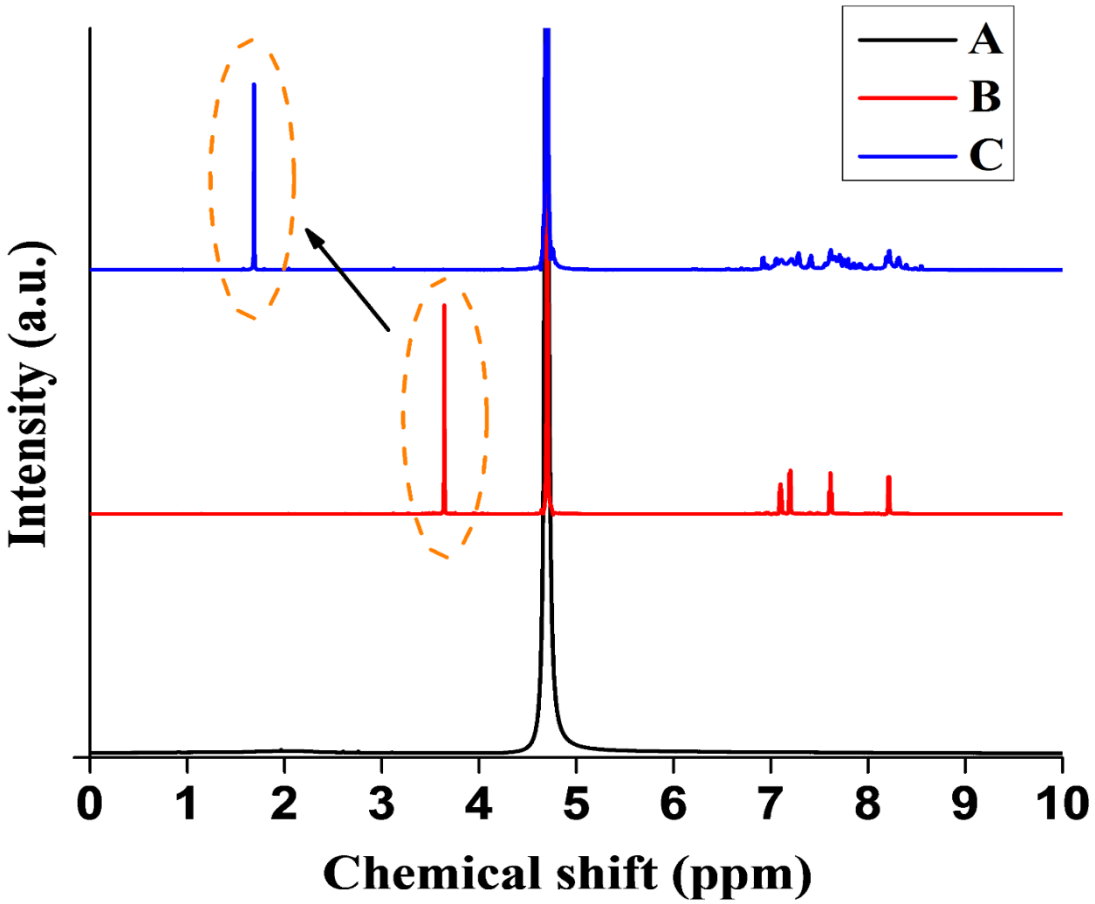

Figure A4.5. ^{1}H NMR spectra of cobalt acetate (**A**), 2-PA (**B**) and blue complex (**C**) in D_2O solvent. Measurements were done using 500 MHz NMR instrument.

TH-2949_166122105

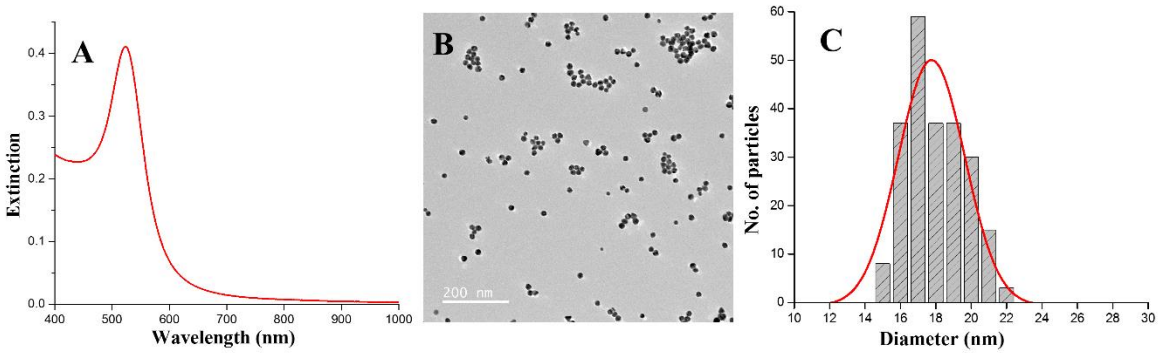

Figure A4.6. UV-Vis spectrum (**A**), TEM image, (**B**) and average particle size and (**C**) of as-synthesized citrate stabilized Au nanoparticles.

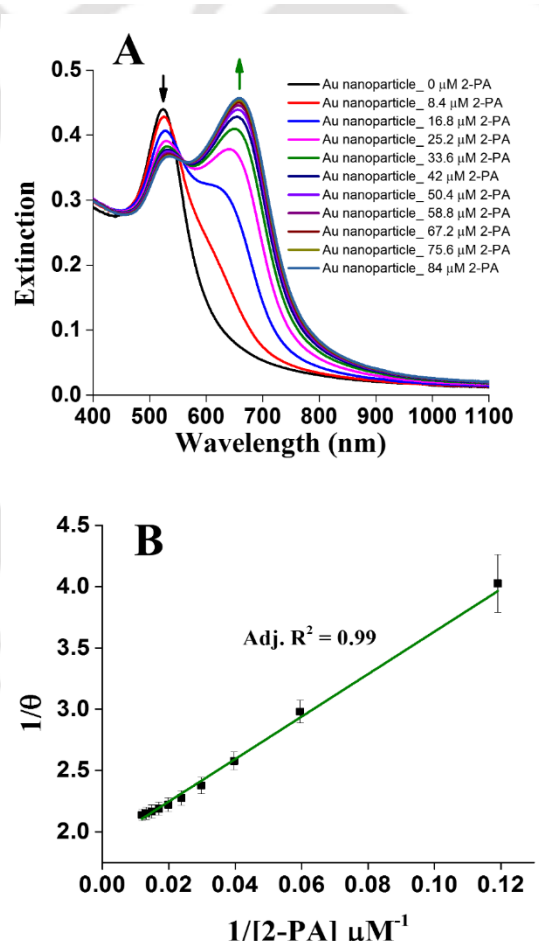

Figure A4.7. (**A**) UV-Vis spectra of the different concentrations of 2-PA added Au nanoparticles. (**B**) Reciprocal plot (of surface coverage (Θ) versus concentration of free 2-PA) of Langmuir adsorption isotherm with a linear fitting.

TH-2949_166122105

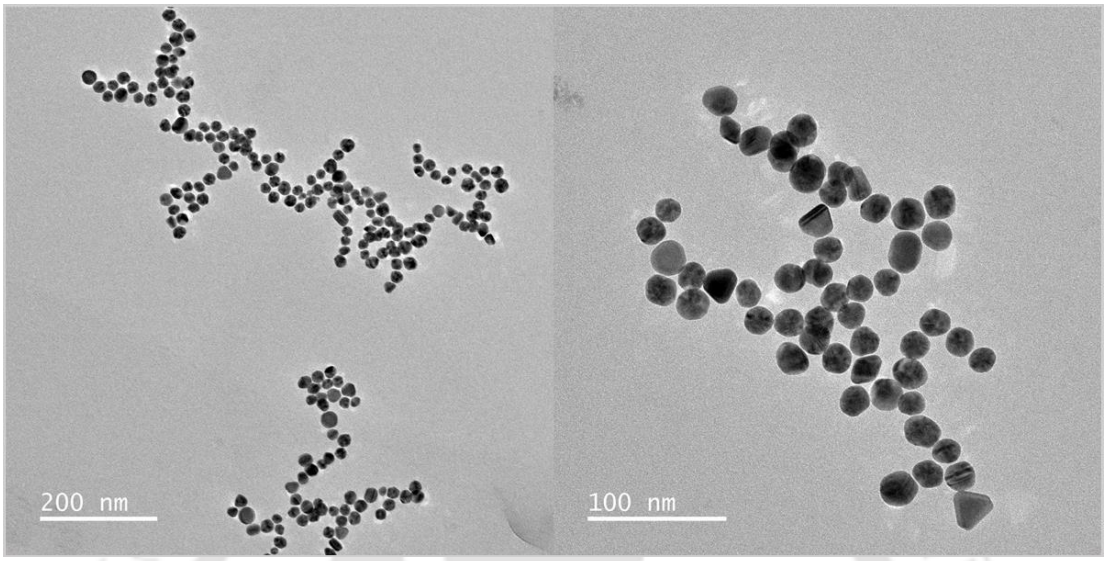

Figure A4.8. TEM image of 2-PA treated Au nanoparticles.

TH-2949_166122105

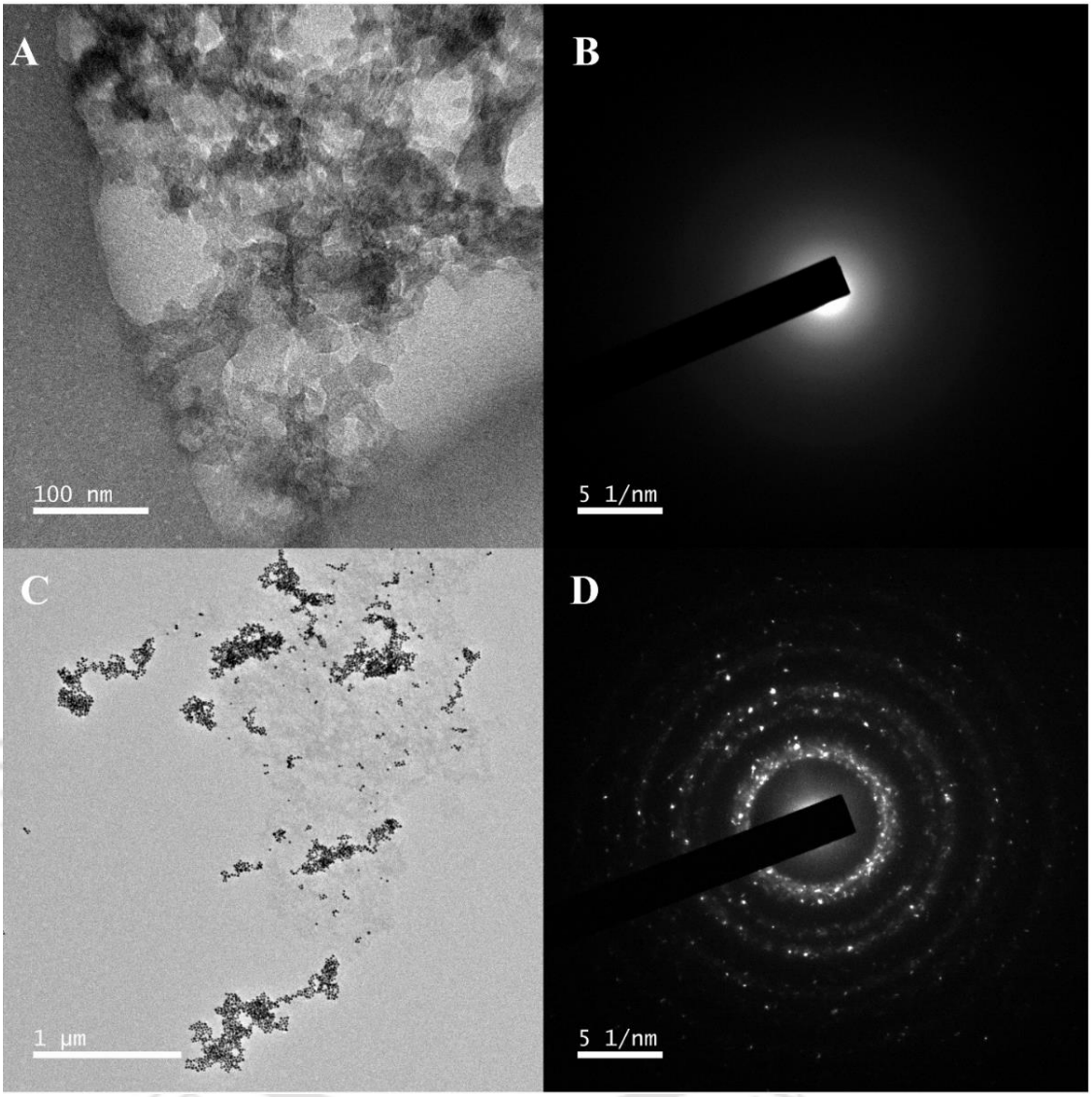

Figure A4.9. TEM image of polynuclear complex (product) synthesized in absence Au nanoparticles (**A**) and corresponding SAED pattern (**B**). TEM image of polynuclear complex (product) synthesized in presence Au nanoparticles (**C**) and corresponding SAED pattern (**D**).

TH-2949_166122105

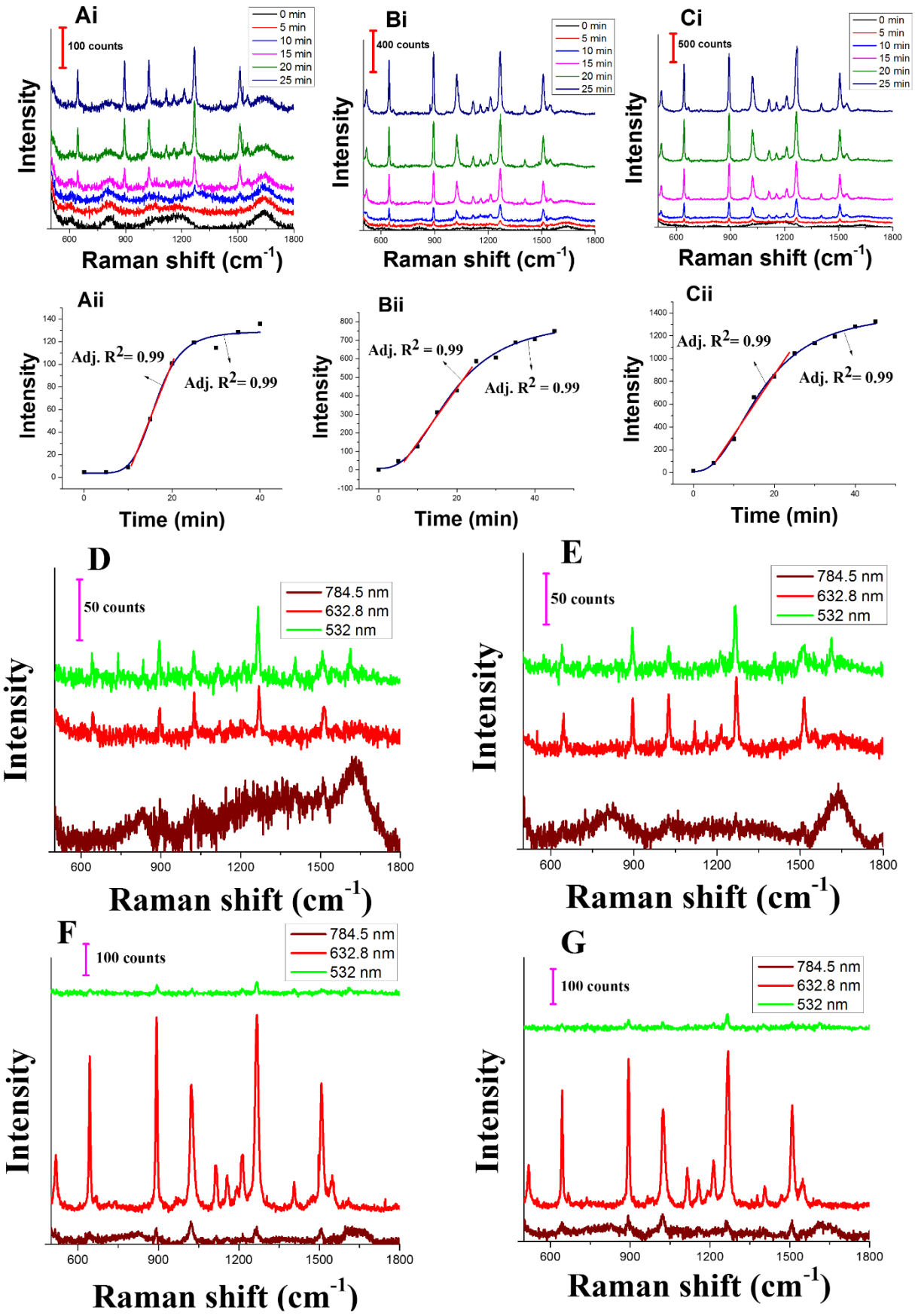
Ai
100 counts
0 min
5 min
10 min
15 min
20 min
25 min
Intensity
Raman shift (cm-1)
Bi
400 counts
Ci
500 counts
Aii
Adj. R2= 0.99
Time (min)
Bii
Cii
D
50 counts
784.5 nm
632.8 nm
532 nm
E
F
100 counts
G

Figure A4.10. Time dependent Raman spectra (measured at a laser power of 16 mW) of the polymerization reaction in presence 24.5 pM (**Ai**), 49 pM (**Bi**) and 98 pM (**Ci**) Au nanoparticles and their corresponding sigmoidal kinetic profiles (**Aii**, **Bii** and **Cii**, respectively). Raman signal of polynuclear complex (product) recorded at 532, 632.8 and 784.5 nm laser excitations (**D, E**) in absence of Au nanoparticles and (**F, G**) in presence of Au nanoparticles, respectively (Power of laser source was 3 mW).

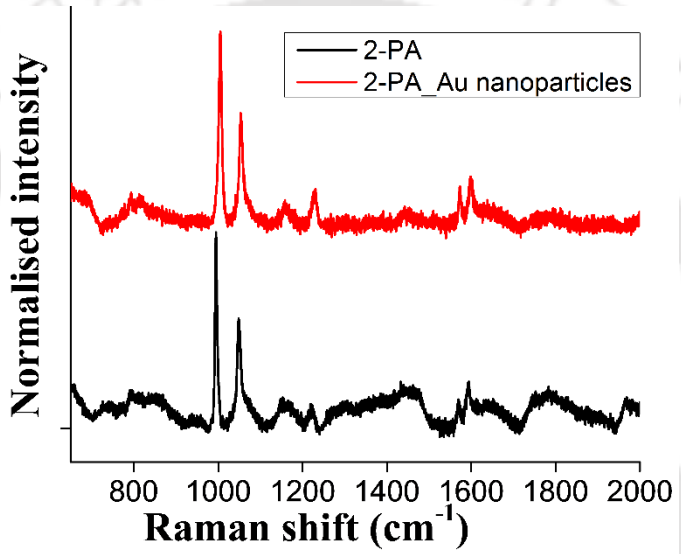

Figure A4.11. Raman spectra of 2-PA (4.85 M) only and 2-PA (2.43 M) in presence of Au nanoparticles (recorded at 632.8 nm laser excitations).

Description: In presence of Au nanoparticles 2-PA showed Raman intensity with improved signal to noise ratio.

TH-2949_166122105

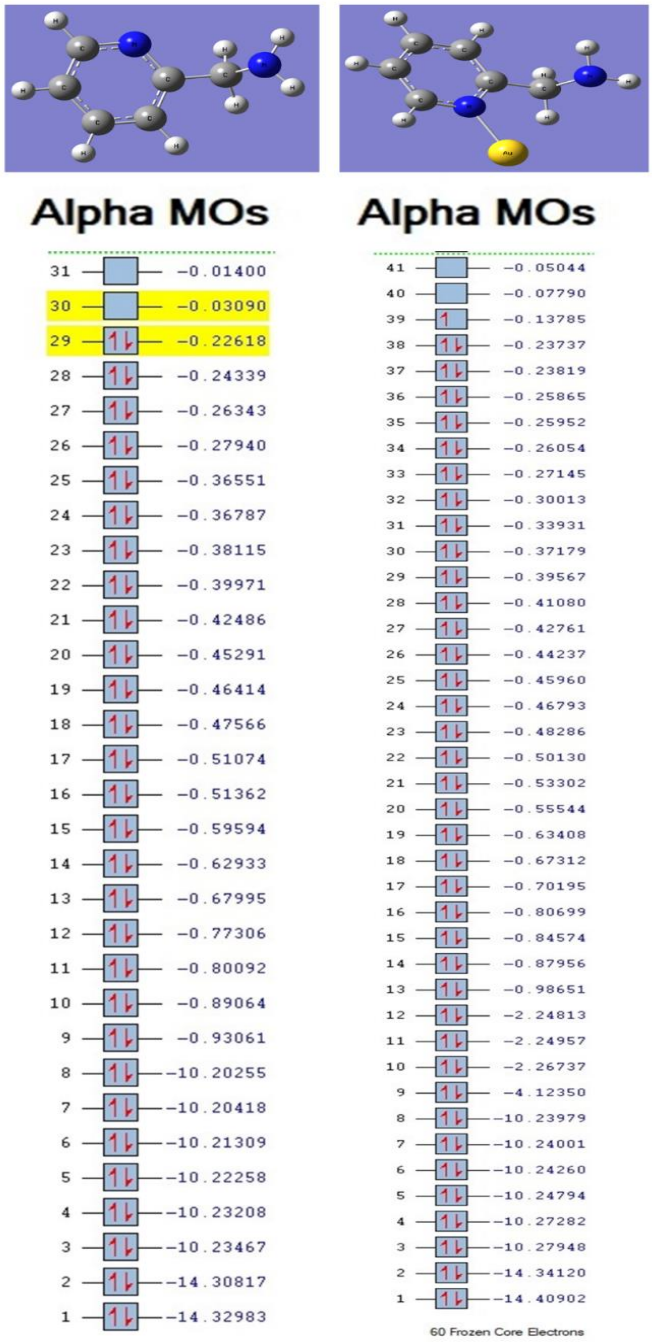

Figure A4.12. DFT computational results using functional B3LYP and basis set LanL2DZ for 2-picolylamine and gold attached 2-picolylamine.

TH-2949_166122105

Calculation of the concentration of citrate capped Au nanoparticles:

Concentration of stock $HAuCl_4$ solution = 29×10^{-3} M

Number of moles of $HAuCl_4$ in 0.123 mL $HAuCl_4$ stock solution = Number of moles of $HAuCl_4$ in reaction mixture = 3.56×10^{-6}

Assuming complete reaction, we can write $[HAuCl_4] = [Au]$

Total number of Au atoms in reaction mixture = $3.56\times10^{-6}\times N_A$

,where $N_A = 6.023\times10^{23}$ mol^{-1}

For FCC nanocrystal, packing fraction = 0.74

Average radius of one spherical Au nanoparticle = 9.2 nm as measured from FETEM.

Average radius of one Au atom = 0.144 nm

Number of Au atoms in one Au nanoparticle

= Packing fraction × (Volume of one Au nanoparticle)/(Volume of one Au atom)

= Packing fraction × (Average radius of Au nanoparticle)^3/(Average radius of Au atom)^3

= $0.74\times(9.2\text{ nm})^3/(0.144\text{ nm})^3$

= 1.93×10^5

Number of Au nanoparticles in the 25 mL reaction mixture

= (Total number of Au atoms in reaction mixture) / (Number of Au atoms in one Au nanoparticle)

= 1.11×10^{13}

Number of moles of Au nanoparticles in 25 mL reaction mixture = 1.84×10^{-11} mol

The Au nanoparticles were concentrated by two times through centrifugation.

TH-2949_166122105

Final concentration of Au nanoparticles = $\frac{1.84\times10^{-11}\times1000}{12.5}$ M

Final concentration of Au nanoparticles = 1.47×10^{-9} M = 1.47 nM = 1470 pM

Preparation of 5 different concentrations of Au nanoparticle dispersions:

1) 0 pM Au nanoparticle dispersion (total volume = 3 mL)

Volume of 1470 pM of Au nanoparticle dispersion required = 0 uL

2) 24.5 pM Au nanoparticle dispersion (total volume = 3 mL)

Volume of 1470 pM of Au nanoparticle dispersion required = 50 uL

3) 49 pM Au nanoparticle dispersion (total volume = 3 mL)

Volume of 1470 pM of Au nanoparticle dispersion required = 100 uL

4) 98 pM Au nanoparticle dispersion (total volume = 3 mL)

Volume of 1470 Pm of Au nanoparticle dispersion required = 200 uL

5) 196 pM Au nanoparticle dispersion (total volume = 3 mL)

Volume of 1470 pM of Au nanoparticle dispersion required = 400 uL

Reaction rate calculation:

In this current work, product formation followed sigmoidal kinetics, which was calculated on the basis of peroxide peak as formed in absence or presence of Au nanoparticles. For each sample the rate of reaction was calculated on the basis of maximum slope in their sigmoidal kinetic profiles.

In the complexation reaction, the concentrations of 2-PA, cobalt ion and base were fixed but the concentration of dissolved oxygen (one of the reactants) was indefinite for each reaction mixture. Thus, it was not possible to find out the order of reaction. In other words, it was not possible to find the absolute unit of rate of the reaction. Therefore, the unit of rate is referred to as conc.min^{-1}.

TH-2949_166122105

CHAPTER 5

Herein we report simultaneous quantitative detection of H_2O, D_2O and HOD in the same reaction mixture with the help of bridged polynuclear peroxo complex in absence and presence of Au nanoparticles on the basis of a peroxide vibrational mode in resonance Raman and surface-enhanced resonance Raman spectrum. We synthesize bridged polynuclear peroxo complex in different solvent mixture of H_2O and D_2O. Due to the formation of different nature of hydrogen bonding between peroxide and solvent molecules (H_2O, D_2O and HOD), vibrational frequency of peroxo bond is significantly affected. Mixtures of different H_2O and D_2O concentrations produce different HOD concentrations and that lead to different intensities of peaks positioned at 897, 823 and 867 cm^{-1} indicating H_2O, D_2O and HOD, respectively. The lowest detection limits (LODs) were 0.028 mole fraction of D_2O in H_2O and 0.046 mole faction of H_2O in D_2O. In addition, for the first time the results revealed that the cis-peroxide forms two hydrogen bonds with solvent molecules.

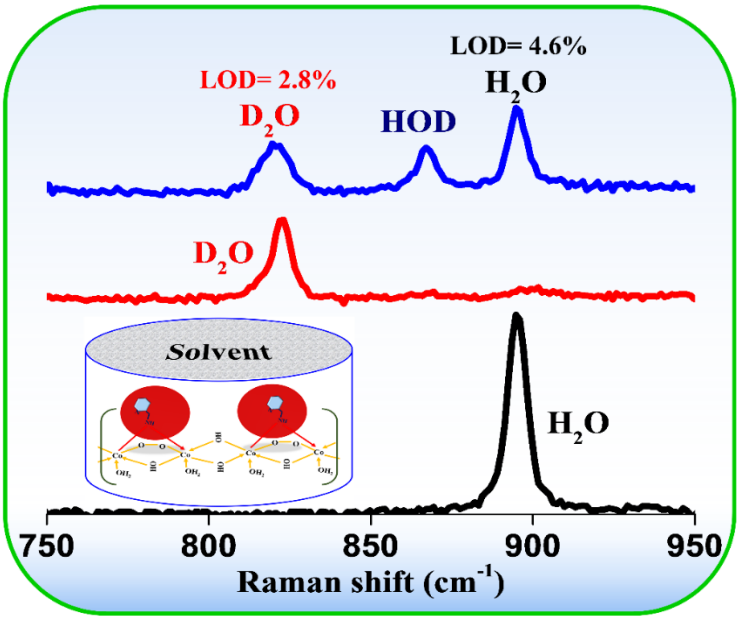

Ref.: Pal, S.; Chattopadhyay, A. Highly Efficient and Simultaneous Sensing of H_2O, D_2O and HOD through Peroxo Vibrations. [Communicated, 2022]

TH-2949_166122105

5.1. Introduction

An important scientific challenge that has drawn consistent special attention of spectroscopic and spectrometric probes is the knowledge of purity of heavy water (D_2O). This possibly stems from the fact that the availability of pure D_2O is key to several scientific and technological applications. For example, D_2O acts as a moderator for deceleration of neutron in nuclear reactor.[1-3] The molecule is also essential in neutrino detector.[4-6] D_2O is a suitable solvent for infrared (IR) and nuclear magnetic resonance (NMR) spectroscopy, which helps eliminate the band from H_2O that overlaps with the solute.[7-9] It is also used to preserve pancreas.[10] The purity of D_2O is essential for the abovementioned and other applications.[11] Thus, D_2O must be free from H_2O impurity. However, the determination of the level of purity is rather difficult as not only the size and shape of H_2O and D_2O molecules are the same but also spectroscopic differentiation especially when present as a mixture is problematic.[12]

There are several methods such as atomic absorption, NMR, FTIR and fluorescence spectroscopy to distinguish qualitatively D_2O from H_2O in a mixture.[13-19] Further, fluorescence sensors such as those from lanthanide complexes behave differently in H_2O and D_2O and thus could distinguish the two solvents.[20,21] Although mass spectrometry provides a viable option, however, here again (like other methods) identification of HOD in the mixture quantitatively is rather difficult due to overlapping spectra of the components.[22]

Moreover, there are challenges such as portability of instruments and time-consuming and involved nature of sample preparation and detection that impede point-of-need use of the above-mentioned methods. In addition, the fundamental challenge involving formation of HOD as a reaction between H_2O and D_2O needs to be taken into consideration for a meaningful resolution of the constituent molecules in the mixture. The methods that have been developed so far cannot address the issue of detection of HOD present in the mixture. The atomic mass distinction - especially when present in a reactive mixture - can possibly be made through the use of vibrational spectroscopy. In this regard, Raman spectroscopy may be considered as the most suitable method for identification of H_2O, D_2O and HOD in a mixture. However, conventional Raman spectrum of pure H_2O as well as D_2O has a broad characteristic peak associated with 5 different vibrations.[23-26] Along with this, the broadness

TH-2949_166122105

of the peak for H_2O is much higher compared to that of D_2O and Raman scattering of H_2O is significantly larger than D_2O.[23-26] Thus, it is rather challenging to quantitate H_2O and D_2O in different mixtures based on the Raman spectrum as such. In addition, distinction of HOD present in the mixture is not possible using the conventional Raman spectroscopy. This could be the reason for no literature report of simultaneous detection of H_2O, D_2O and HOD based on their Raman spectra.

On the other hand, vibrational spectroscopic probe of molecular bonds when involved in intermolecular interactions through hydrogen bonding could be an important source of differentiation of the isotopic contents of water. For example, vibrational frequencies of an aqueous inorganic complex that forms hydrogen bonds may change differently depending on the nature of the bonding species present in the medium, i.e., H_2O, D_2O or HOD. This could be the basis of distinction. It would be even more significant if the Raman scattering intensities of the probe frequencies (such as those of an inorganic complex) could be sufficiently increased in the presence of plasmonic nanoparticles such as those of Au or Ag. In addition, if the absorption maximum of the complex coincides with that of the laser frequency then a resonance condition can be achieved for obtaining highest amplification in the form of SERRS.

Herein we report simultaneous detection of mole fractions of H_2O, D_2O and HOD using resonance Raman (RR) and SERRS. This was pursued via the synthesis of a bridged polynuclear peroxo complex in the solvent mixture of H_2O and D_2O in absence and in the presence of Au nanoparticles. The absorption peak of the complex at 595 nm generated resonance Raman condition at the laser excitation wavelength of 632.8 nm.[27] We observed that the Raman peak of the peroxo bond was differently affected by the interaction with H_2O, D_2O or HOD as a result of hydrogen bonding. The results suggested that the Raman peak of the peroxo bond appeared at 897, 823 and 867 cm^{-1} in the presence of H_2O, D_2O and HOD, respectively. Mixtures of different H_2O and D_2O concentrations produced resulted in different intensities of the peaks, which facilitated the detection of H_2O, D_2O and HOD content. The LODs were 0.028 mole fraction of D_2O in H_2O and 0.046 mole faction of H_2O in D_2O. Interestingly, the results could be accounted for by considering the formation of cis-peroxide complex that formed two hydrogen bonds with the neighboring solvent molecules.

TH-2949_166122105

This is contrary to the well-known trans-peroxide that forms four hydrogen bonds[28] with the solvent molecules. To the best of our knowledge, this is the first report on the simultaneous detection of H_2O, D_2O and HOD content in a solvent, using RRS and SERRS that further shed light on the nature of hydrogen bonding of a cis-peroxo complex.

5.2. Experimental Section

5.2.1. Materials: Gold(III) chloride (30 wt. % in HCl), 2-PA, cobalt(II) acetate tetrahydrate, sodium hydroxide, trisodium citrate dihydrate, and heavy water were used for the experiments. All the mentioned chemicals were purchased from Sigma-Aldrich (India) and used in experiments without further purification. For various experimental works, Milli-Q (MQ) grade water was used.

5.2.2. Au nanoparticle synthesis: Citrate capped Au nanoparticles were synthesized following a reported method.[1] 54.4 mg of trisodium citrate was added into a double neck round bottom flask containing 100 mL MQ grade water and then the mixture was heated at 110 °C while stirring. After 1 h, 492 µL of 29 mM $HAuCl_4$ solution was added into the flask. After sometime, the color of the reaction mixture turned into red indicating the formation of Au nanoparticles. The reaction mixture was stirred for 30 min more. After that the red colored dispersion was cooled to room temperature and divided into two parts (50 mL each). Each part was centrifuged at 15,000 rpm for 10 min. The precipitate obtained after centrifugation of one part was dispersed into 25 ml MQ grade water and the precipitate collecting from other part was dispersed into 25 mL heavy water (D_2O). Both the dispersed Au nanoparticles stocks (one in H_2O and other one in D_2O) were stored at room temperature for further use.

5.2.3. Bridged polynuclear complex synthesis: 2-PA (0.5 M) solution was treated with sodium hydroxide (1M) followed by the addition of cobalt acetate (21 mM) solution. The quantity of each reactant is shown in **Table 5.1** and **Table 5.2**. After sometime the reaction mixture turned into blue, which indicated the formation of bridged polynuclear complex. Each synthesis of bridged polynuclear complex was carried out thrice with seven different concentrations of H_2O & D_2O solvent in absence and presence of Au nanoparticles (1.47 nM).

TH-2949_166122105

Table 5.1. Quantities of components in the synthesis of bridged polynuclear complex in absence of Au nanoparticles.

Volume of added D_2O and H_2O	Volume of added 2-PA	Volume of added base	Volume of added Co(II)	Total volume of reaction mixture	Mole fractions of D_2O and H_2O in mixture
1875 µL D_2O	50 µL 2-PA in D_2O	25 µL NaOH in D_2O	50 µL Co(II) in D_2O	2 mL	$D_2O \rightarrow 1$ $H_2O \rightarrow 0$
1800 µL D_2O + 75 µL H_2O	50 µL 2-PA in H_2O	25 µL NaOH in H_2O	50 µL Co(II) in H_2O	2 mL	$D_2O \rightarrow 0.9$ $H_2O \rightarrow 0.1$
1400 µL D_2O + 475 µL H_2O	50 µL 2-PA in H_2O	25 µL NaOH in H_2O	50 µL Co(II) in H_2O	2 mL	$D_2O \rightarrow 0.7$ $H_2O \rightarrow 0.3$
1000 µL D_2O + 875 µL H_2O	50 µL 2-PA in H_2O	25 µL NaOH in H_2O	50 µL Co(II) in H_2O	2 mL	$D_2O \rightarrow 0.5$ $H_2O \rightarrow 0.5$
600 µL D_2O + 1275 µL H_2O	50 µL 2-PA in H_2O	25 µL NaOH in H_2O	50 µL Co(II) in H_2O	2 mL	$D_2O \rightarrow 0.3$ $H_2O \rightarrow 0.7$
200 µL D_2O + 1675 µL H_2O	50 µL 2-PA in H_2O	25 µL NaOH in H_2O	50 µL Co(II) in H_2O	2 mL	$D_2O \rightarrow 0.1$ $H_2O \rightarrow 0.9$
1875 µL H_2O	50 µL 2-PA in H_2O	25 µL NaOH in H_2O	50 µL Co(II) in H_2O	2 mL	$D_2O \rightarrow 0$ $H_2O \rightarrow 1$

TH-2949_166122105

Table 5.2. Quantities of components in the synthesis of bridged polynuclear complex in presence of Au nanoparticles.

Volume of added D_2O and H_2O	Volume of added 2-PA	Volume of added base	Volume of added Co(II)	Volume of added Au nanoparticles	Total volume of reaction mixture	Mole fractions of D_2O and H_2O in mixture
1875 µL D_2O	50 µL 2-PA in D_2O	25 µL NaOH in D_2O	50 µL Co(II) in D_2O	1000 µL Au NP in D_2O	3 mL	$D_2O \rightarrow 1$ $H_2O \rightarrow 0$
1800 µL D_2O + 75 µL H_2O	50 µL 2-PA in H_2O	25 µL NaOH in H_2O	50 µL Co(II) in H_2O	900 µL Au NP in D_2O + 100 µL Au NP in H_2O	3 mL	$D_2O \rightarrow 0.9$ $H_2O \rightarrow 0.1$
1400 µL D_2O + 475 µL H_2O	50 µL 2-PA in H_2O	25 µL NaOH in H_2O	50 µL Co(II) in H_2O	700 µL Au NP in D_2O + 300 µL Au NP in H_2O	3 mL	$D_2O \rightarrow 0.7$ $H_2O \rightarrow 0.3$
1000 µL D_2O + 875 µL H_2O	50 µL 2-PA in H_2O	25 µL NaOH in H_2O	50 µL Co(II) in H_2O	500 µL Au NP in D_2O + 500 µL Au NP in H_2O	3 mL	$D_2O \rightarrow 0.5$ $H_2O \rightarrow 0.5$
600 µL D_2O + 1275 µL H_2O	50 µL 2-PA in H_2O	25 µL NaOH in H_2O	50 µL Co(II) in H_2O	300 µL Au NP in D_2O + 700 µL Au NP in H_2O	3 mL	$D_2O \rightarrow 0.3$ $H_2O \rightarrow 0.7$
200 µL D_2O + 1675 µL H_2O	50 µL 2-PA in H_2O	25 µL NaOH in H_2O	50 µL Co(II) in H_2O	100 µL Au NP in D_2O + 900 µL Au NP in H_2O	3 mL	$D_2O \rightarrow 0.1$ $H_2O \rightarrow 0.9$
1875 µL H_2O	50 µL 2-PA in H_2O	25 µL NaOH in H_2O	50 µL Co(II) in H_2O	1000 µL Au NP in H_2O	3 mL	$D_2O \rightarrow 0$ $H_2O \rightarrow 1$

5.2.4. Instruments used: (i) Horiba LabRAM HR Evolution microscope Raman instrument was used to record Raman spectra. (ii) PerkinElmer® Lambda 35 double beam UV-Vis spectrophotometer was used to record UV-Vis spectra. (iii) Transmission electron microscopic images were acquired using JEOL JEM-2100 transmission electron microscope (operating voltage 200 kV).

TH-2949_166122105

5.3. Result and Discussion

Bridged polynuclear peroxo complex of Co(II) and 2-PA was synthesized following a reported procedure.[27] Briefly, in the basic medium (pH~11), Co(II) was reacted with 2-PA to form the peroxo complex with the appearance of a peak at 595 nm in the UV-Vis spectrum (**Figure A5.1, Appendix**) – owing to the charge transfer from peroxo group to Co(III) center.[27] The extinction at the 595 nm of the product complex enabled attaining resonance Raman (RR) condition when the excitation wavelength was 632.8 nm.[27] The formation and structure of the product polynuclear peroxo species is shown in **Scheme 5.1**.[27] The experimental evidences – such as the calculated and experimental mass spectra, Raman spectra, UV-Vis spectra, TEM images along with SAED pattern, EDS spectra along with elemental mapping - supporting the structure of the product and the catalytic role of Au nanoparticles in the formation of product were presented in our earlier work reported.[27]

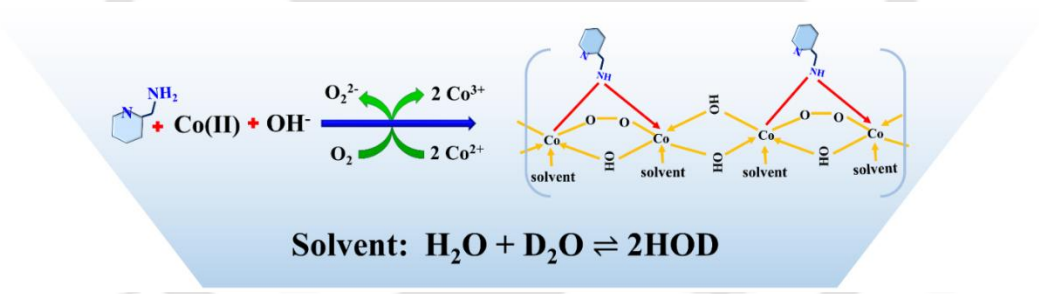

Scheme 5.1. Synthesis of bridged polynuclear peroxo complex in solvent having different mole fractions of H_2O and D_2O. These reactions are applicable for both in the absence and presence of Au nanoparticles.

TH-2949_166122105

When the complexation reaction between Co(II) and 2-PA was carried out in pure H_2O medium under alkaline condition, the recorded RR spectrum for the product showed various characteristic Raman peaks (**Figure 5.1A**) positioned at 644, 897, 1025, 1269 and 1512 cm^{-1}, which are assigned to the symmetric stretching of cobalt-oxygen bond, stretching of peroxo, symmetric trigonal ring breathing mode, bending of CH_2, and in plane vibration of ring, respectively.[27] When the same reaction was carried out in pure D_2O medium, recorded RR spectrum showed major vibrational peaks positioned at 629, 823, 1025, 1271 and 1075 & 1508 cm^{-1}, which are assigned to the symmetric stretching of cobalt-oxygen bond, stretching of peroxo, symmetric trigonal ring breathing mode, bending of CH_2 and in plane vibrations, respectively. The most interesting observation was that the peroxide peak appeared at 897 cm^{-1} in H_2O medium, whereas it appeared at 823 cm^{-1} in D_2O medium. This distinct redshift over 74 cm^{-1} for the peroxo stretching frequency is shown in **Figure 5.1A**. Moreover, 1075 cm^{-1} peak appeared only in D_2O medium, whereas it was absent in H_2O medium. When we carried out the same reaction in solvent having different H_2O & D_2O mole fractions, we observed some more significant changes in the RR spectra. The intensity of the peak at 897 cm^{-1} was enhanced as the mole fraction of H_2O was increased, whereas

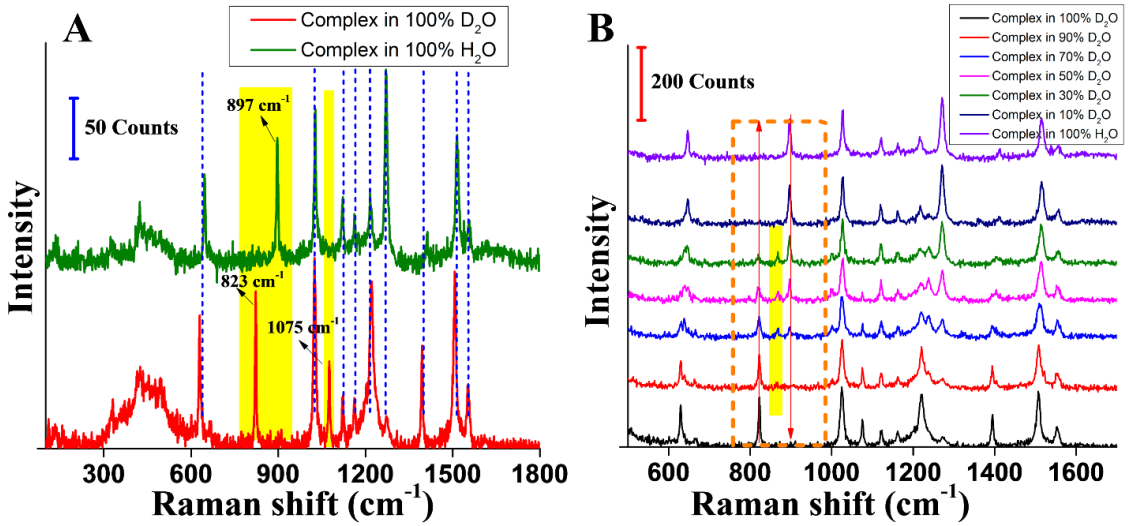

Figure 5.1. (**A**) RR spectrum of product polymer in pure H_2O and D_2O. (**B**) RR spectrum of product polymer in various mixtures of H_2O and D_2O.

the intensity of 823 cm^{-1} was enhanced as the mole fraction of D_2O was increased (**Figure 5.1B**). In solvents having both H_2O and D_2O, a new peak arose at 863 cm^{-1} and its intensity was maximum in the presence of equal mole fractions of H_2O and D_2O in the solvent as

TH-2949_166122105

shown in **Figure 5.1B**. The new peak could be considered to have arisen due to the collective effect of adding masses to the peroxo "oscillator" through hydrogen bonding i.e., the coupling between the O-O and adjoining O••D/O••H hydrogen bonds.[29,30]

We noticed that although we were able to distinguish peaks due different mole fractions of H_2O/D_2O in the medium, the signal to noise ratio of the peaks especially indicative of the bonding between the solvent molecules and the complex needed to be improved for better analysis. This was especially required for identification of HOD in the medium. We thus pursued SERRS.

We synthesized citrate stabilized Au nanoparticles and the corresponding TEM image along with size distribution are shown in **Figure A5.2 (Appendix)**. The average diameter of Au nanoparticle was calculated to be 18±2 nm. When we performed the complexation reaction on the surface of Au nanoparticles and in solvents having different mole fractions of H_2O and D_2O, we observed spectra in SERRS that were similar to those in RRS but with much better signal to noise ratio and better-resolved peaks as is shown in **Figure 5.2**. For example, in solvent having equal mole fractions of H_2O and D_2O, the peak that appeared at ~640 cm^{-1} was broad in RRS spectrum (**Figure 5.1B**) but in SERRS spectrum (**Figure 5.2Aii**) it was split into 3 different peaks with better signal to noise ratio. The peaks assigned to Co-N bond, symmetric stretching of cobalt-oxygen (of peroxo) bond, stretching of peroxo, symmetric trigonal ring breathing mode, bending of CH_2, and in plane vibration appeared at 519, 646, 895, 1025, 1220 and 1509 cm^{-1}, respectively, in pure H_2O medium, whereas they appeared at 495, 629, 823, 1025, 1218 and 1502 cm^{-1}, respectively, in pure D_2O medium (**Figure 5.2A**). In solvents having both H_2O and D_2O, a new peak at 867 cm^{-1} appeared in the SERRS spectra and its intensity was maximum in the presence of equal mole fractions of H_2O and D_2O as shown in **Figure 5.2Ai**. Since the SERRS spectra were of superior quality and better resolved, quantitative analyses of them recorded in the presence of different H_2O/D_2O solvent mixtures were made. The significant observations with respect to the vibrational peaks are summarized in **Figure 5.2B**.

Since the extended peak shift was a result of the combined effect of adding extra mass to the peroxo "oscillator" and the coupling between the O-O and adjoining O••D/O••H hydrogen bonds,[29,30] a brief account of the results based on hydrogen bonding between the

TH-2949_166122105

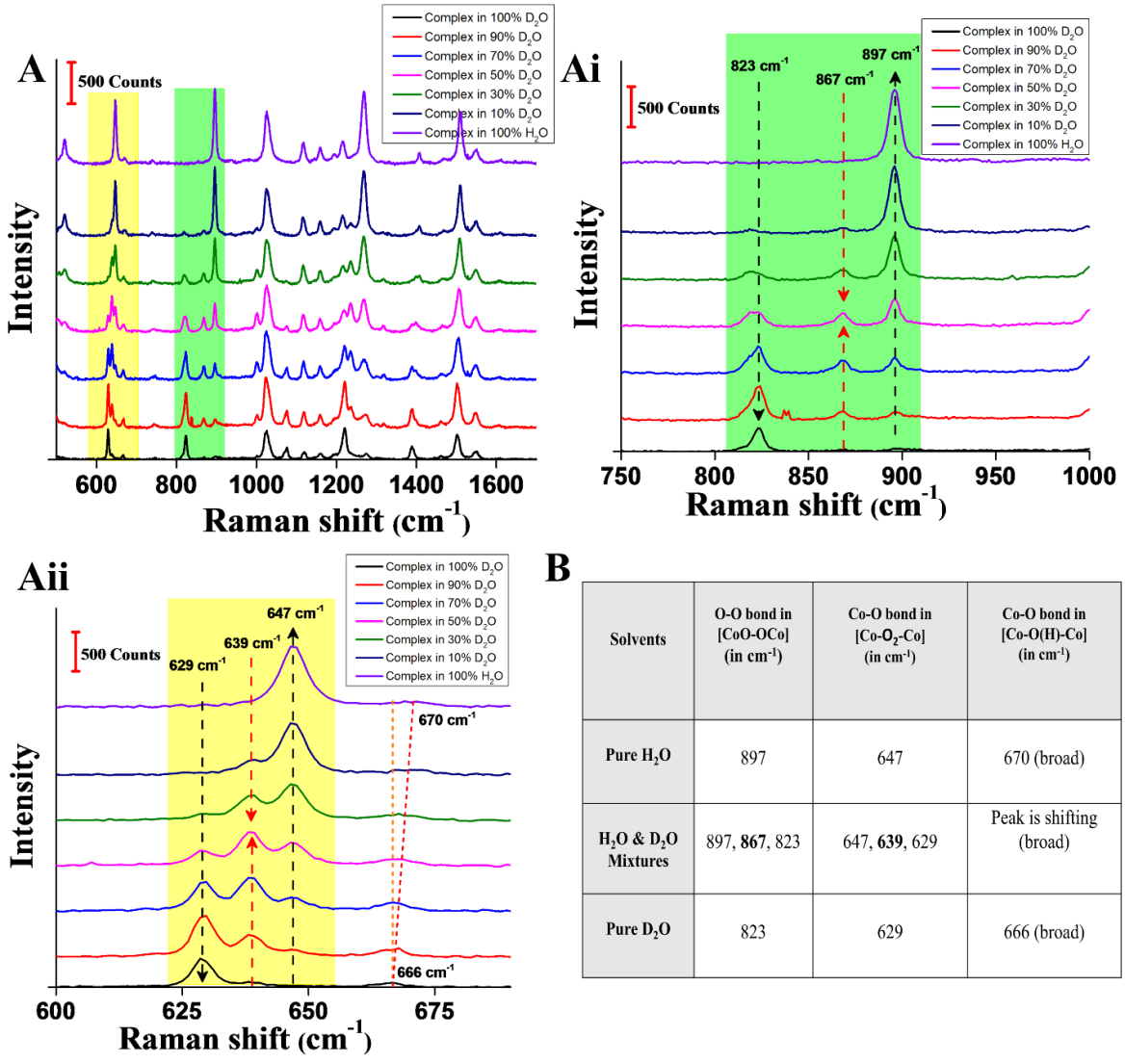

B

Solvents	O-O bond in [CoO-OCo] (in cm^{-1})	Co-O bond in [Co-O_2-Co] (in cm^{-1})	Co-O bond in [Co-O(H)-Co] (in cm^{-1})
Pure H_2O	897	647	670 (broad)
H_2O & D_2O Mixtures	897, **867**, 823	647, **639**, 629	Peak is shifting (broad)
Pure D_2O	823	629	666 (broad)

Figure 5.2. (**A**) SERRS spectrum of product polymer in solvents having different mole fractions of H_2O and D_2O in presence of Au nanoparticles along with expanded highlighted regions (**Ai**, **Aii**). (**B**) Vibrational peak positions of O-O (of CoO-OCo), Co-O (of Co-O_2-Co) and Co-O (of Co-O(H)-Co) are identified for different mole fractions of H_2O/ D_2O.

metal complex and the solvent (H_2O/D_2O) is presented in **Table 5.3**. When the cobalt-peroxo complex was formed in H_2O, the hydrogen bonded structure of the peroxo group led to the appearance of a single peak at 895 cm^{-1}. In less polar D_2O that can form stronger hydrogen

TH-2949_166122105

bond as compared to H_2O,[24] the vibrational frequency of peroxo bond was shifted towards lower energy and the peak appeared at 823 cm^{-1}. In a solvent that contains mixtures of H_2O and D_2O, HOD is formed from the reaction between the components. Therefore, in solvent having both H_2O and D_2O, peroxide can form hydrogen bonds with H_2O, D_2O and HOD, separately. Thus, the vibrational frequencies of peroxides that appeared at ~897, 823 and 867 cm^{-1} represented the hydrogen bonded structures of the peroxide with H_2O, D_2O and HOD, respectively. In pure H_2O or D_2O, there is only one possible hydrogen bonded structure between peroxide and solvent molecules as shown in **Table 5.3** and thus, the expected number of peaks for peroxide would be one. But in solvent having different mole fractions of H_2O and D_2O, total number of hydrogen bonded structures is three, if **possibility A** was followed and five, if **possibility B** was followed. Since we observed three peaks for peroxide in the solvents having a mixture of H_2O and D_2O, we may conclude that the **possibility A** was exhibited experimentally.

Further, the broad peak that appeared at 670 cm^{-1} associated with Co-oxygen bond (of Co-O(H)-Co) in pure H_2O was shifted to 666 cm^{-1} (**Figure 5.2Aii**) with the introduction of D_2O in the medium, due to the replacement of hydrogen by deuterium in Co-O(H)-Co (refer the complex structure shown in **Scheme 5.1**)[29,30]. Since the resolution of this peak was poor, it appeared broad instead of two distinct peaks (one for Co-O(H)-Co and other for Co-O(D)-Co) in the solvent mixture of H_2O/D_2O. Whereas the Co-oxygen (of Co-O_2-Co) bond showed different spectral features (**Figure 5.2Bi**). Raman peak of Co-oxygen (of Co-O_2-Co) bond appeared at 647 and 629 cm^{-1} in pure H_2O and D_2O solvent, respectively. In mixtures of H_2O and D_2O, there was the appearance of a new peak at 639 cm^{-1}. This can be explained by the formation of hydrogen bonds with Co-O-O-Co unit. When both the oxygen of peroxo formed hydrogen bonds with H_2O and D_2O, we observed one peak for Co-oxygen (of the Co-O_2-Co) bond in the vibrational spectra (**Figure 5.2Ai**). But in the mixture of H_2O and D_2O there are three possibilities of hydrogen bonded structures between peroxo and solvent as shown in **Table 5.3** and that resulted in the appearance of three different peaks.

TH-2949_166122105

Table 5.3. Different possibilities regarding hydrogen bonding with peroxide and corresponding expected number of peaks.

Solvent	Possibility A	Expected Number of O-O Peaks	Expected Number of Co-O Peaks	Possibility B	Expected Number of O-O Peaks
Pure H_2O	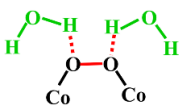	1	1	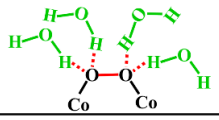	1
H_2O & D_2O Mixtures	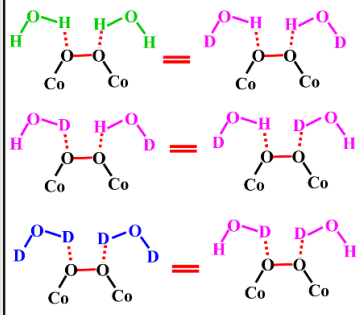	3	3	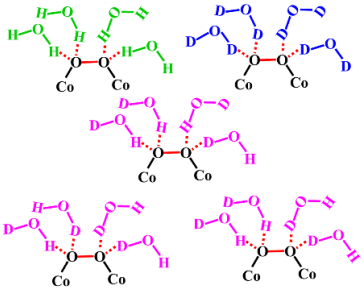	5
Pure D_2O	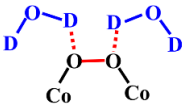	1	1	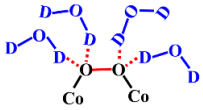	1

Next, we plotted the peak intensity ratios for 895, 867 and 823 cm^{-1} normalized with respect to a standard peak positioned at 1025 cm^{-1} (corresponding to symmetric trigonal ring breathing mode of vibration) against mole fraction of solvent containing H_2O and D_2O (shown in **Figure 5.3**). The results in **Figure 5.3** demonstrate that the peak ratio for 895 cm^{-1} gradually increased as the mole fraction of H_2O had increased, peak ratio for 823 cm^{-1} increased as the mole fraction of D_2O had increased and the maximum peak intensity ratio representing HOD formation occurred when the solvent had equal mole fractions of H_2O and D_2O. The LOD for D_2O was calculated to be 0.028 mole fraction (or 2.8% D_2O in H_2O) and for H_2O it was found to be 0.046 mole faction (or 4.6% D_2O in H_2O). In addition, the lowest detection of HOD was calculated to be 0.079 mole fraction of D_2O in H_2O and 0.088 mole fraction of H_2O in D_2O (refer **Figure 5.3**). We wish to emphasize here too that spectra recorded in the presence of Au nanoparticles provided the best options in terms of signal to noise ratio and therefore estimation of the mole fractions of H_2O/D_2O in the solvent mixture.

TH-2949_166122105

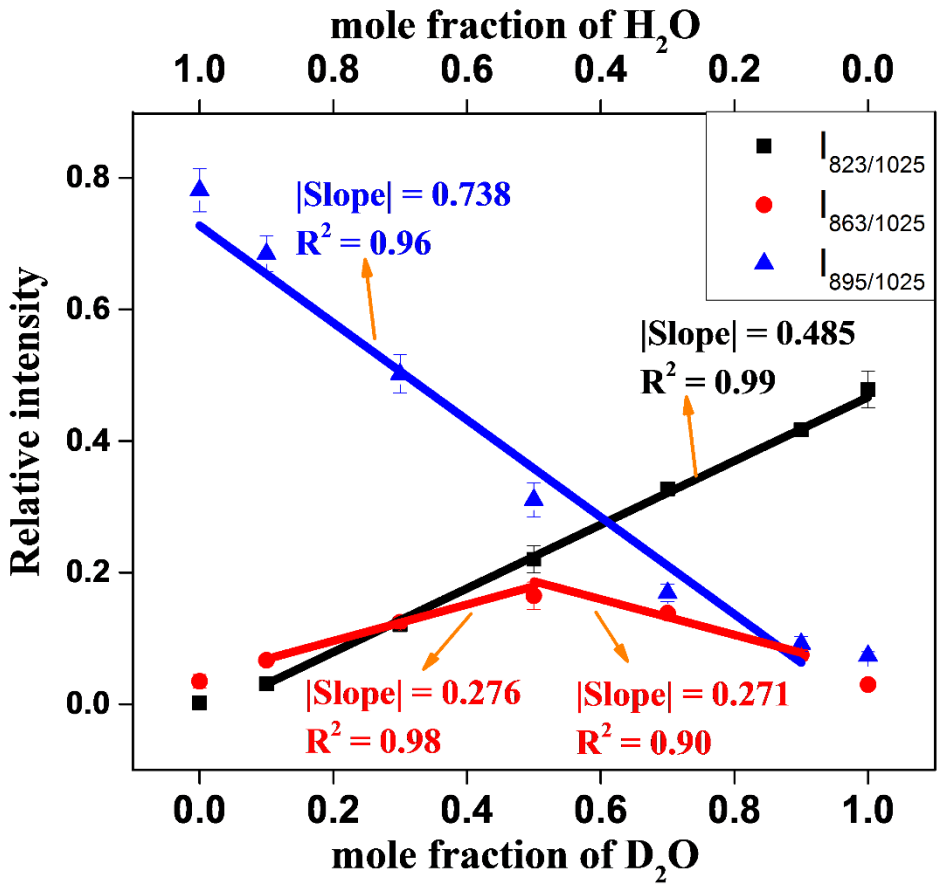

Figure 5.3. Correlation between intensity of peroxo peak with varying mole fractions of H_2O/D_2O in presence of Au nanoparticles. Here, intensity was calculated normalized with respect to the standard peak situated at 1025 cm^{-1}. $I_{823/1025}$, $I_{863/1025}$ and $I_{895/1025}$ represent the intensities of peaks due to presence of D_2O, HOD and H_2O, respectively. All the experiments were carried out in triplicate.

Literature report suggests that binuclear species of cobalt-peroxo complex tentatively prefers cis peroxide configuration.[31] **Table 5.3** along with **Figure 5.3** showed that peroxide formed two hydrogen bonds with solvent molecules and for the first time this has been reported here.

5.4. Conclusions

In summary, we reported a novel strategy to detect H_2O, D_2O and HOD in their mixtures using single vibrational mode based RRS and SERRS in the absence and presence of Au nanoparticles, respectively. Bridged polynuclear peroxo complex was synthesized in solvent

TH-2949_166122105

mixtures of H_2O and D_2O containing their different mole fractions. Hydrogen bonds between peroxide and solvent molecules (H_2O, D_2O and HOD) significantly shifted the vibrational frequency of the peroxo bond. Reactions between different H_2O and D_2O concentrations produced different HOD concentrations and that led to different intensities of peaks positioned at 895, 823 and 867 cm^{-1}, which facilitated the quantitative detection of H_2O, D_2O and HOD content, respectively, in the mixtures. We believe this work opens a new pathway to distinguish various isotopic solvents quantitatively.

5.5. References

1. Rowinski, M. K.; White, T. J.; Zhao, J. Y. *Renewable Sustainable Energy Rev.* **2015**, *44*, 643.

2. Bromley, B. P.; Colton, A. V.; Golesorkhi, S. *Ann. Nucl. Energy* **2019**, *124*, 399.

3. Kluge, H.; Weise, K.; Hunt, J. B. *Radiat. Prot. Dosim.***1990**, *32*, 233.

4. Aharmim, B.; Ahmed, S. N.; Anthony, A. E.; Beier, E. W. *Phys. Rev. C: Nucl. Phys.* **2005**, *72*, 055502.

5. Boger, J.; Hahn, R.; Rowley, J.; et al., *Nucl. Instrum. Methods Phys. Res.* **2000**, *449*, 172.

6. Bellerive, A.; Klein, J. R.; et al., *Nucl. Phys. B* **2016**, *908*, 30.

7. Roberts, J. D. *Nuclear Magnetic Resonance: applications to organic chemistry, McGraw-Hill Book Company* **1959**.

8. Emsley, J.; Feeney, J.; Sutcliffe, L. H. *High Resolution Nuclear Magnetic Resonance Spectroscopy V.2, Pergamon* **1995**.

9. Baenziger, J. E.; Methot, N. *J. Biol. Chem.* **1995**, *270*, 29129.

10. Hesse, U. J.; Gores, P. F.; et al., *Transplant. Proc.* **1987**, *19*(5), 4167.

11. Tcelykh, L.; Kozhevnikova (Khudoleeva), V.; Goloveshkin, A.; Lepnev, L.; Popelensky, T.; Utochnikova, V. *Analyst* **2020**, *145*, 759.

TH-2949_166122105

12. Dunning, S. G.; Nunez, A. J.; Moore, M. D.; Steiner, A.; Lynch, V. M.; Sessler, J. L.; Holliday, B. J.; Humphrey, S. M. *Chem.* **2017**, *2*, 579-589.

13. Meijer, G.; Meulen, J.J. T.; Andresen, P.; Bath, A. *J. Chem. Phys*. **1986**, *85*, 6914-6922.

14. Olson, D. L.; Lacey, M. E.; Webb, A. G.; Sweedler, J. V. Anal. *Chem.* **1999**, *71*, 3070.

15. Xiong, F. B.; Zhu, W. Z.; Lin, H. F. *Appl. Mech. Mater*. **2013**, *303*, 59.

16. Armani, A. M.; Vahala, K. J. *Opt. Lett.* **2006**, *31*, 1896.

17. Xiong, F. B.; Zhu, W. Z.; Meng, X. G.; Lin, H. F.; Huang, X. H.; Huang, Y. Q. *Optik* **2013**, *124*, 2008.

18. Park, K.; Kimand, Y.; Lee, K. J. *J. Radioanal. Nucl. Chem*. **2019**, *322*, 487.

19. Dong, B.; Lu, Y.; Song, W.; Kong, X.; Sun, Y.; Lin, W. *Chem. Commun*. **2020**, *56*, 1191-1194.

20. Zhang, Y.; Chen, L.; Liu, Z.; Liu, W.; Yuan, M.; Shu, J.; Wang, N.; He, L.; Zhang, J.; Xie, J.; Chen, X.; Diwu, J. *ACS Appl. Mater. Interfaces* **2020**, *12*, 16648-16654.

21. Hawes, C. S.; Gunnlaugsson, T. Chem **2017**, *2*, 459-469.

22. Meija, J.; Mester, Z. *J Am Soc Mass Spectrom* **2006**, *17*, 1028-1036.

23. Hu, Q.; Zhao, H.; Ouyang, S. *Phys.Chem.Chem.Phys.* **2017**, *19*, 21540.

24. Hu, Q.; Ouyang, S.; Lia, J.; Cao, Z. *J. Raman Spectrosc*. **2017**, *48*, 610-617.

25. Baschenko, S. M.; Marchenko, L. S. *Semiconductor Physics, Quantum Electronics & Optoelectronics* **2011**, *14*, 77-79.

26. Zarei, A.; Klumbach, S.; Keppler, H. *ACS Earth Space Chem* **2018**, *2*, 925-934.

27. Pal, S.; Paul, S.; Chattopadhyay, A. *ChemistrySelect* **2022**, *7*, e202201569.

28. Churakov, A. V.; Grishanov, D. A.; Medvedev, A. G.; Mikhaylov, A. A.; Vener, M. V.; Navasardyan, M. A.; Tripol'skaya, T. A.; Lev, O.; Prikhodchenko, P. V. *CrystEngComm* **2020**, *22*, 2866.

29. Bi, X.; Miao, K.; Wei, L. *J. Am. Chem. Soc.* **2022**, *144*, 8504–8514.

TH-2949_166122105

30. Chen, Z.; Paley, D. W.; Wei, L.; Weisman, A. L.; Friesner, R. A.; Nuckolls, C.; Min, W. *J. Am. Chem. Soc.* **2014**, *136*, 8027-8033.

31. Goodman, G. L.; Hecht, H. G.; Weil, J. A. *Advances in Chemistry* **1962**, *8*, 90-97.

TH-2949_166122105

Appendix of Chapter 5: A5

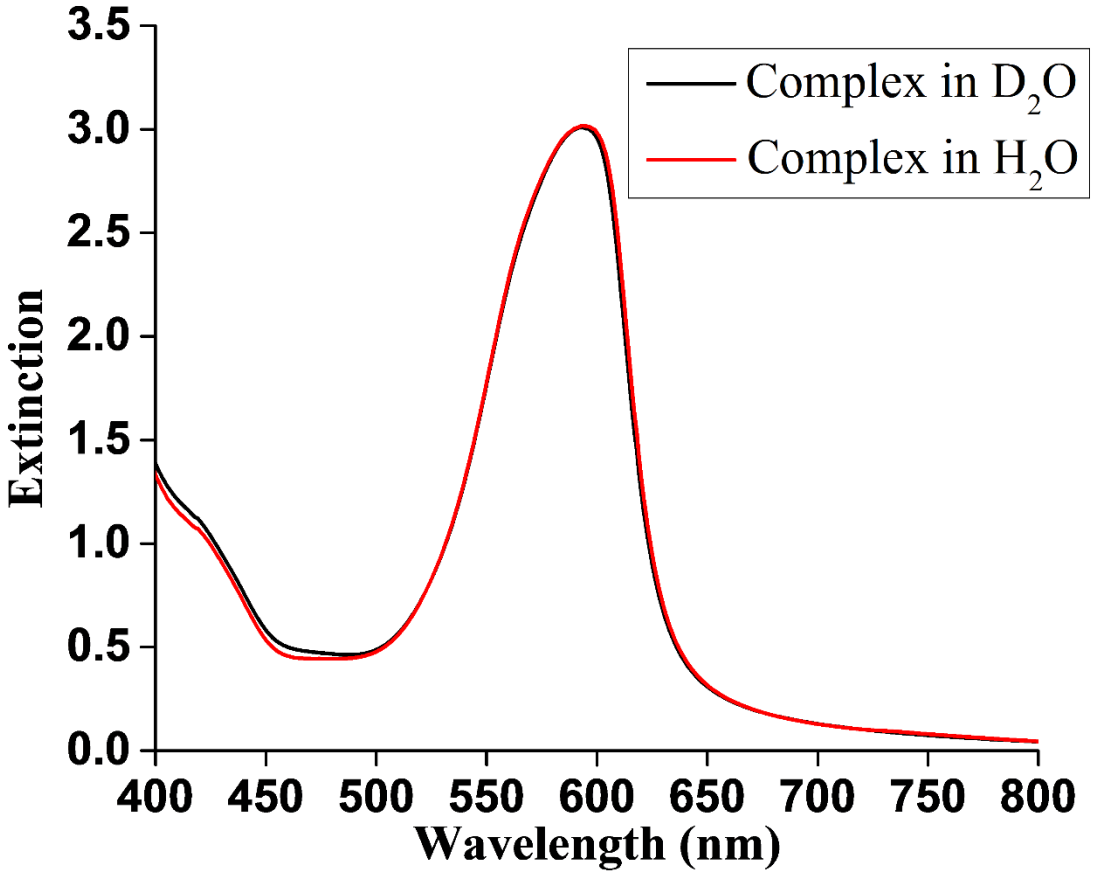

Figure A5.1. UV-Vis spectra of the complex product in pure H_2O and D_2O, respectively.

TH-2949_166122105

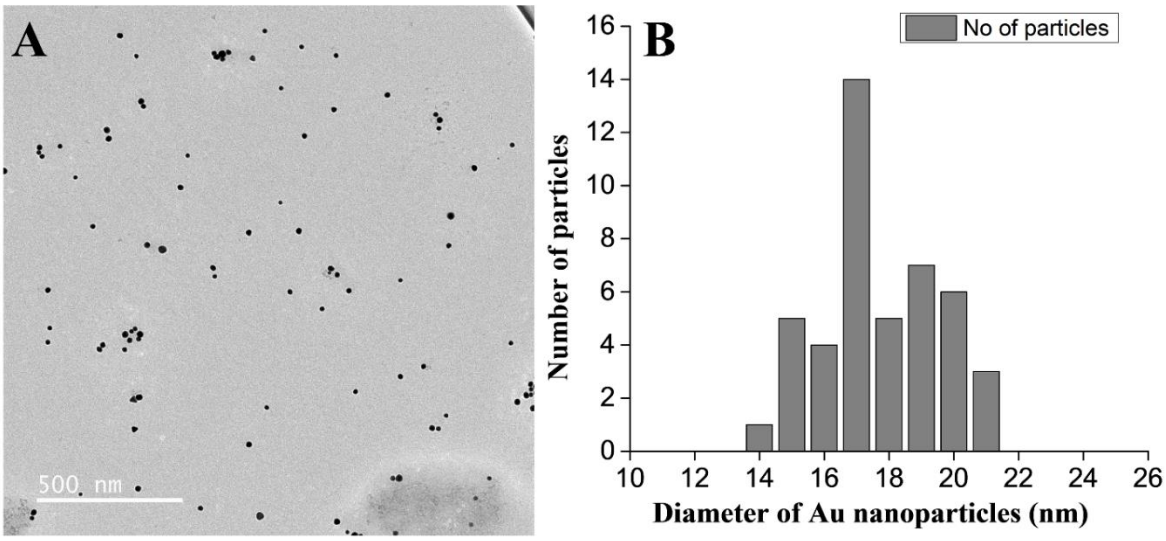

Figure A5.2. TEM image (**A**) and size distribution (**B**) of as synthesized Au nanoparticles.

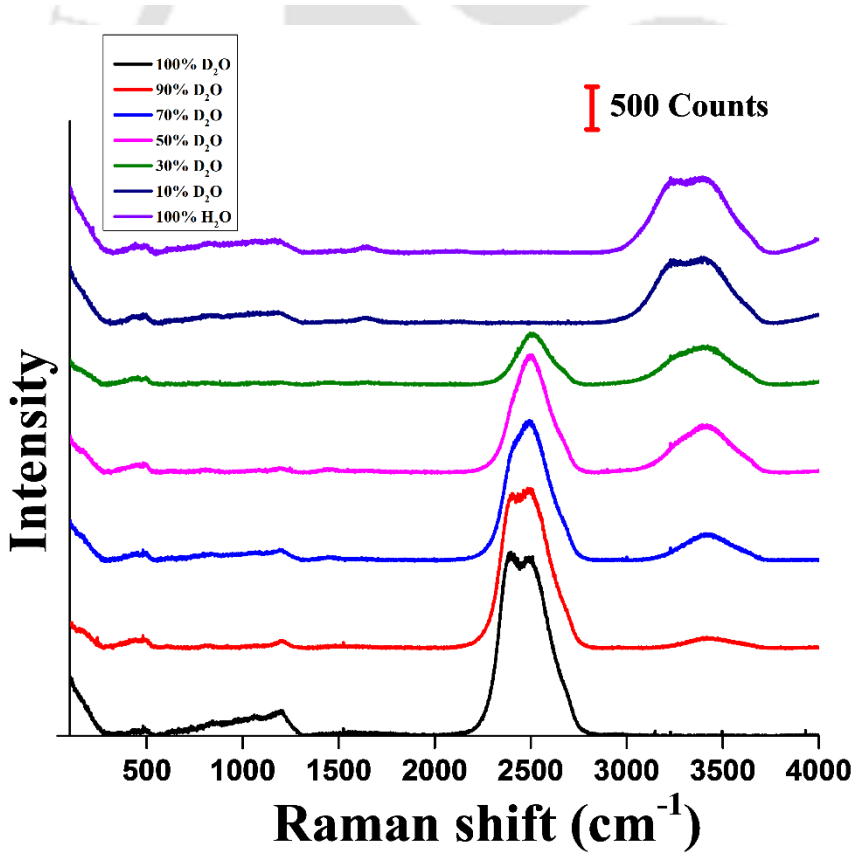

Figure A5.3. Raman spectra of solvents having different mole fractions of H_2O and D_2O.

TH-2949_166122105

Table A5.1. Tabulated form of the comparison of different optical techniques and probes for detection H_2O in D_2O, D_2O in H_2O and HOD.

Reference No	Recent Used Optical Technique/ Probe	Detected Species	Advantages	Limitations
This work	Surface enhanced resonance Raman scattering (Peroxo complex/ Au nanoparticle)	• H_2O in D_2O • D_2O in H_2O • HOD	• Characteristic peak for each species • Can detect H_2O, D_2O and HOD simultaneously in a single Raman spectrum • Easy synthesis and less time required	—
2	Luminescence (Fluorophores)	H_2O in D_2O	Turn-on emission signal	• Cannot detect HOD • Cannot detect D_2O in H_2O • Time consuming and complicated fabrication
3	Luminescence (Uranyl/lanthanide Framework)	D_2O in H_2O	Ratiometric detection	• Use of Radioactive ^{238}U • Cannot detect HOD • Cannot detect H_2O in D_2O • Time consuming and complicated fabrication
4	Luminescence (Carbon polymer dots)	H_2O in D_2O	Green synthesis	• Use of turn-off emission signal • Cannot detect HOD • Cannot detect D_2O in H_2O • Complicated fabrication
5	Luminescence (Lanthanide polymer)	D_2O in H_2O	Ratiometric detection	• Cannot detect HOD • Cannot detect H_2O in D_2O • Complicated fabrication
6	Luminescence (Lanthanide MOF)	H_2O in D_2O	Ratiometric detection	• Cannot detect HOD • Cannot detect D_2O in H_2O • Time consuming and complicated fabrication

References:

1. Ojea-Jiménez, O.; I.; Romero, F. M.; Bastús, N. G.; Puntes, V, *J. Phys. Chem. C* **2010,** *114*, 1800-1804

2. Dong, B.; Lu, Y.; Song, W.; Kong, X.; Sun, Y.; Lin, W. *Chem. Commun*. **2020**, *56*, 1191-1194.

3. Zhang, Y.; Chen, L.; Liu, Z.; Liu, W.; Yuan, M.; Shu, J.; Wang, N.; He, L.; Zhang, J.; Xie, J.; Chen, X.; Diwu, J. *ACS Appl. Mater. Interfaces* **2020**, *12*, 16648-16654.

TH-2949_166122105

4. Xia, J.; Yu, Y. L.; Wang, J. H. *Chem. Commun.* **2019**, *55*, 12467-12470.

5. Hawes, C. S.; Gunnlaugsson, T. *Chem* **2017**, *2*, 459-469.

6. Dunning, S. G.; Nunez, A. J.; Moore, M. D.; Steiner, A.; Lynch, V. M.; Sessler, J. L.; Holliday, B. J.; Humphrey, S. M. *Chem* **2017**, *2*, 579-589.

TH-2949_166122105

CHAPTER 6

6.1. Thesis Summary

In summary, the present thesis illustrates the potential applications of Au nanostructures in plasmon induced photochemical reactions as well as in catalyzing inorganic bridged polynuclear complex synthesis. In this regard, end-to-end assembled Au nanorods were formed exploiting selective binding nature of 4-ATP (maintaining lower concentration) at the longitudinal end of Au nanorods. In the assembly of Au nanorods, H-bonded dimeric structure of 4-ATP molecules were positioned at the hot-spots. Illumination of laser converted 4-ATP molecules adsorbed at the surface of Au nanorods into DMAB. The kinetic rate of this plasmon driven photochemical reaction at the hot spot was faster than that at the longitudinal end surface of non-assembled Au nanorods. The formation of DMAB from 4-ATP was feasible at the surface of Au nanostructures. Further the presence of transition metal cations significantly increased the yield of DMAB. During the oxidation of 4-ATP into DMAB, the oxidation states of metal cations plausibly were changed, leading to the formation of metal oxides, which augmented the SERS signal. Separately, 2-PA molecules reacted with Co(II) in aqueous alkaline medium and formed amorphous bridged polynuclear peroxo complex. 2-PA molecules were adsorbed on Au nanospheres following Langmuir adsorption isotherm and following formation of the complex SERRS conditions were met. That helped in deciphering the structure and bonding of the complex product. The product formation was also catalyzed by the Au nanospheres. Additionally, the complex polynuclear species was exploited to detect H_2O, D_2O and HOD simultaneously in a single SERRS spectrum using the vibrational modes of peroxide. H_2O, D_2O and HOD formed different nature of hydrogen bonded structures with peroxide of the complex and that resulted in significant vibrational frequency shift of the peroxide bond. The nature of hydrogen bonding with three different species (based on H or D being bonded to the peroxide) provided an estimation of the content of H_2O or D_2O in the mixture.

TH-2949_166122105

6.2. Future Prospects

At the hot spots of assembled Au nanorods, the rate constant of 4-ATP into DMAB conversion was higher compared to that at the typical surface of Au nanorods. Further, the presence of metal cations increased the rate of 4-ATP into DMAB conversion and the yield of product. Therefore, the idea of carrying out any plasmon induced photochemical reaction at the hot spots of plasmonic-nanostructures in the presence of transition metal cations could serve as a better approach to get the extraordinary rate constant as well as yield of product and that need to be explored thoroughly. On the other hand, potential applications of plasmonic-nanostructures could be extended to the complex inorganic chemistry other than plasmon mediated photochemical reactions. SERRS studies and the usage of metal nanostructures could help in proposing the plausible structure and bonding of amorphous inorganic complex product. Adsorption of 2-PA ligand at the surface of Au nanospheres reduced the HOMO-LUMO energy gap of the ligand, which in turn catalyzed the formation of bridged polynuclear peroxo complex product. Thus, carrying out any complexation reaction at the surface of metal nanostructures could be a better approach for up and coming filed of inorganic chemistry. In addition, peroxo group of metal polynuclear peroxo species can easily form different nature of hydrogen bonded structures with solvent molecules. This phenomenon can be utilized to detect various isotopic solvents quantitatively on the basis of characteristic signal in the SERRS spectrum.

TH-2949_166122105

Publications

Publications based on the work reported in the thesis

1) **Pal, S**.; Dutta, A.; Paul, M.; Chattopadhyay, A. Plasmon-Enhanced Chemical Reaction at the Hot Spots of End-to-End Assembled Gold Nanorods. *J. Phys. Chem. C* 2020, 124, 3204-3210.

2) **Pal, S**.; Paul, S.; Chattopadhyay, A. Enhanced Solid-State Plasmon Catalyzed Oxidation and SERS Signal in the Presence of Transition Metal Cations at the Surface of Gold Nanostructures. *Phys. Chem. Chem. Phys.* 2021,23, 21808-21816.

3) **Pal, S**.; Paul, S.; Chattopadhyay, A. Dual Role of Au Nanoparticles in the Catalytic Formation of an Amorphous Polynuclear Peroxo Complex and Surface Enhanced Resonance Raman Scattering. *ChemistrySelect* 2022, *7*, e202201569.

4) **Pal, S**.; Chattopadhyay, A. Highly Efficient and Simultaneous Sensing of H_2O, D_2O and HOD through Peroxo Vibrations. [Communicated, 2022]

Publications from collaborations

5) Gogoi, K.; **Pal, S.**; Chattopadhyay, A. Molecule-Assembled Plasmonic Gold Nanoparticle Network for Piezo-Phototronic and Human Activity Detections. [Communicated, 2022]

6) Chowdhuri, A. R.; Laha, D.; **Pal, S**.; Karmakar, P.; Sahu, S. K. One-Pot Synthesis of Folic Acid Encapsulated Upconversion Nanoscale Metal Organic Responsive Drug Release. *Dalton Trans.* 2016, 45, 18120-18132.

TH-2949_166122105

Conferences Attended

1. Participated as **Poster Presenter** in the Research & Industrial Conclave (RIC) 2022, organized by the Students' Academic Board, IIT Guwahati and IIT Guwahati Research Park. [2022]

2. Received Indian Chemical Society **Research Excellence Award** for the **presentation (Oral)** in the 58th Annual Convention of Chemists, 2021 & International Conference on "Recent Trends in Chemical Sciences (RTCS-2021)" organized by the Indian Chemical Society, Kolkata, India. [2021]

3. Participated as **Flash Talk Presenter** in the 7th International Conference on Advanced Nanomaterials and Nanotechnology (ICANN2021), organized by the Centre for Nanotechnology, IIT Guwahati, Assam, India. [2021]

4. Participated in International Hybrid Meeting on Physics and Chemistry of Advanced Materials (PCAM-2021) at Indian Institute of Technology, Delhi and Kasouli, H.P., India. [2021]

5. Participated in 5th National Workshop on NEMS/MEMS & Theranostic Devices, under the aegis of Centre for Nanotechnology, Indian Institute of Technology Guwahati, India. [2019]

TH-2949_166122105

PERMISSIONS

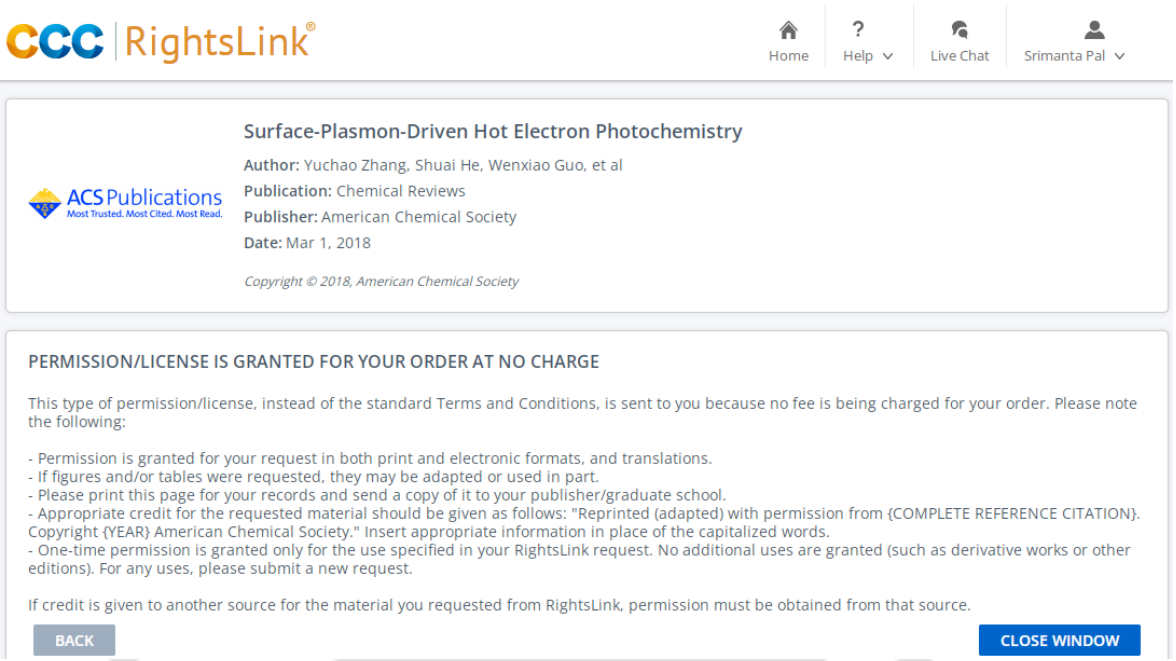

CCC RightsLink®

Home | Help | Live Chat | Srimanta Pal

ACS Publications
Most Trusted. Most Cited. Most Read.

Surface-Plasmon-Driven Hot Electron Photochemistry

Author: Yuchao Zhang, Shuai He, Wenxiao Guo, et al
Publication: Chemical Reviews
Publisher: American Chemical Society
Date: Mar 1, 2018

Copyright © 2018, American Chemical Society

PERMISSION/LICENSE IS GRANTED FOR YOUR ORDER AT NO CHARGE

This type of permission/license, instead of the standard Terms and Conditions, is sent to you because no fee is being charged for your order. Please note the following:

- Permission is granted for your request in both print and electronic formats, and translations.
- If figures and/or tables were requested, they may be adapted or used in part.
- Please print this page for your records and send a copy of it to your publisher/graduate school.
- Appropriate credit for the requested material should be given as follows: "Reprinted (adapted) with permission from {COMPLETE REFERENCE CITATION}. Copyright {YEAR} American Chemical Society." Insert appropriate information in place of the capitalized words.
- One-time permission is granted only for the use specified in your RightsLink request. No additional uses are granted (such as derivative works or other editions). For any uses, please submit a new request.

If credit is given to another source for the material you requested from RightsLink, permission must be obtained from that source.

BACK | CLOSE WINDOW

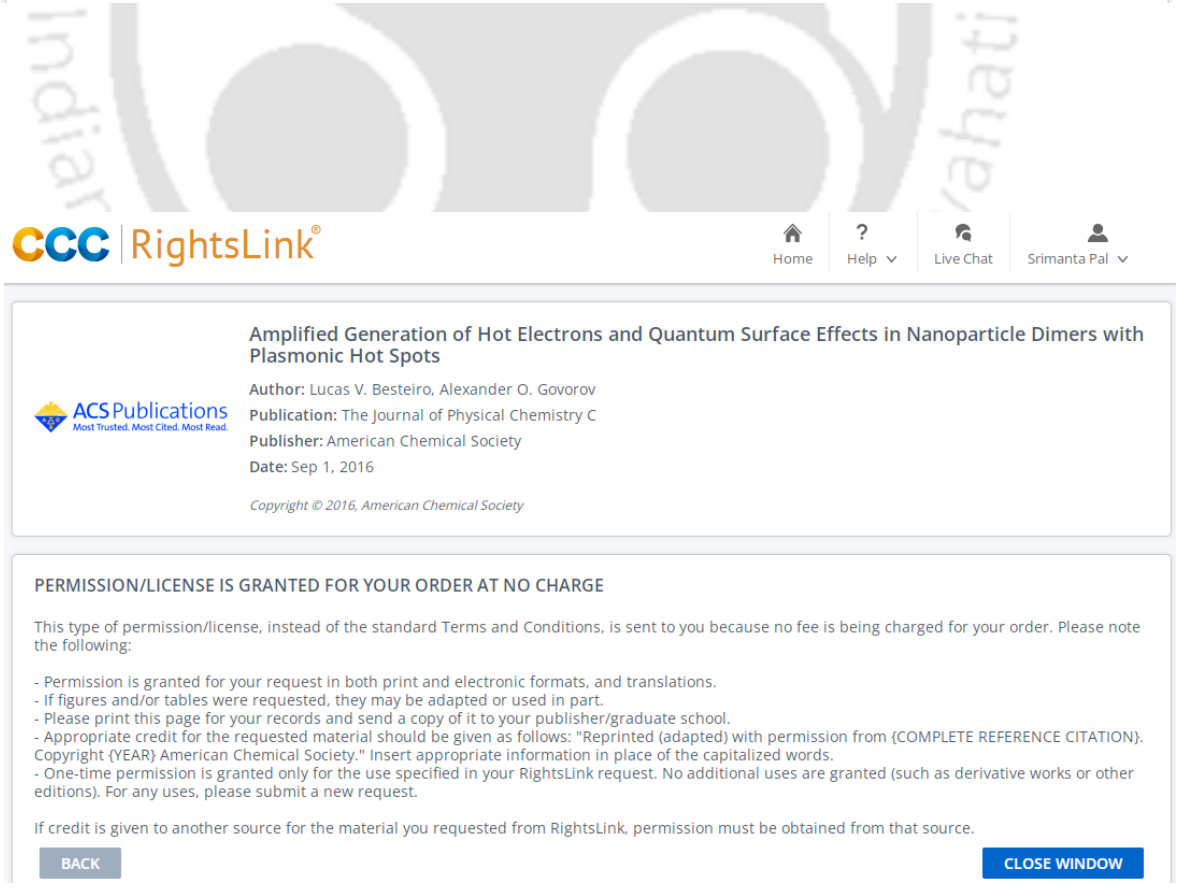

CCC RightsLink®

Home | Help | Live Chat | Srimanta Pal

ACS Publications
Most Trusted. Most Cited. Most Read.

Amplified Generation of Hot Electrons and Quantum Surface Effects in Nanoparticle Dimers with Plasmonic Hot Spots

Author: Lucas V. Besteiro, Alexander O. Govorov
Publication: The Journal of Physical Chemistry C
Publisher: American Chemical Society
Date: Sep 1, 2016

Copyright © 2016, American Chemical Society

PERMISSION/LICENSE IS GRANTED FOR YOUR ORDER AT NO CHARGE

This type of permission/license, instead of the standard Terms and Conditions, is sent to you because no fee is being charged for your order. Please note the following:

- Permission is granted for your request in both print and electronic formats, and translations.
- If figures and/or tables were requested, they may be adapted or used in part.
- Please print this page for your records and send a copy of it to your publisher/graduate school.
- Appropriate credit for the requested material should be given as follows: "Reprinted (adapted) with permission from {COMPLETE REFERENCE CITATION}. Copyright {YEAR} American Chemical Society." Insert appropriate information in place of the capitalized words.
- One-time permission is granted only for the use specified in your RightsLink request. No additional uses are granted (such as derivative works or other editions). For any uses, please submit a new request.

If credit is given to another source for the material you requested from RightsLink, permission must be obtained from that source.

BACK | CLOSE WINDOW

TH-2949_166122105

CCC RightsLink®

Home | Help | Live Chat | Srimanta Pal

ACS Publications
Most Trusted. Most Cited. Most Read.

Kinetically Controlled Seeded Growth Synthesis of Citrate-Stabilized Gold Nanoparticles of up to 200 nm: Size Focusing versus Ostwald Ripening

Author: Neus G. Bastús, Joan Comenge, Víctor Puntes
Publication: Langmuir
Publisher: American Chemical Society
Date: Sep 1, 2011

Copyright © 2011, American Chemical Society

PERMISSION/LICENSE IS GRANTED FOR YOUR ORDER AT NO CHARGE

This type of permission/license, instead of the standard Terms and Conditions, is sent to you because no fee is being charged for your order. Please note the following:

- Permission is granted for your request in both print and electronic formats, and translations.
- If figures and/or tables were requested, they may be adapted or used in part.
- Please print this page for your records and send a copy of it to your publisher/graduate school.
- Appropriate credit for the requested material should be given as follows: "Reprinted (adapted) with permission from {COMPLETE REFERENCE CITATION}. Copyright {YEAR} American Chemical Society." Insert appropriate information in place of the capitalized words.
- One-time permission is granted only for the use specified in your RightsLink request. No additional uses are granted (such as derivative works or other editions). For any uses, please submit a new request.

If credit is given to another source for the material you requested from RightsLink, permission must be obtained from that source.

BACK | CLOSE WINDOW

CCC RightsLink®

Home | Help | Live Chat | Srimanta Pal

Anisotropic Metal Nanoparticles: Synthesis, Assembly, and Optical Applications

Author: Catherine J. Murphy, Tapan K. Sau, Anand M. Gole, et al
Publication: The Journal of Physical Chemistry B
Publisher: American Chemical Society
Date: Jul 1, 2005

Copyright © 2005, American Chemical Society

PERMISSION/LICENSE IS GRANTED FOR YOUR ORDER AT NO CHARGE

This type of permission/license, instead of the standard Terms and Conditions, is sent to you because no fee is being charged for your order. Please note the following:

- Permission is granted for your request in both print and electronic formats, and translations.
- If figures and/or tables were requested, they may be adapted or used in part.
- Please print this page for your records and send a copy of it to your publisher/graduate school.
- Appropriate credit for the requested material should be given as follows: "Reprinted (adapted) with permission from {COMPLETE REFERENCE CITATION}. Copyright {YEAR} American Chemical Society." Insert appropriate information in place of the capitalized words.
- One-time permission is granted only for the use specified in your RightsLink request. No additional uses are granted (such as derivative works or other editions). For any uses, please submit a new request.

If credit is given to another source for the material you requested from RightsLink, permission must be obtained from that source.

BACK | CLOSE WINDOW

CCC RightsLink®

Home | Help | Live Chat | Srimanta Pal

ACS Publications
Most Trusted. Most Cited. Most Read.

When the Signal Is Not from the Original Molecule To Be Detected: Chemical Transformation of para-Aminothiophenol on Ag during the SERS Measurement

Author: Yi-Fan Huang, Hong-Ping Zhu, Guo-Kun Liu, et al
Publication: Journal of the American Chemical Society
Publisher: American Chemical Society
Date: Jul 1, 2010

Copyright © 2010, American Chemical Society

PERMISSION/LICENSE IS GRANTED FOR YOUR ORDER AT NO CHARGE

This type of permission/license, instead of the standard Terms and Conditions, is sent to you because no fee is being charged for your order. Please note the following:

- Permission is granted for your request in both print and electronic formats, and translations.
- If figures and/or tables were requested, they may be adapted or used in part.
- Please print this page for your records and send a copy of it to your publisher/graduate school.
- Appropriate credit for the requested material should be given as follows: "Reprinted (adapted) with permission from {COMPLETE REFERENCE CITATION}. Copyright {YEAR} American Chemical Society." Insert appropriate information in place of the capitalized words.
- One-time permission is granted only for the use specified in your RightsLink request. No additional uses are granted (such as derivative works or other editions). For any uses, please submit a new request.

If credit is given to another source for the material you requested from RightsLink, permission must be obtained from that source.

BACK | CLOSE WINDOW

CCC RightsLink®

Home | Help | Email Support | Srimanta Pal

ACS Publications
Most Trusted. Most Cited. Most Read.

Plasmon-Enhanced Chemical Reaction at the Hot Spots of End-to-End Assembled Gold Nanorods

Author: Srimanta Pal, Anushree Dutta, Manideepa Paul, et al
Publication: The Journal of Physical Chemistry C
Publisher: American Chemical Society
Date: Feb 1, 2020

Copyright © 2020, American Chemical Society

Quick Price Estimate

This service provides permission for reuse only. If you do not have a copy of the portion you are using, you may copy and paste the content and reuse according to the terms of your agreement. Please be advised that obtaining the content you license is a separate transaction not involving RightsLink.

Permission for this particular request is granted for print and electronic formats, and translations, at no charge. Figures and tables may be modified. Appropriate credit should be given. Please print this page for your records and provide a copy to your publisher. Requests for up to 4 figures require only this record. Five or more figures will generate a printout of additional terms and conditions. Appropriate credit should read: "Reprinted with permission from {COMPLETE REFERENCE CITATION}. Copyright {YEAR} American Chemical Society." Insert appropriate information in place of the capitalized words.

JOHN WILEY AND SONS LICENSE
TERMS AND CONDITIONS

Aug 14, 2022

This Agreement between Mr. Srimanta Pal ("You") and John Wiley and Sons ("John Wiley and Sons") consists of your license details and the terms and conditions provided by John Wiley and Sons and Copyright Clearance Center.

License Number	5367611147816
License date	Aug 14, 2022
Licensed Content Publisher	John Wiley and Sons
Licensed Content Publication	ChemistrySelect
Licensed Content Title	Dual Role of Au nanoparticles in the Catalytic Formation of an Amorphous Polynuclear Peroxo Complex and Surface Enhanced Resonance Raman Scattering
Licensed Content Author	Srimanta Pal, Sujay Paul, Arun Chattopadhyay
Licensed Content Date	Jul 14, 2022
Licensed Content Volume	7
Licensed Content Issue	27

Licensed Content Pages	7
Type of use	Dissertation/Thesis
Requestor type	Author of this Wiley article
Format	Print and electronic
Portion	Full article
Will you be translating?	No
Title	Dual Role of Au nanoparticles in the Catalytic Formation of an Amorphous Polynuclear Peroxo Complex and Surface Enhanced Resonance Raman Scattering
Institution name	IIT Guwahati
Expected presentation date	Aug 2022
Requestor Location	Mr. Srimanta Pal IIT GUWAHATI North Guwahati Guwahati, other 781039 India Attn: Mr. Srimanta Pal
Publisher Tax ID	EU826007151
Total	0.00 USD

Terms and Conditions

Indian Institute of Technology Guwahati

TH-2949_166122105